Title
Post-Earthquake Performance Assessment and Decision-Making for Tall Buildings: Integrating Statistical Modeling, Machine Learning, Stochastic Simulation and Optimization

Author
Zhang, Yu

Publication Date
2019

Peer reviewed|Thesis/dissertation

UNIVERSITY OF CALIFORNIA

Los Angeles

Post-Earthquake Performance Assessment and Decision-Making for Tall Buildings: Integrating Statistical Modeling, Machine Learning, Stochastic Simulation and Optimization

A dissertation submitted in partial satisfaction

of the requirements for the degree

Doctor of Philosophy in Civil Engineering

by

Yu Zhang

2019

ABSTRACT OF THE DISSERTATION

Post-Earthquake Performance Assessment and Decision-Making for Tall Buildings: Integrating Statistical Modeling, Machine Learning, Stochastic Simulation and Optimization

by

Yu Zhang

Doctor of Philosophy in Civil Engineering

University of California, Los Angeles, 2019

Professor Henry J Burton, Chair

With the embrace of the seismic resilience concept as a measure of the ability of constructed facilities and communities to contain the effects of an earthquake and achieve a timely recovery, the critical role of tall buildings in supporting community functionality, has been brought to the forefront. This study presents a series of frameworks for performing post-earthquake assessment and optimal decision-making for tall buildings. A machine learning framework to assess structural safety is first proposed and applied to a low-rise frame building. A similar methodology is then adapted for tall buildings, while incorporating robust techniques to deal with the high-dimension feature space that arises because of the large number of structural components. Seismic risk assessment is then carried out for the tall building by comparing the time-dependent probability of exceeding various response demand limits over a pre-defined period considering both mainshock-only and mainshock-aftershock hazard. The risk-based consistency of the limit state acceptance criteria for engineering demand parameters is also examined. Finally, a methodology to support optimal decision-making following the mainshock is developed with the goal of minimizing expected financial losses and, at the same time, ensuring life safety. The proposed prediction model, risk assessment methodology and optimal decision-making strategy can provide critical insights into the seismic performance of mainshock-damaged tall buildings and inform the post-earthquake actions of occupants, structural engineers, insurance companies and policymakers.

The dissertation of Yu Zhang is approved.

John Wright Wallace

Scott Joseph Brandenberg

Arash Ali Amini

Thomas A Sabol

Henry J Burton, Committee Chair

University of California, Los Angeles, 2019

2019

To my parents …

For their unconditional and endless love and support

Table of Contents

List of Tables

List of Figures

ACKNOWLEDGMENTS

The research presented in this study is supported by the National Science Foundation CMMI Research Grant No. 1538866. However, any opinions, findings, conclusions, and recommendations expressed in this paper are those of the author and do not necessarily reflect the views of the sponsor.

I am very grateful to my primary advisor, Prof. Henry Burton, who not only provides guidance in the area of structural and earthquake engineering but also encourages and supports me to explore cross-discipline knowledge in reliability engineering, statistics, and computer science, which lay the solid foundation of my research and enable unique opportunities for my future career. I would also like to thank Prof. John Wallace, Prof. Scott Brandenberg, Prof. Arash Amini, and Prof. Thomas Sabol for serving as my committee members and guiding my research. Thanks also go to all the members in the Burton Research Group, who are talented, passionate, helpful and compassionate.

VITA

2007-2011	B.S. in Civil Engineering, Tongji University, Shanghai, China
2011-2014	M.S. in Mechanics, Tongji University, Shanghai, China
2014-2015	M.S. in Civil Engineering, University of California, Los Angeles, USA
2015-2019	M.S. in Statistics, University of California, Los Angeles, USA
2014-2019	Ph.D. Candidate in Civil Engineering, University of California, Los Angeles, USA

JOURNAL PAPER

Zhang, Y., Burton, H. V., Sun, H., & Shokrabadi, M. (2018). A machine learning framework for assessing post-earthquake structural safety. Structural Safety, 72, 1-16.

Zhang, Y., & Burton, H. V. (2019). Pattern recognition approach to assess the residual structural capacity of damaged tall buildings. Structural Safety, 78, 12-22.

Zhang, Y., Burton, H. V., Shokrabadi, M. & Wallace J. W. (2019). Seismic risk assessment of a 42-story reinforced concrete dual-system building considering mainshock and aftershock hazard. ASCE Journal of Structural Engineering (accepted for publication).

Sun, H., Burton, H. V., Zhang, Y. and Wallace, J. W. (2017). Interbuilding interpolation of peak seismic response demands using spatially correlated demand parameters. Earthquake Engineering Structural Dynamics, 47(5), 1168-1188.

CHAPTER 1: Introduction

1.1 Motivation and Background

For the most part, seismic design codes and guidelines are established with the intent of ensuring the most critical performance objective, which is preventing loss of life or life-threatening injury to building occupants, when a rare seismic event occurs. Recently, the ASCE/SEI 7-10 Standard [1], International Building Code [2] and National Earthquake Hazards Reduction Program (NEHRP) Provisions have consistently adopted the hazard level of 2% in 50 years as the Maximum Considered Earthquake (MCE), and updated the performance objective from life safety to collapse prevention [3], which is achieved by an upper bound of 10% collapse probability. However, they are still limited to one desired building performance objective under a specific hazard level, even though events such as the 1994 Northridge and 1995 Kobe earthquakes have highlighted the need for more robust design and evaluation procedures. While these events resulted in a relatively low number of fatalities or injuries, meeting the desired code-based performance, high levels of both structural and nonstructural damage led to 1) significant economic losses, 2) severe disruption to residential and commercial building functionality and 3) weakening of the local competitiveness and attractiveness of the affected communities.

In addition to code-based design, an alternative design procedure derived from Performance-Based Earthquake Engineering (PBEE) has been widely used, especially for special and tall buildings. PBEE provides a more encompassing design and evaluation approach that takes into consideration multiple performance objectives conditioned on a series of earthquake hazard levels. Three documents including SEAOC Vision 2000 [4], ATC 40 [5], and FEMA 273/274 [6] have laid the foundation for the first-generation PBEE [7], where multiple performance objectives such as Immediate Occupancy (IO), Life Safety (LS) and Collapse Prevention (CP) are derived from component-level Engineering Demand Parameters (EDPs). Despite its remarkable accomplishments, the first-generation PBEE had several shortcomings: 1) EDPs are mainly obtained by static analysis; 2) the relationship between EDPs and component performance are not validated by test data; 3) the overall building performance is assumed to be equal to the worst component performance [8].

To overcome these shortcomings, the Pacific Earthquake Engineering Research (PEER) Center formalized a more robust global framework for the second-generation PBEE based on probability theory. Four discrete analysis steps, i.e., 1) hazard analysis, 2) structural/nonstructural analysis, 3) damage analysis, and 4) loss analysis, are characterized by corresponding mathematical variables including Intensity Measure (IM), EDP, Damage Measure (DM), and Decision Variable (DV). The total probability theorem is employed to integrate across the various analysis steps: Probabilistic Seismic Hazard Analysis (PSHA) is conducted for a given site, followed by NRHAs performed at different IMs to obtain the corresponding EDPs, which are then related to both structural and nonstructural component DMs by fragility curves developed using test data and post-earthquake inspections. The final step involves translating the DMs to the expected DVs such as repair costs, downtime, injuries, and fatalities.

Many tall buildings which are either newly completed or under construction and which have been developed through the application of PBEE, could be found throughout the cities on the US west coast, such as Seattle, Portland, San Francisco, Los Angeles, and San Diego. For tall buildings, one of the most popular lateral resisting systems has been the reinforced concrete (RC) shear wall, which in some cases is used in conjunction with steel or RC special moment frames (SMFs).

More recently, with the embrace of the seismic resilience concept as a measure of the ability of building facilities and communities to contain the effects of an earthquake and achieve a timely recovery, the critical role of tall buildings in minimizing the impact on community functionality has been brought to the forefront (e.g. in the 2010-2011 Canterbury earthquake sequence). Although with limited fatalities or injuries, the central business district was severely disrupted. A large area in the downtown area was cordoned off mainly due to the risk of aftershock collapse and falling debris from several mid- and high-rise buildings, which were extensively damaged and subsequently slated for demolition. Moreover, local authorities mandated the closure of surrounding streets during the demolition of these buildings [9]. Although the overall Canterbury economy proved to be reasonably resilient to the impact of the earthquakes, some sectors such as retail, accommodation, and hospitality were hard hit. International visitor numbers are sharply down, and there was even some population loss from Christchurch [10]. While recent studies on mainshock-aftershock seismic performance assessment [32,86,87] have advanced our understanding of the additional seismic risk to buildings posed by aftershocks, none-to-date have focused on high-rise buildings, which are

typically designed using alternative (or performance-based) procedures. Moreover, the uncertainty in the seismic hazard (mainshock and aftershock) and the time-dependent building structural damage following the mainshock also need to be appropriately considered in the seismic risk assessment.

The physical size and concentration of people and services in tall buildings is such that their seismic performance has strong implications for the resilience of the urban environments that they occupy. As such, quantifying their seismic performance using resilience-based metrics is crucial to understanding their role in ensuring continued functionality of large city centers following a hazard event. While resilience-based assessment employs a similar approach to the current PBEE framework, a greater emphasis is placed on post-earthquake safety, functionality, and recovery. A resilience-assessment frame developed by Burton et al. [11] uses specific recovery paths which are explicitly linked to the following building performance limit states: 1) damage triggering inspection, 2) occupiable damage with loss of functionality, 3) unoccupiable damage, 4) irreparable damage, and 5) collapse. These building-level limit states are different from those used in the current version of the PBEE framework, where component-level DMs are primarily used.

The Burton et al. methodology points to the need for an objective and scientific methodology for mapping the EDPs and component-level DMs obtained from the structural and damage analysis in PBEE to building-level performance. To decide whether a damaged building is safe to occupy, existing studies and guidelines [12,13] primarily use subjective engineering judgment to relate EDPs and component DMs to building level performance. Although some practices have been carried out using basic statistical methods for low- and mid-rise buildings, further improvements are still needed. When it comes to the building-level performance assessment of the tall buildings, even fewer researches are available.

Finally, it is important that the results from previously mentioned analyses can be effectively used to help the decision-making process in the aftershock environment. The actions during a time window of interest after the mainshock and their corresponding consequences, in terms of both financial gains/losses and fatality losses, need be optimized.

1.2 Objectives

The current seismic codes, guidelines, and research have increased our preparedness for a major seismic event in the future such that life safety is guaranteed, and the financial losses are

limited. However, there are other critical questions related to the post-earthquake environment that have only been partially answered or not answered at all.

1. *Despite the widely used judgment-based tagging procedure, can we provide answers with robust statistical support for one of the most important questions right after a major seismic event, "is it safe to stay in the building"?*
2. *How safe is safe-enough? Can we define and quantify the safety of a damaged building? What is the best indicator of post-earthquake structural safety?*
3. *If various monitoring and inspection data from a damaged building are available, is it possible to integrate them together to better estimate the current state of the building? How do we trust the estimate?*
4. *If we have a methodology that works for a simple low-rise building, can it be used for tall buildings? If not, what changes are needed?*
5. *If someone is not satisfied with the simple answer of safe and unsafe, can we provide more details and let he/she make his/her own decision?*
6. *What can we do if some important information is missing but we still want to maintain the accuracy of our evaluation?*
7. *We know that a mainshock could be followed by a series of potential aftershocks. Could they make things worse? Can we consider aftershocks when designing a building?*
8. *A major earthquake just happened, and the building was strong enough to survive it. What shall we do now given that an aftershock could occur any time soon?*

The objectives of the current study are to answer these critical questions and provide helpful solutions at the building level after a major seismic event.

1.3 Organization and Outline

This study consists of a total of seven chapters. Starting with the introduction in Chapter 1 and ending with the summary in Chapter 7, the main body covers 5 distinct yet closely related chapters, of which most are adopted from published research papers by the author.

Chapter 2 outlines a machine learning framework to assess post-earthquake structural safety. The concepts of response and damage patterns are introduced and incorporated into a systematic methodology for generating a robust dataset for any damaged building. Incremental dynamic analysis using sequential ground motions is used to evaluate the residual collapse capacity of the damaged structure. Machine learning algorithms are used to map response and

damage patterns to the structural safety state (safe or unsafe to occupy) of the building based on an acceptable threshold of residual collapse capacity. Predictive models including classification and regression tree and Random Forests are used to probabilistically identify the structural safety state of an earthquake-damaged building. The proposed framework is applied to a 4-story reinforced concrete special moment frame building.

Chapter 3 presents the structural modeling, probabilistic seismic hazard analysis and ground motion selection of tall buildings with core walls and special moment frames and lays the foundation for the analyses in the following chapters.

Chapter 4 extends the framework discussed in Chapter 2 to tall buildings with special focus on the high dimensional feature space. A pattern recognition approach is proposed to quantitatively assess the residual structural capacity of earthquake-damaged tall buildings. Sequential NRHAs using as-recorded mainshock-aftershock ground motions are conducted to generate distinct feature patterns comprised of spatially distributed global and local EDPs within the tall building. Residual structural capacity is assessed based on the median spectral intensity corresponding to the collapse prevention performance level. Correlation-based filtering and feature selection using Least Absolute Shrinkage and Selector Operator (LASSO) is performed to effectively reduce the high dimensional feature space while selecting the most informative ones. The features that survive the filtering but excluded by LASSO are reserved and grouped based on their correlations with those that are selected. These reserved features can be utilized when the selected ones are unavailable. Predictive models using Support Vector Machine are constructed to map the EDP-based features to the residual structural capacity of the tall building.

Chapter 5 presents a seismic risk assessment of a 42-story reinforced concrete dual-system building considering mainshock and aftershock hazard. Sequential NRHAs are also performed. Aftershock assessment describes the case where the mainshock has occurred and the associated damaged state of the building is known. A Markov process model is used to integrate the increase in vulnerability of the mainshock-damaged building with the time-dependent aftershock hazard. Aftershock risk is quantified as the probability of exceeding the structural response demand limits used in performance-based seismic design of tall buildings at different instants in time following the mainshock. The same metric is used to quantify mainshock-aftershock risk, however, for this type of assessment, the uncertainty in the intensity and

damage caused by both the mainshock and aftershock is considered. The results of mainshock-only, aftershock and mainshock-aftershock assessment are compared and discussed.

Chapter 6 seeks to support optimal decision-making in the aftershock environment by integrating the time-dependent Markov Process-based methodology developed in Chapter 5 with dynamic programming. The objective is to minimize the expected total financial loss from various sources such as structural and nonstructural component damage, fatalities due to collapse, functionality disruption, and repair cost. The expected cumulative loss within a certain time window of interest is obtained by summing up the discounted values of all the potential losses in the future. In addition to the fatality loss, a safety constraint is defined based on the transition probability into unsafe damage states to ensure life safety. The transition from a higher damage state to a lower one (due to repair actions), which is previously excluded in Chapter 5, is also considered in this chapter. Two sets of actions after the mainshock are considered at any time point: 1) whether to evacuate the building and when to reoccupy the building if it is previously evacuated and 2) whether to repair the building and when to start to start and stop the repairs (assuming that the building had been restored to a satisfactory state). Dynamic Programming is then performed to find the optimal actions throughout the time period of interest Sensitivity analyses are carried out to quantify the impact of the key parameters on the decision-making, including time window, safety threshold, fatality loss, disruption loss, and repair cost.

Chapter 7 summarizes all the key findings of the previous chapters, discusses the limitations of the current work and provides potential directions that could improve the proposed frameworks, methodologies and practices.

CHAPTER 2: Machine Learning Framework for Assessing Post-Earthquake Structural Safety

This chapter is adopted from the following study:

Zhang, Y., Burton, H. V., Sun, H., & Shokrabadi, M. (2018). A machine learning framework for assessing post-earthquake structural safety. Structural Safety, 72, 1-16.

2.1 Introduction

Assessing building structural and nonstructural component-level damage is a key step in the performance-based earthquake engineering (PBEE) framework [4–6,8,14–17]. Component damage characterization serves as the link between building structural response and the performance metrics (death, dollars, and downtime) that are relevant to end-users. More recently, the importance of building-level limit states has been highlighted due to the growing emphasis on quantifying seismic resilience at the individual infrastructure and community scales [18,19]. Iervolino [20] defined post-earthquake building-level limit states based on the level of functionality (relative to before the event) that a damaged structure could support following an earthquake. These limit states were used to model the probabilistic recovery of functionality using state- and time-dependent Markov Chains. In the assessment of the seismic resilience of a residential community, Burton et al. [11] proposed a set of building-level limit states, which are explicitly linked to post-earthquake recovery and functionality. Fragility curves were developed to link ground shaking intensity to the probability of exceedance of these limit states, which include functional loss, unsafe to occupy, demolition and collapse. Building-level limit states have also been used for lifecycle seismic performance assessment and optimization for structures, where retrofit strategies, repair cost, time and salvage value are considered [21].

Post-earthquake structural safety is key to determining whether a damaged building is safe to re-occupy, which is one of the key pieces of information needed by stakeholders immediately after an earthquake. ATC-20 [22,23] provides guidelines for post-earthquake visual inspection to rapidly evaluate building structural safety and assign corresponding green, yellow and red tags to buildings that are deemed safe to occupy, occupiable with restrictions and unsafe to occupy respectively. It has been widely used after U.S. earthquakes such as Loma Prieta, Landers, Northridge [23] and Hawaii [24] and adapted for use in many other countries around

the world. Building on the work of Porter et al. [16], Mitrani-Reiser [25] used fragility curves to map continuous EDPs to discrete component-level damage states that have similar descriptions to the ones used in ATC-20. A "virtual inspector" was then used to probabilistically estimate building safety and assign corresponding tags based on the criteria in the first two tiers of an ATC-20 evaluation. The Mitrani-Reiser methodology was adopted in FEMA P58 [12,13] using a slightly different approach to link component-level damage to the likelihood that a building will be assigned an unsafe placard. For each structural and non-structural element, the median fraction of components (based on the total number in the building or a single story) in a particular damage state is estimated. The damaged building is assigned an unsafe placard if any of these values exceed a pre-defined triggering ratio. For example, the unsafe placard for steel special concentrically braced frames with wide flange braces could be triggered by any of the three scenarios: more than 60% of the components are in damage state 2 (brace has lost significant axial capacity), more than 40% of the components are in damage state 3 (brace and gusset are severely damaged with significant loss in stiffness and resistance), and more than 20% of the components are in damage state 4 (brace or gusset have fractured). It is important to note that the triggering ratios in FEMA-P58 are largely based on judgement and are not explicitly linked to the reduction in collapse safety of the damaged building.

Incremental dynamic analysis (IDA) [26–28] has been widely used to probabilistically assess the most critical building-level limit state of collapse. More recently, the reduction in the collapse capacity of mainshock damaged buildings has been used as a metric for assessing the post-earthquake structural safety and occupiability of damaged buildings. IDAs are performed using sequential ground motions to quantify the reduction in collapse capacity. Maffei et al. [29,30] proposed four post-earthquake occupiability criteria, which differ based on the metric used to quantify the reduction in collapse safety of the damaged building. Yeo and Cornell [31] used the time-varying aftershock hazard at a given site to compute an equivalent constant collapse rate, which decreases with time after the occurrence of the mainshock. The time-varying tagging scenarios are established based on the evolving collapse risk in the aftershock environment. The time-dependent tag could be changed from red to yellow and even green as time elapses. In the Maffei et al. and Yeo and Cornell studies, no direct link was made between component-level damage and the safety state of the building. Raghunandan et al. [32] quantified the increase in vulnerability to collapse of mainshock-damaged modern ductile reinforced concrete (RC) special moment frame (SMF) buildings.

They also evaluated the extent to which different system- (transient and residual story drifts) and component-level damage indicators (e.g. beam and column plastic rotation) can serve as a proxy for the reduced collapse capacity. Single variable linear regression was used to link individual damage indicators to the residual collapse capacity. Burton and Deierlein [33] extended the Mitrani-Reiser and FEMA P58 approach by explicitly linking the component-level damage ratios that trigger an unsafe placard to the increase in collapse risk of the damaged building. However, the interaction between damage indicators was not considered in either of these two (Raghunandan et al., and Burton and Deierlein) studies.

Presented in this chapter is a novel approach to assessing post-earthquake structural safety. Central to the newly proposed methodology is a machine learning framework for mapping building response and observable damage patterns to the residual collapse capacity of the structure, which is used as the criterion for assessing its safety state. The term "response pattern" is used to describe the distribution of peak global (e.g. residual and transient drifts) and local response (component deformations) demands obtained from NRHA. Similarly, the term "damage pattern" describes the distribution of observable states of physical damage to key structural components obtained from damage simulation. Machine learning algorithms including classification and regression tree (CART) and Random Forests are used to build predictive models, which can probabilistically identify the post-earthquake structural safety state of the building based on its residual collapse capacity, given any unique response or damage pattern. To illustrate the overall methodology, a case study is conducted using a 4-story RC SMF building. Several applications are envisioned for the proposed framework. The model can be embedded in an electronic tool that can be used to supplement the judgment of field inspectors conducting post-earthquake building safety assessments. Observations of the distribution of component-level damage (or damage pattern) can serve as inputs into the model, which will provide probabilistic predictions of the safety state based on the reduced collapse capacity. For buildings instrumented to record, process and transmit structural response demands, the machine learning algorithm can be used to provide preliminary rapid estimates of the safety state of the building. The methodology can also be used to generate fragility curves for the "unsafe to occupy" building-level limit state, which can be incorporated into building or community resilience and lifecycle performance assessments and optimization.

2.2 Post-Earthquake Structural Safety Assessment

2.2.1 Overview of Methodology

A schematic overview of the methodology used to assess post-earthquake structural safety is shown in Fig. 2-1. Starting with an intact structure, five distinct yet fully integrated steps are used to illustrate the assessment framework. The outcome of this assessment is the predicted structural safety state conditioned on the structural response demands (from instrumentation) and/or available observed physical damage (through field inspections).

The first step describes the process of using a set of "damaging" ground motions to create samples of the damaged structure from which response and damage patterns will be extracted. The response patterns or distribution of EDPs is obtained directly from NRHA. Subjecting the intact structure to a single damaging ground motion scaled to a specific spectral intensity will produce a single distinct response pattern. Multiple response patterns with different levels and distributions of response demands are obtained by using a suite of damaging ground motions scaled to incrementally increasing spectral intensities. Damage patterns are simulated using structural component damage fragility functions which relate local EDPs to the probability of exceeding a given damage state. A single damage pattern is described by each structural component assigned a single discrete damage state. Monte Carlo Simulation is used to generate multiple damage patterns for single ground motion and spectral intensity. More details on generating the response and damage patterns and their relationship to the safety state of the building are provided in Section 2.3.

The collapse capacity of the damaged structure is assessed through the application of IDAs using sequential ground motions in the second step (Step 2). Each damaging record, which is used as the first ground motion in the sequence, is followed by an IDA using a set of "collapsing" ground motions. The median first-mode spectral acceleration corresponding to the collapse point $(\hat{S}a_{col,DMG})$ is used as the measure of residual collapse safety of the damaged building. In the third step, the collapse capacity of the intact structure is assessed by conducting single-record IDAs using the collapsing ground motions. The median collapse capacity $(\hat{S}a_{col,INT})$ is also used as the measure of collapse safety for the intact structure. Note that the dispersion or log-standard deviation of the collapse capacities, $\beta_{col,DMG}$ and $\beta_{col,INT}$, are also obtained but not directly used. The ratio of $\hat{S}a_{col,DMG}$ to $\hat{S}a_{col,INT}$ (κ) is used as a quantitative measure of the increased collapse vulnerability or the reduction in the collapse capacity of the

damaged structure. The damaged building is classified as safe or unsafe to occupy by comparing κ to a pre-established threshold (κ_{min}), which represents the minimum acceptable reduction in collapse safety.

The fourth step uses 1) the response and damage patterns generated in step 1 and 2) their associated post-earthquake structural safety states determined based on the reduction in collapse safety (comparing κ to κ_{min}) obtained from steps 2 and 3 to establish a classification problem. The machine learning algorithm is then used to construct predictive models. Subsequently, any arbitrary response and/or damage pattern can be used to probabilistically predict the safety state of an earthquake-damaged structure (Step 5).

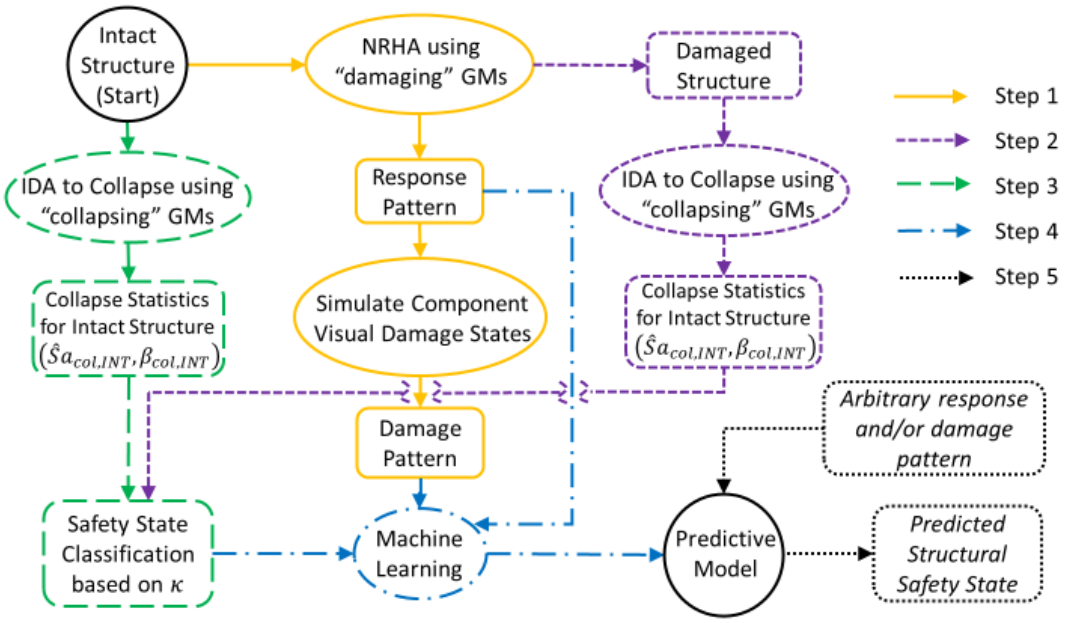

Fig. 2-1. Schematic of post-earthquake structural safety assessment methodology

2.2.2 Establishing Post-Earthquake Safety State Criteria

As noted in Section 2.1, the reduction in the collapse capacity of the damaged structure (as defined by κ) is used as the basis for assessing its post-earthquake safety state. For each of the damaging ground motions, ten incrementally-increasing maximum story drift ratio (SDR_{DG}) levels are targeted, ranging from 0.5% to 5% at increments of 0.5%. These SDR_{DG} values serve as proxies for the possible states of building damage under a damaging ground motion. The number and increment of SDR_{DG} used to generate the response and damage patterns is selected to balance the need to cover a broad range of damage levels and the computational expense associated with performing IDA to collapse of the damaged structure (described in step 2). Fig.

2-2 shows a series of IDA plots for the intact structure and three instances of the damaged structure for the 4-story RC SMF building used to illustrate the methodology. The design, modeling and ground motion details are provided in Section 3.1. Fig. 2-2 (a) shows that the median collapse capacity for the intact building, which was obtained by applying IDAs using the collapsing ground motions, is 1.20g. Fig. 2-2 (b), (c) and (d) show IDA plots for the damaged structure generated using a single damaging ground motion scaled to produce SDR_{DG} values of 2%, 3.5% and 5% respectively. Note that, for the damaged structure, the PSDR corresponding to a collapsing ground motion spectral acceleration level (Sa_{T1}) of zero is the same as the residual drift demand from the damaging ground motion. As expected, the median collapse capacity decreases as SDR_{DG} increases. For example, the median collapse capacity is 1.12g ($\kappa = 0.93$) when $SDR_{DG} = 2\%$ and reduces to 0.43g ($\kappa = 0.36$) when $SDR_{DG} = 5\%$.

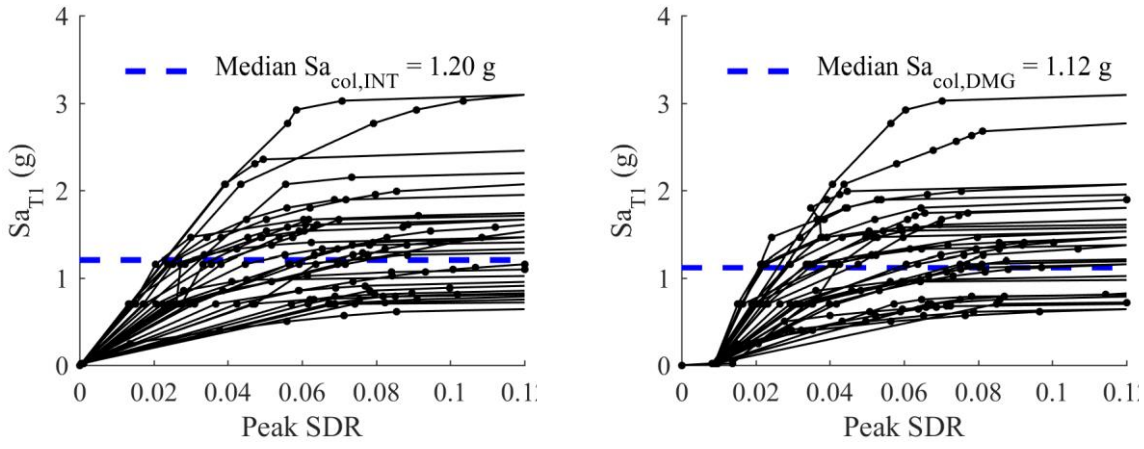

(a)

(b)

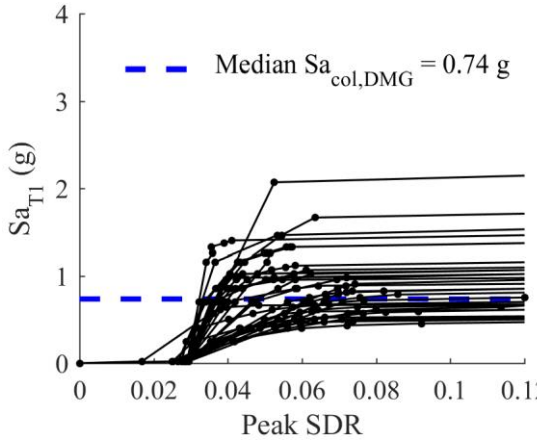

(c)

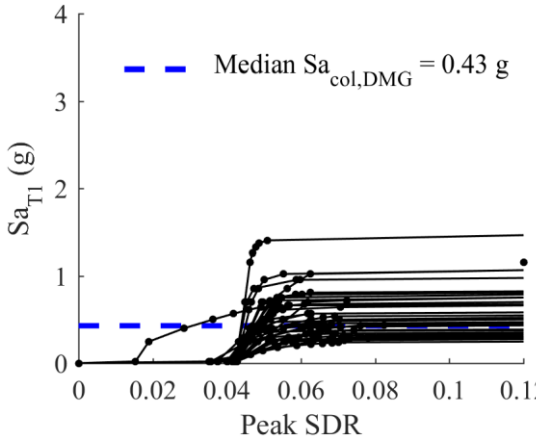

(d)

Fig. 2-2. Example IDAs using safety-testing ground motions for the (a) intact building and the building damaged by damage-generating ground motions with PSDR of (b) 0.01, (c) 0.03 and (d) 0.05

For each damaging ground motion, log-normal collapse fragility curves are fitted for the ten target damage levels, while accounting for record-to-record variability and structural modeling uncertainty [12,13]. Examples of these fragility curves and the relationship between κ and SDR_{DG} for a single damaging ground motion are shown in Fig. 2-3. It shows that there is no measurable reduction in collapse safety until $SDR_{DG} = 2\%$, where κ drops to 0.92, after which κ decreases almost linearly with SDR_{DG}. The results shown in Fig. 2-3 (b) confirms the effectiveness of SDR_{DG}as a proxy for the severity of structural damage. Moreover, only for this specific damaging ground motion, it appears that κ corresponding to $SDR_{DG} = 2\%$might be an appropriate minimum threshold (κ_{min}) to distinguish the safe and unsafe structural states. Further discussion of this issue is presented later in this section.

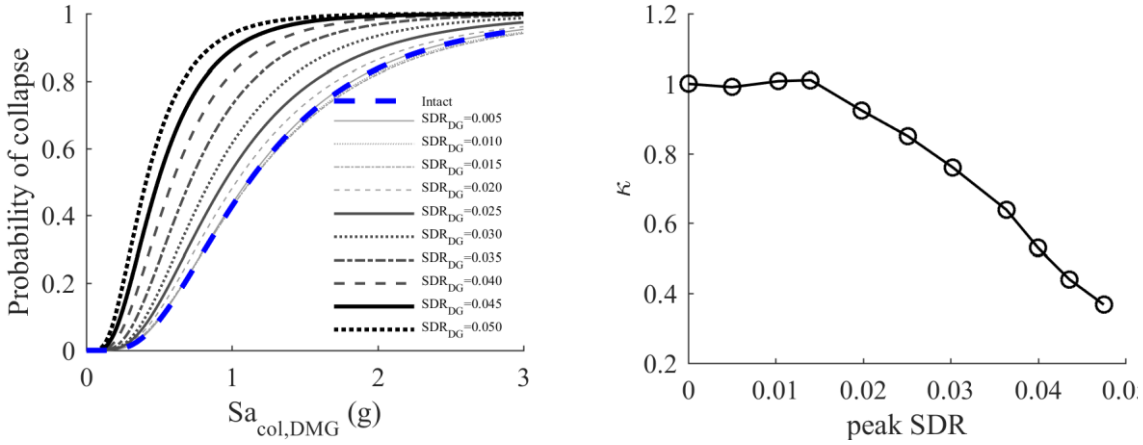

(a) (b)

Fig. 2-3. Example (a) collapse fragility curves and (b) median κ versus PSDR under the DG ground motion

Establishing an acceptable value of κ_{min} is partly a policy decision and is not fully addressed in this study. However, as noted earlier, the observed trend between κ and SDR_{DG}can inform the choice of κ_{min}. To further illustrate this point, Fig. 2-4 (a) shows a plot of κ and SDR_{DG}that was generated by using a suite of damaging ground motions. The details of the damaging and collapsing ground motions used in this study are presented in Section 3. Fig. 2-4 (b) shows a statistical summary of the relationship shown in Fig. 2-3 (b) including plots based on the median ($\hat{\kappa}$) and a 90% confidence interval for κ. Here it can be observed that the absolute value of the slope of the median line remains roughly constant up to about

$SDR_{DG} = 2\%$, after which there is a sharp increase. Based on this observation, one approach could be to take κ_{min} to be the median value of κcorresponding to $SDR_{DG} = 2\%$ in this study. Note however that, using this approach, there is a 50% probability that the value of $\kappa$is less than κ_{min} (based on the definition of the median) at $SDR_{DG} = 2\%$. An alternative approach is to choose a value of κ at $SDR_{DG} = 2\%$that has a higher probability of being exceeded (e.g. 90% probability that $\kappa \geq \kappa_{min}$). A third approach would be to consider the uncertainty in the safety state threshold by assuming a parametric (e.g. lognormal) probability distribution for $\kappa_{min}$and using the mean/median and dispersion corresponding to $SDR_{DG} = 2\%$.

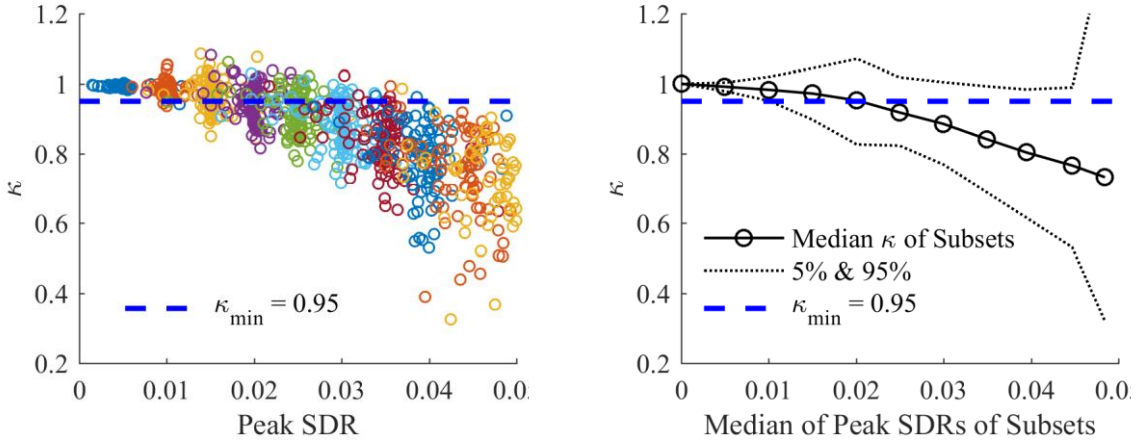

(a) (b)

Fig. 2-4. Median collapse capacity for (a) individual samples and (b) sample subsets by target damage levels

2.2.3 Classified Structural Response and Damage Patterns

As described in Section 2.1, structural response and damage patterns are used in combination with the safety states to construct the prediction model using an appropriate machine learning algorithm. Fig. 2-5 shows some examples of response patterns obtained from NRHA using the "damaging" ground motions and the corresponding safety state. The global response patterns include peak transient and residual SDRs throughout the building height [Fig. 2-5 (a) and (b)]. Profiles of peak plastic hinge rotations in the frame beams and columns [Fig. 2-5 (c) and (d)] are considered local response patterns. A single profile represents the response pattern for a single "damaging" ground motion and value of SDR_{DG}. The response patterns are classified into the safe and unsafe states based on κ_{min} (median κ at $SDR_{DG} = 2\%$) from Fig. 2-4 (b). A noteworthy observation is that there is a clear demarcation between the peak and residual drift response patterns of the safe and unsafe states in the first two stories. However, in the upper stories, there is a fair amount of overlap between the response patterns of the two

safety states. A similar observation can be made for the response patterns based on the beam and column plastic hinge rotations. This observation highlights the importance of considering the spatial variation of EDPs (or response pattern) and not just the absolute maximum in the entire building in structural safety state assessment.

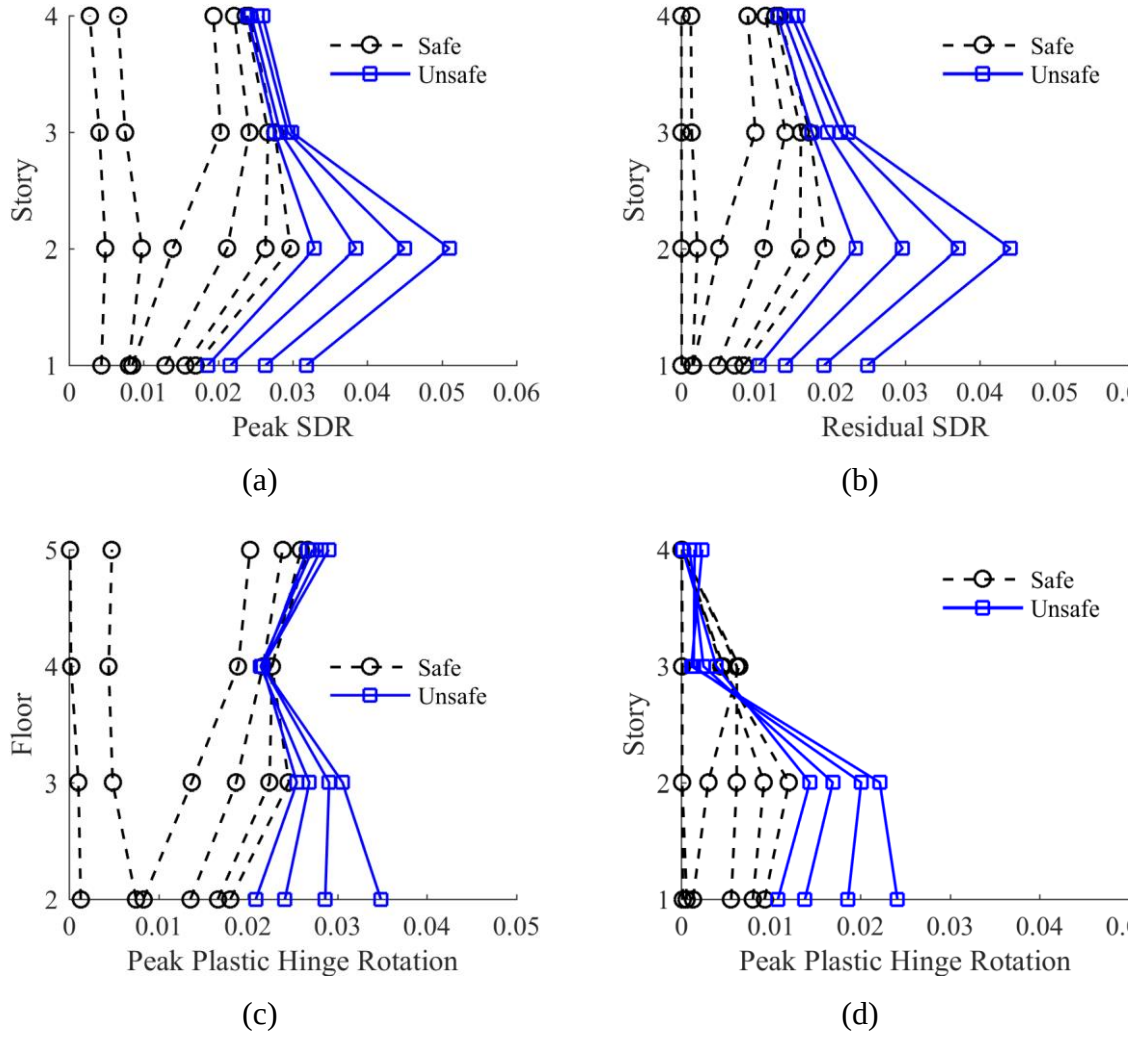

Fig. 2-5. Example response patterns of (a) peak and (b) residual SDRs, and peak plastic hinge rotations of exterior (c) beams and (d) columns

Examples of safe and unsafe damage patterns for the beam hinges simulated using the peak plastic rotations in Fig. 2-5 (c) are shown in Fig. 2-6. Damage patterns are described by each element being assigned one of four discrete damage states, where state 0 represents no visual damage and state 3 represents the most severe damage requiring complete beam replacement. Comparing Fig. 2-6 (a) and (b), the damage pattern corresponding to the unsafe state has 8 beam hinges in higher damage states, 10 in the same damage states and 5 in lower damage states. This observation again reinforces the need to consider the spatial distribution of physical damage (or damage patterns) to assess the severity of system-level damage and the

corresponding building safety state. The response and damage patterns in Fig. 2-5 and Fig. 2-6 suggest that only a subset of the EDPs and damage states would significantly affect the structural safety states. It is important to recall that these results represent patterns obtained for a single damaging record and their spatial variation and severity could be very different for other distinct ground motions. A major advantage of the machine learning approach is the availability of powerful algorithms that can isolate the most critical response and damage points and establish more clear distinctions between the two safety states.

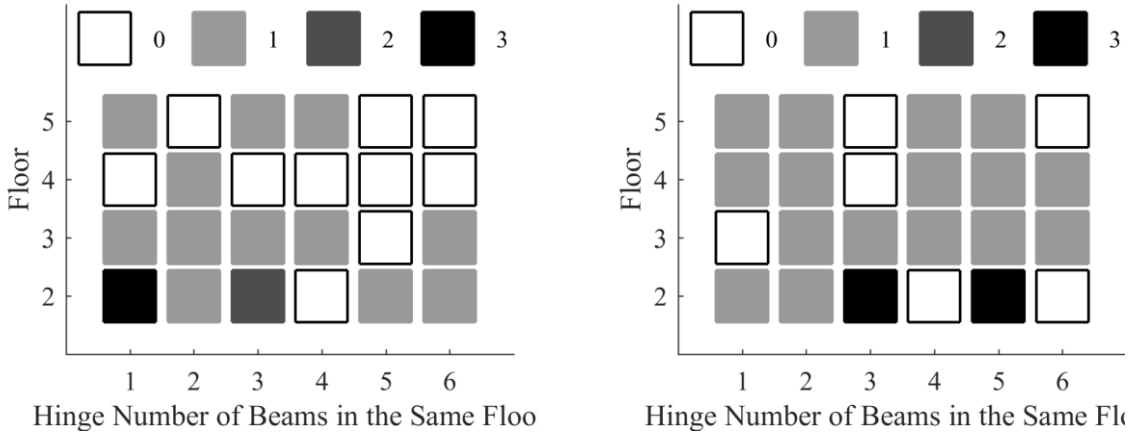

Fig. 2-6. Example damage patterns at beam hinges for a structure classified as (a) safe and (b) unsafe

2.2.4 Safety State Prediction using Machine Learning

In a classification problem, machine learning algorithms utilize an observed dataset that is divided into a training subset, which is used to construct the predictive models, and testing subset, which is used to evaluate the performance of those models. Each observation has two attributes: a set of predictors and their associated classes. In this study, the response and damage patterns serve as the predictors, which are always assumed to be available. The structural safety states (safe or unsafe) serve as the corresponding binary categorical classes, which are assumed to be known for the training data and unknown for the testing data.

2.2.4.1 Classification and Regression Tree

CART is a machine learning algorithm that can be used to predict both categorical classes (classification tree) and ordered values (regression tree) [34]. This study is focused on categorical class prediction. By recursively partitioning the predictor space (P), CART gradually explores and learns the structure of the observed dataset with the goal of creating

mutually exclusive subspaces with better purity. The ratio between the sample number of the dominant class, which is the one with the most samples, and the size of the subset, defines the purity of a subspace.

Fig. 2-7 shows an example of a simple binary tree that is used to represent a CART. It comprises of a root node (node number 1 in Fig. 2-7), three interior nodes (numbered 2, 4 and 8) and five leaf nodes (numbered 3, 5, 9, 16 and 17). Except for the root node which consists of the full sample space, each node represents a subspace of observed predictors and classes. Each interior (or decision) node is generated when a parent node is split into two child nodes based on the observed values of one of the predictors ($p \in P$). For example, the split at the root node is based on the damage state in one of the beam hinges (e.g. damage state ≤ 0.5 or > 0.5). The edges from a parent node to two child nodes represent a split ($s_p \in S_p$), where S_p is the space of all the split points in predictor p at the parent predictor. The simple tree shown in Fig. 2-7 has a depth (the number of splits) of four and five leaf (terminal) nodes. Each leaf node provides a predicted class ($c \in C$), where C is the space of all the classes under consideration, given the inputs of all the predictors represented by the complete path from the root to that leaf.

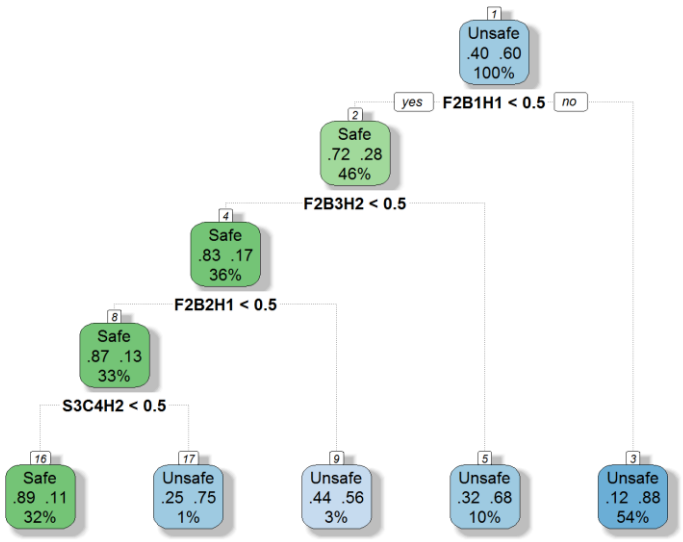

Fig. 2-7. Example tree structure, where $FiBjHk$ denotes the damage states at Hinge k of Beam j at Floor i, and $SiCjHk$ denotes the damage states at Hinge k of Column j in Story i.

There are three main steps involved in building a CART model. First, the binary tree is grown following the greedy algorithm, which always tries to find a predictor, p, and its split point, s_p, that maximizes the purity (or minimizes the impurity) of the resulting subspaces. The Gini Index (GI) [34] is introduced as a measure of the impurity in Equation 2.1.

$$GI = \sum_{n \in N} \sum_{c \in C} \pi_n \rho_c (1 - \rho_c) = \sum_{n \in N} \pi_n (1 - \sum_{c \in C} \rho_c^2) \tag{2.1}$$

where N is the set of all leaf nodes in a given tree; π_n is the proportion of the dataset falling into a leaf node, $n \in N$, and ρ_c denotes the probability of class c at a given node. For the predictors with ordered values such as the response patterns, each split point, s_p, creates a hyperplane perpendicular to the axis of the predictor, p, at location s_p, to divide the predictor subspace of the current parent node. For predictors defined by categorical classes, such as the damage patterns, each split point, s_p, partitions the predictor space into two sets of classes: one contains only a selected class c and the other consists of all other classes, $(C - c)$. Starting with the root node, all the predictors are assembled and almost all their possible split points are tested by computing the GI for each split. The predictor and split point with the lowest GI is then used to create two child nodes. This process is repeated to recursively partition the dataset into subspaces with boundary surfaces parallel to the predictor axes.

The second main step involves establishing an appropriate criterion for stopping the growth of the tree. Examples of stopping criteria include a minimum number of samples needed at a given node for the further split, a maximum tree depth, a limit on the total number of leaf nodes in a tree. An alternative stopping criterion that balances the tree size and its associated GI could be achieved by introducing a penalty term. The concept of cost-complexity tuning [34] is then adopted, which penalizes the GI.

$$GI = \sum_{n \in N} \pi_n (1 - \sum_{c \in C} \rho_c^2) + c_p |N| \tag{2.2}$$

where c_p is the complexity parameter and $|N|$ is the size of N for the given tree. Equation 2.2 stops the growth of the tree when the gain from reducing the overall impurity is not large enough to compensate for the cost of an excessively complex tree. It should be noted that the optimal value of c_p could be very different for different datasets. If it is too large, the model will be unable to adequately capture the characteristics of the dataset. On the other hand, a c_p that is too small can lead to overfitting of the training data and have poor performance on the testing data.

The third and final step involves pruning the tree to reduce the possibility of overfitting. This could be achieved by randomly selecting a hold-out set from the training data at the very beginning, passing it through the generated tree, and testing all splits from the bottom-up,

deleting those whose removals would reduce the overall impurity for the hold-out set. The pruning process continues recursively until there are no further improvements.

2.2.4.2 Random Forests

Although powerful, a CART is very sensitive to the specific dataset on which it is trained and is, therefore, a high-variance model. As a result, the tree and corresponding predictions generated for different subsets of the same training dataset could be quite different. This problem can be addressed by assembling bootstrap-sampled subsets of the training data. Bootstrap is a statistical technique that involves randomly sampling from a dataset to create a series of sub-datasets [35,36]. Each random sample is placed back into the original dataset such that multiple (or no) instances of a particular sample can be included in the sub-dataset. Based on these resampled datasets, bootstrap aggregation, also known as bagging [37], is an ensemble method, which seeks to achieve better predictions by combining multiple less accurate models. Bagging CART is used to train the predictive models using all these resampled datasets and generate aggregated predictions by using the prediction that is generated by the majority of models.

While bagging addresses some of the limitations of a basic CART model, the method still has an inherent defect that prevents it from producing the optimal predictive model. Bagging CART can result in highly correlated tree structures due to the application of the greedy algorithm, where all of the original predictors are considered at every split of every tree [38]. In order to overcome this problem, the Random Forests [39] algorithm was developed with a modification to Bagging to reduce such tree correlation. At each split point during the growth of the tree, Random Forests only applies the greedy algorithm to a randomly selected proportion of the original predictors.

2.2.4.3 Evaluating the Performance of the Prediction Model

Since the unsafe state is unfavorable and critical, it is defined in this study as the “positive class” while the safe state as the “negative class”. This section introduces some important performance measures, which are used for testing and selecting the predictive models built using different machine learning algorithms and corresponding tuning parameters.

The sensitivity or true positive rate is defined as the proportion of the unsafe (positive) samples in the testing dataset that are also predicted to be unsafe. The specificity of a prediction model, which is also referred to as the true negative rate, is expressed as the proportion of

known safe (negative) samples that are correctly predicted. The accuracy, which combines the sensitivity and specificity, is computed as the ratio between the sum of all the true positive and true negative samples and the number of the total samples. The false positive rate represents the proportion of the safe samples which are recognized as unsafe by the predictive model and is equal to one minus the specificity. More importantly, the false negative rate measures how many of the unsafe samples are misclassified as safe by the predictive model. This is the most unfavorable situation as it poses the highest risk to injury or fatality of the building occupants and therefore needs to be carefully maintained at an acceptably low rate.

The receiver operating characteristic (ROC) describes the relationship between sensitivity and specificity [40,41]. The discrimination threshold of the ROC, which can take on a numerical value between 0 to 1, is used to relate the probability distribution of the safety state to a single state. A sample is classified as unsafe if the probability of being positive obtained from the predictive model is larger or equal to this threshold; otherwise, the safe classification is assigned. A threshold of 0 guarantees the maximum sensitivity because all the samples are predicted to be unsafe and 1 provides the best specificity because it produces only safe predictions. When the threshold increases, the sensitivity drops while the specificity grows. A ROC curve is obtained by incrementally varying the discrimination threshold from 0 to 1 and plotting its corresponding sensitivity and specificity. The area under the ROC curve is then used as a balanced measurement of the performance of a particular model.

K-fold cross-validation is a resampling technique that is also used to reduce possible overfitting and select the optimal tuning parameters for a predictive model [36]. The initial sample space is partitioned into k roughly equally-sized subsets, and a model is trained using all but one held-out subset, which is used to assess the model performance [38]. This procedure is repeated k times by holding out the subsets one at a time and fitting the model to the remaining $(k-1)$ subsets. The overall performance for these k resampled datasets is evaluated for each predictive model with specific tuning parameters, such as the complexity parameter for CART, the number of total trees and number of randomly selected predictors to choose from at each split for Random Forests. The k-fold cross-validation procedure could also be repeated using a different set of partitioned subsamples to further reduce possible bias from the partition.

2.3 Case Study: Post-Earthquake Structural Safety of A Modern Reinforced Concrete Special Moment-Frame Building

2.3.1 Building Description, Ground Motion Selection, Structural Modeling, and Response Simulation

The post-earthquake structural safety of a 4-story perimeter frame building is assessed to demonstrate the proposed framework. This building was developed by Haselton et al. [42] (identified with building design ID 1013) as part of a larger study on the seismic collapse safety of modern code conforming reinforced concrete moment frame buildings. The building was designed according to the provisions of the International Building Code [2], ASCE 7-02 [1], and ACI 318 [43], which includes requirements for strength, stiffness, capacity design, and detailing. The building has an 8-in flat slab floor system with a square plan of $120ft$ by $120ft$. A height of $15ft$ is used for the first story and $13ft$ for all the upper stories. The seismic design is based on the mapped hazard for a Los Angeles site with $S_S = 1.5g$, $S_1 = 0.6g$, and soil site class D.

A two-dimensional model of the three-bay moment frame is built in OpenSees [44] (Fig. 2-8) using expected gravity loads ($D + 0.25L$). A leaning column is used to account for P-Delta effects resulting from the loads on the gravity system, which is not explicitly modeled. The leaning column is axially rigid, provides no lateral restraint and the horizontal translational degrees of freedom of the end nodes are constrained to the floor nodes. It is assumed that damage to the slab-column connections of the gravity system will not result in a vertical collapse of the slab. The foundation rotation stiffness is calculated from typical grade-beam design and soil stiffness properties. The moment frame columns are fixed at the base. Rayleigh damping corresponding to 5% of critical damping in the first and third modes is applied.

The moment frame is defined using elastic beam-column elements with flexural plastic hinges at the ends. The nonlinear behavior of the flexural hinges in the frame beams and columns is based on the peak oriented hysteretic model [45] and the predictive equations developed by Panagiotakos and Fardis [46] and Haselton et al. [47] are used to obtain the backbone parameters, such as the plastic rotation capacity, post-capping deformation capacity, the ratio of maximum to yield moment and the energy-based cyclic degradation

parameter.

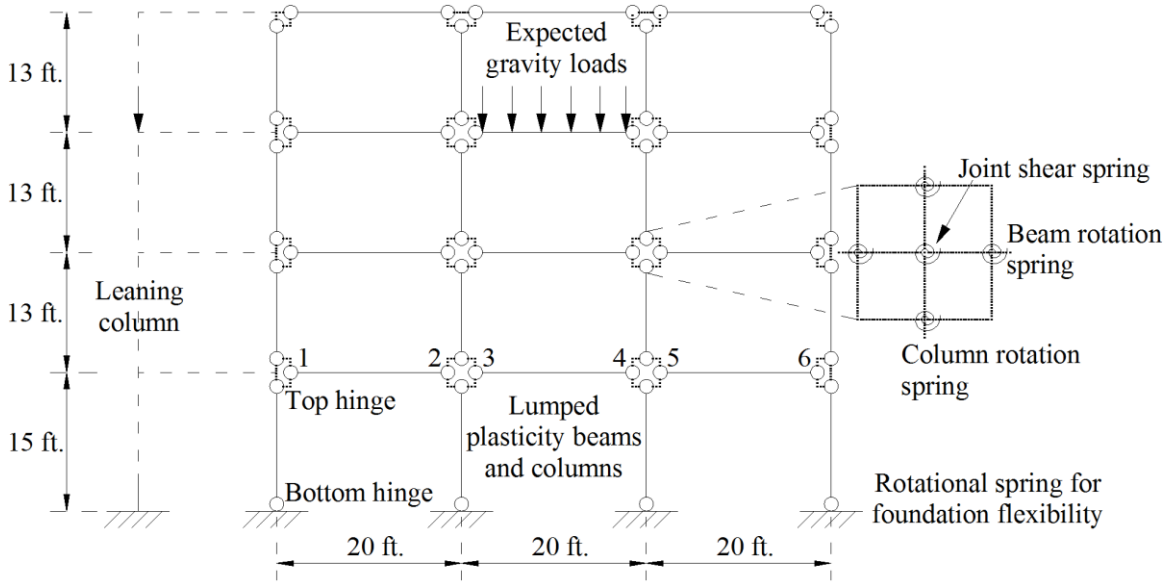

Fig. 2-8. Schematic illustration of the RC SMF OpenSees model

The ground motions used for NRHA are selected based on the conditional mean spectra, which are computed for the building site (118.162º W, 33.996º N) using probabilistic seismic hazard deaggregation and the ground motion prediction equations developed by Campbell and Bozorgnia [48,49]. The approach suggested by Baker and Cornell [50,51] is used to select both the damaging and collapsing ground motions, where a mean ε of 1.47 for large-magnitude short distance events is used for both sets. A total of 98 ground motions is included in the damaging set by randomly sampling one of the horizontal components of each record. This is done to avoid having ground motions with highly correlated spectral shapes that would induce similar (and redundant) response patterns. 32 ground motion pairs are selected for the collapsing set. The collapsing and damaging ground motion spectra are shown in Fig. 2-9.

The collapse performance of the intact building is evaluated by performing IDAs using the two components in each pair of the collapsing ground motions and taking the lower of the two collapse intensities. To obtain the collapse capacity of the damaged buildings, sequential NRHAs are performed, whereby the building is subjected to each of the 98 damaging ground motions, followed by an IDA to collapse using the 32 pairs of collapsing records. Like the intact building, the lower of the two collapse intensities for each collapsing record-pair is used for the damaged buildings. The response and damage patterns are obtained from the damaging analysis. Using the ten states of building-level damage described in Section 2.2 for each

damaging ground motion produces 980 samples, which include response patterns, damage patterns, and $\kappa's$. However, 55 of those samples were excluded because collapse occurred during the damaging analysis. As a result, the prediction model was constructed using 935 samples.

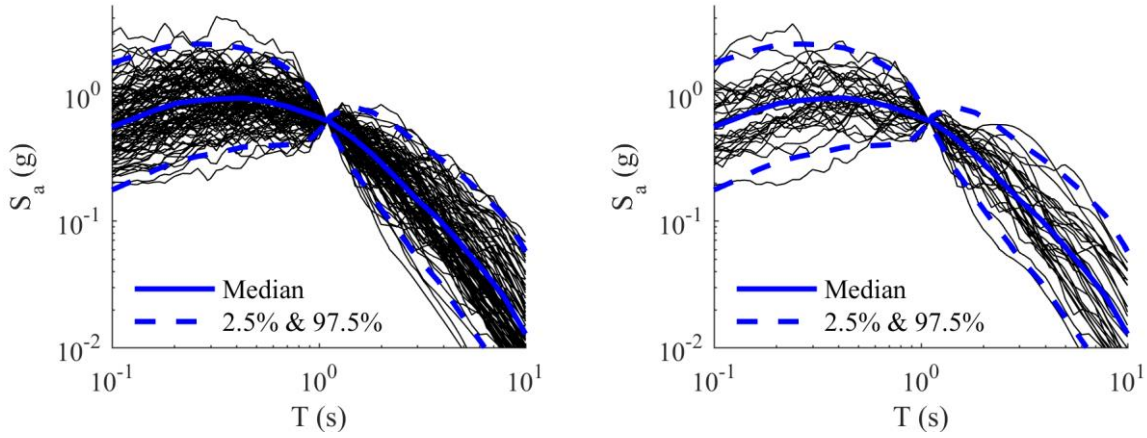

Fig. 2-9. Response spectra for (a) damaging and (b) collapsing ground motions

2.3.2 Safety-State-Based Distribution of Response Demands and Damage Patterns

The probability distributions of the global response patterns (peak and residual SDRs) for all the 935 samples corresponding to each safety state is shown in Fig. 2-10. We are particularly interested in the amount of overlap (or lack thereof) in the distribution of peak and residual drifts between the safe and unsafe states. The 90% confidence interval for peak 1st story drift demands [Fig. 2-10 (a)] ranges from 0.4% to 2.1% for the safe state and 1.5% to 4.6% for the unsafe state. For peak 2nd story drift demands, the range is 0.5% to 2.9% for the safe state and 1.6% to 5.0% for the unsafe state, which indicates that the distribution for the two safety states is quite different. In contrast, the 3rd and 4th stories have significant overlap in the distribution of peak story drift ratios for the safe and unsafe samples, for example, the 4th story has 90% confidence intervals of 0.2% to 1.5% and 0.3% to 1.6% respectively. A similar trend can be observed for the distribution of residual drifts. There is relatively less overlap in the residual drift distributions between the unsafe and safe samples in the first two stories. For example, only unsafe samples have residual drift demands greater than 2.5% in the 1st and 2nd stories. The opposite is generally true for the 3rd and 4th stories where the residual drift distributions are very similar for the two safety states. The separation of the global EDP distribution in the first two stories suggests that they are more likely to be used as split boundaries that distinguish

between safe and unsafe states. In other words, the global EDPs in the first two stories are the potential strong predictors for classification.

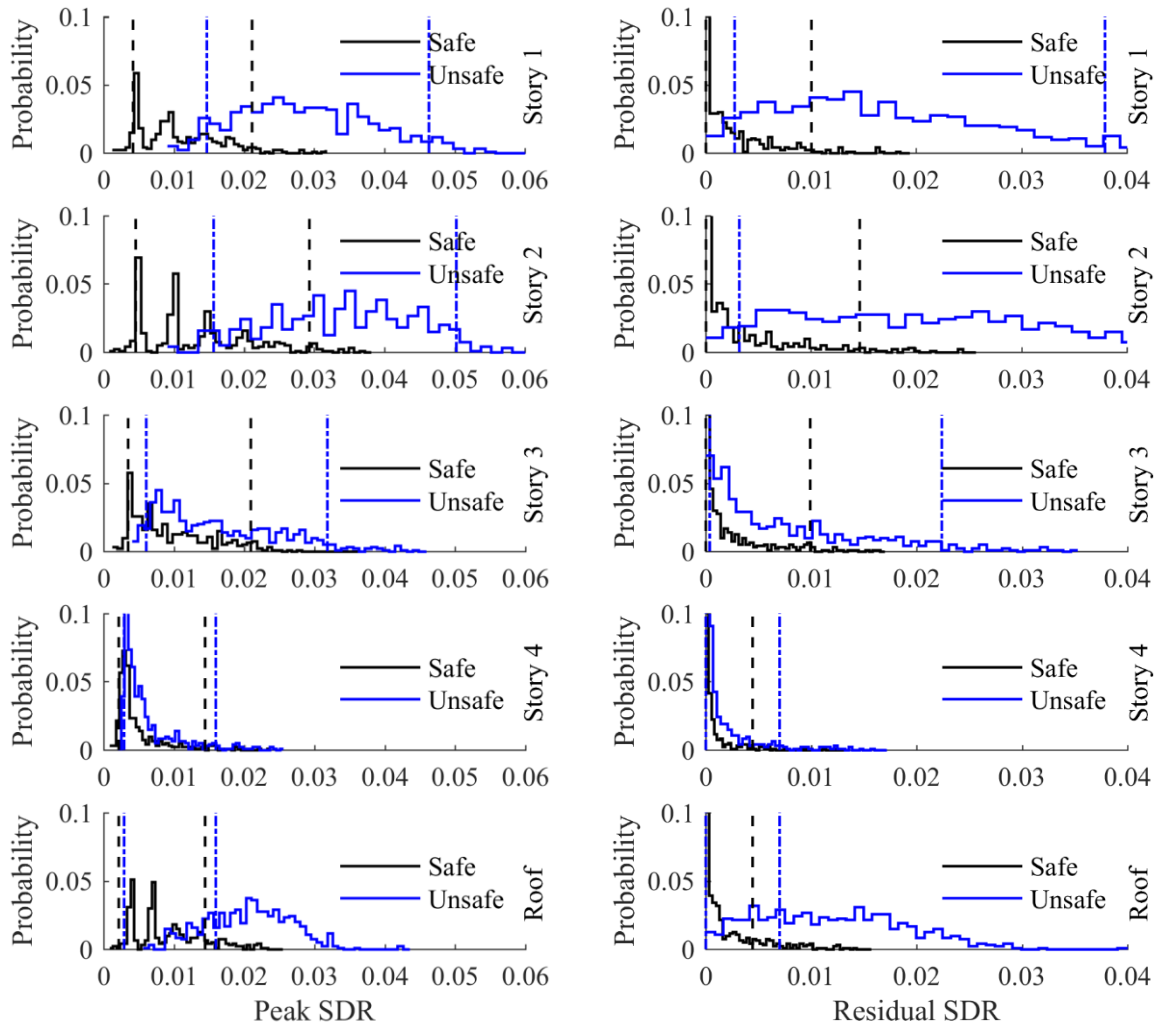

Fig. 2-10. Histogram of (a) peak and (b) residual SDRs for samples classified as safe and unsafe (the dashed and dot lines show the 90% confidence intervals for the safe and unsafe states respectively)

Fig. 2-11 shows the histograms of the peak plastic hinge rotations at the ends of a typical exterior column. From the figure, it can be seen that the plastic rotation demand distributions for the column hinges at the top of Stories 1 and 4 are very similar for safe and unsafe states, having 90% confidence intervals of 1.09×10^{-4} to 2.07×10^{-4} and 1.34×10^{-4} to 2.52×10^{-4} respectively. The distributions are more separated in the top hinge of the 2nd and 3rd story column, where the rotation demands are concentrated around 10^{-4} for the safe samples and

generally range from 10^{-3} to 5×10^{-2} for the unsafe ones. For the bottom hinges, only those in the 1st story have distributions that are clearly separated, where a possible split point (recall in Section 2.2.4) could be located within the range between 10^{-3} and 10^{-2}.

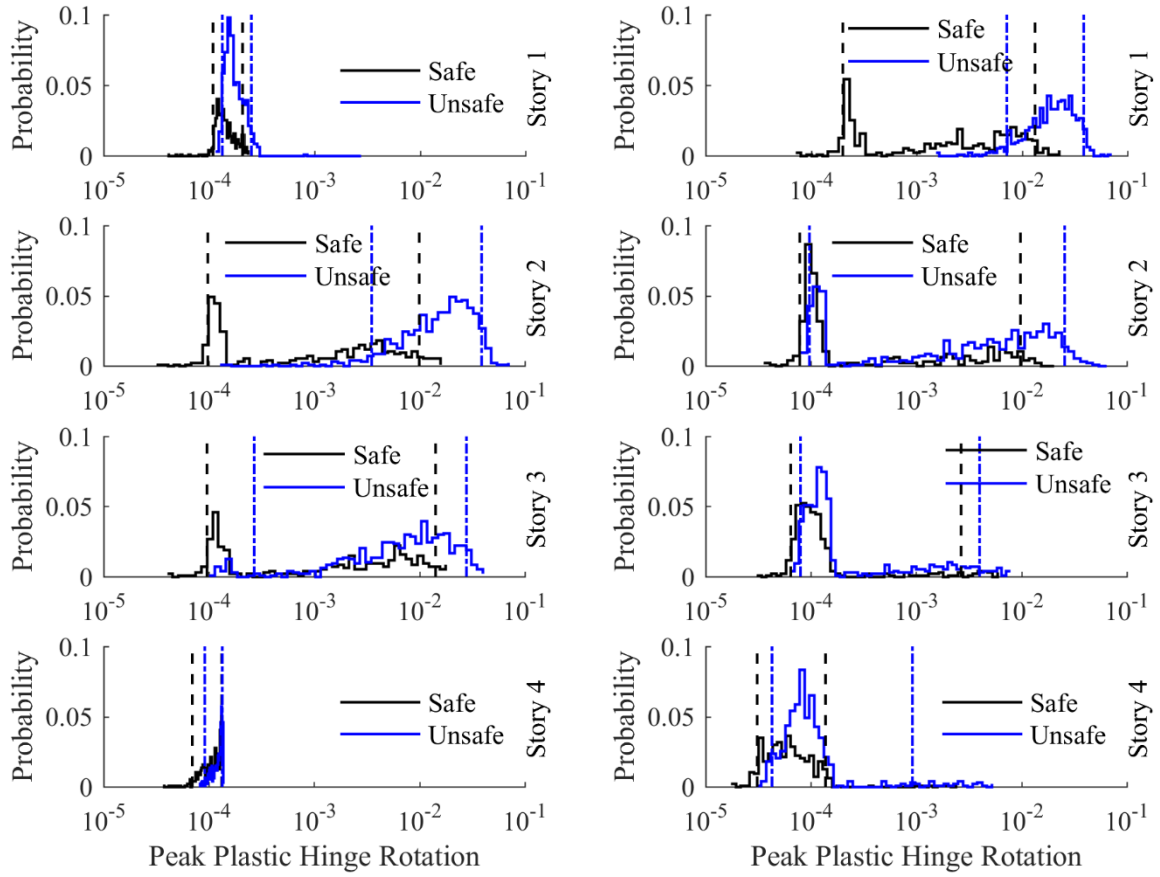

(a) (b)

Fig. 2-11. Histogram of peak plastic hinge rotations at the (a) top and (b) bottom ends of a typical column (the dashed and dot lines show the 90% confidence intervals for the safe and unsafe states respectively)

For each of the 935 samples, 100 damage patterns are generated using Monte Carlo simulation by combining the local response patterns with fragility curves that relate EDPs to the probability of exceeding discrete damage states. A single damage pattern is described by each component being assigned a damaged state. Each damage measure (DM) (or mode of component-level damage) consists of a pre-defined number of unique damage states [12]. The damage states for beam (DM1) and column (DM2) flexural damage are described in Table 2-1. The median EDP and dispersion that defines the lognormal fragility function for each damage state are also shown in Table 2-1. These fragility parameters are computed using the

methodology outlined in Section 3.8.4 of FEMA P58-1 [12] and exercised in Section 6.3 of FEMA P58-2 [13]. The median rotation demand for the flexural damage states is defined relative to the (capping) rotation demand at peak strength, θ_c.

In Fig. 2-12, the distribution of different damage states in beam and column hinges for the safe and unsafe states is compared using the 93,500 samples with distinct damage patterns. As observed in Fig. 2-12 (a) and (b), beam flexural damage is highest in the two lower floors. For the safe state of the exterior beams, 14.0% and 16.0% of the samples corresponding to the 2nd and 3rd floors respectively are in the lowest damage state (DM1-1). For those at the 3rd and 4th floors, only 5.2% and 2.9% respectively are in DM1-1. Almost no higher damage states occur among the safe state samples. For the unsafe state, 54.7%, 15.2% and 7.8% of exterior beams at the 2nd floor are in damage states DM1-1, DM1-2 and DM1-3, respectively. The proportions of those damage states in the 3rd floor are 32.4%, 5.6%, and 2.1%, respectively. Similar trends are observed for the interior beams at each floor, however, the damage was generally less severe than the exterior ones. Fig. 2-12 (c) shows that, for both the safe and unsafe states, observable damage to the top column hinges only occurs in the 2nd and 3rd story. For the safe state, DM2-1 occurs in 1.1% and 4.0% of the samples corresponding to the 2nd and 3rd stories respectively. Much more damage occurs in the samples associated with the unsafe state. 33.4%, 7.0% and 2.8% of top column hinges in the 2nd story and 18.2%, 2.7% and 0.7% in the 3rd story, are in DM2-1, DM2-2 and DM2-3, respectively. As indicated in Fig. 2-12 (d), less than 2.5% of the safe samples for the bottom column hinges in the first two stories are in DM2-1 and there is no observable damage elsewhere. In general, the distinct damage patterns between the safe and unsafe states provides the basis for building the advanced prediction models using machine learning algorithms.

Table 2-1. Structural component damage measures and median EDP and dispersion associated with each damage state

Damage Measure ID	Damage Measure	Damage State ID	Damage State Description	Median EDP	Dispersion
DM-1	Beam Flexural Damage	DM1-1	Residual crack widths > .06 in	$0.3\theta_c$	0.4
		DM1-2	Concrete spalling and exposed rebar	$0.7\theta_c$	
		DM1-3	Concrete crushing and buckling or fracture of rebar	$1.0\theta_c$	
DM-2	Column Flexural Damage	DM2-1	Residual crack widths > .06 in	$0.25\theta_c$	0.4
		DM2-2	Concrete spalling and exposed rebar	$0.55\theta_c$	
		DM2-3	Concrete crushing and buckling or fracture of rebar	$0.80\theta_c$	

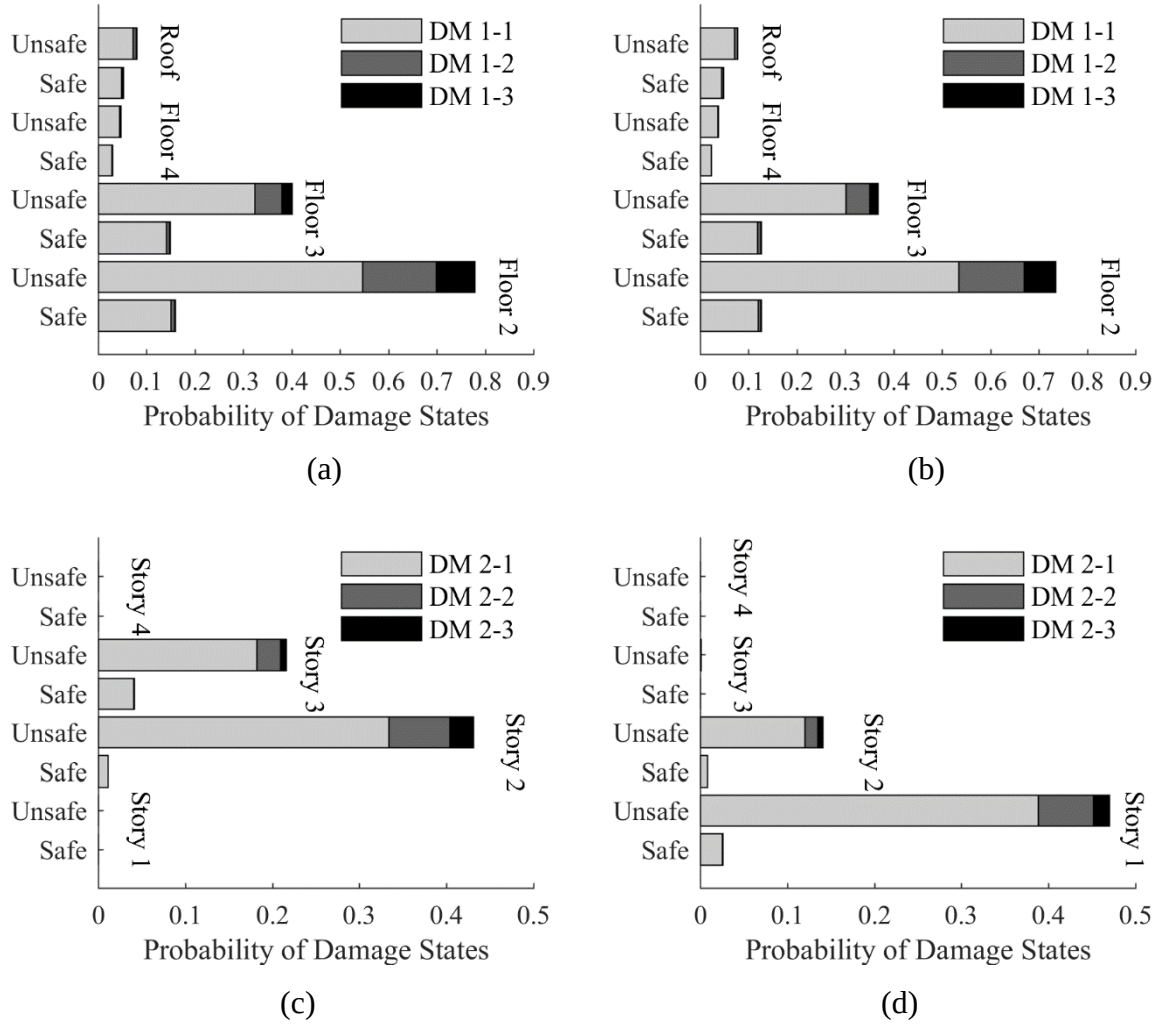

Fig. 2-12. Distribution of damage states for safe and unsafe samples at (a) exterior beam end, (b) interior beam end, (c) top column end and (d) bottom column end

2.3.3 Machine Learning Based Safety State Prediction Models

Predictive models are built using two different datasets: 1) 935 classified response patterns that comprise only global EDPs and 2) 93,500 damage patterns sampled from classified local EDPs. Each dataset is partitioned into two subsets: 75% of the samples are used for training and the remaining 25% are held-out for testing the performance of the proposed models. 10-fold cross-validations are performed using training subsets to find the optimal predictive models with the least amount of overfitting given specific tuning parameters. To further reduce the possible bias in dividing the training data into 10 folders, the cross-validation is repeated 3 times with random partitions. Basic CART models are built as well as advanced Random Forests models.

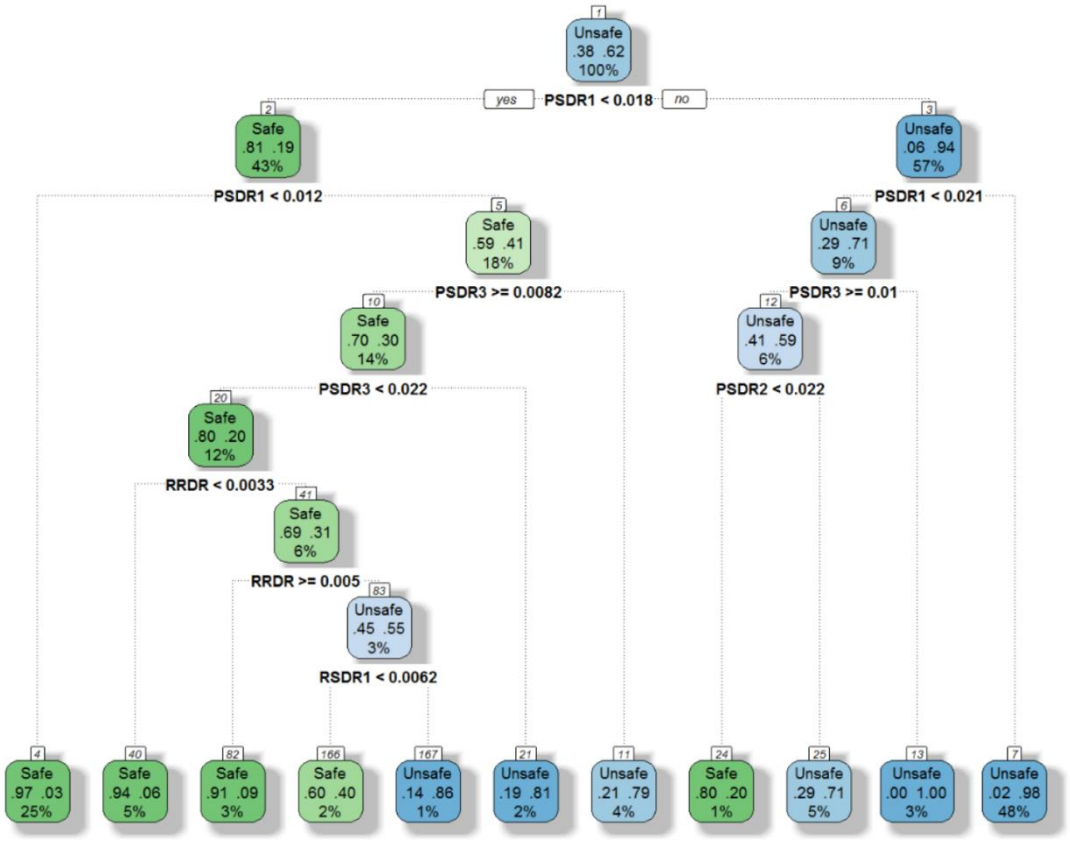

Fig. 2-13. Example CART model with complexity parameter of 0.01 and trained using response patterns, where PSDR*i* denotes the PSDR at Story *i*, RSDR*j* denotes the RSDR at Story *j*

An example CART model constructed using the training subset of the response pattern dataset is presented in Fig. 2-13. The root node has 38% safe samples and 62% unsafe samples, which would result in an unsafe prediction based on the majority vote if no more splits are created in the model. At this initial step, $|N| = 1$, $\pi_n = 1$, and the Gini Index computed using Equation 2.1 is 0.47, indicating a very high impurity when compared with the maximum GI of 0.5 for a binary dataset. By testing the possible splits associated with the predictors, the algorithm finds the optimal point of peak $SDR = 0.018$ and partitions the original sample space into two subspaces. 43% of the samples have peak $SDR < 0.018$and the remaining 57% have peak $SDR \geq 0.018$. The overall GI after the split decreases to 0.197, which represents a substantial reduction of 0.274. Next, within each subspace, the algorithm is repeated in search of the next optimal split point, which is again peak SDR but at a different point, 0.012. After this split, the GI is computed as 0.166, which represents a 0.031 decrease. If the model stops here, it would only have two splits and three leaf nodes. Predictions can be made with more than 90% probability in the cases where peak SDR is less than 0.012 or larger than 0.018, but

poor performance with only 59% probability is found when the SDR falls between those two values. Therefore, the tree keeps growing until the reduction of the overall GI is less than the predefined complexity parameter. Finally, a 7-layer tree with 11 leaf nodes is constructed after a total of 9 partitions, which has more than 90% classification accuracy for approximately 84% of the training subsets, and only 2% of all the predictions have an accuracy less than 70%.

Fig. 2-14 illustrates the parameter tuning process for the CART and Random Forests models trained using the response patterns. In Fig. 2-14 (a), the area under the ROC curve, sensitivity and specificity are plotted versus complexity parameter ranging from 0.5 to 1×10^{-6}. It can be observed that the area under the ROC curve and specificity increase as the complexity parameter decreases, while the sensitivity decreases. All three performance measures remain almost unchanged after the complexity parameter exceeds 0.001. Since the unsafe state is more critical, sensitivity is more valued than specificity in this study so the optimal complexity parameter is chosen as 0.05. Fig. 2-14 (b) demonstrates how the number of predictors considered at each split and the number of trees are used to tune the Random Forests model. The former ranges from 2 to 10 with an increment of 2 and the latter is defined by the set {10, 20, 30, 40, 50, 100, 150, 200, 250, 300}. As shown in Fig. 2-14 (b), the area under the ROC curve tends to increase as the number of trees increases. The model that allows 10 predictors for further splits has the lowest area while the models allowing to 2, 4, 6 and 8 predictors have comparable ones. Fig. 2-14 (c) and (d) show that the models that allow more predictors for selecting each split generally have better performance in terms of the sensitivity but are less competitive for specificity. By synthesizing the above observations, the optimal tuning parameters are selected as 6 predictors considered at split points and 250 trees for bagging.

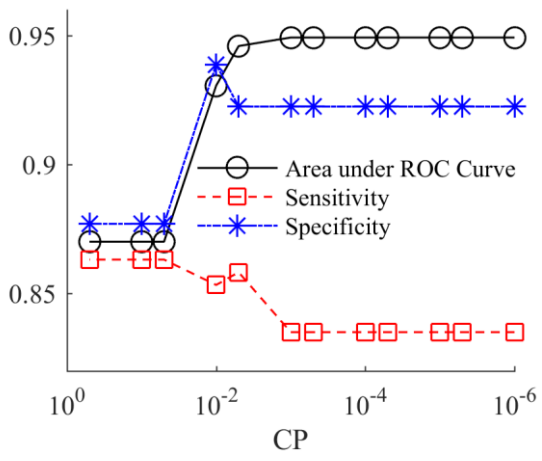

(a)

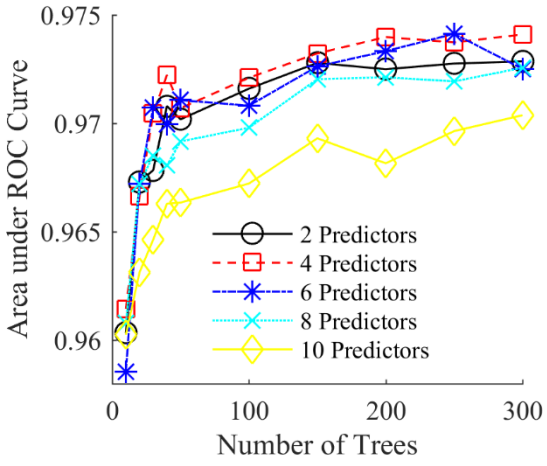

(b)

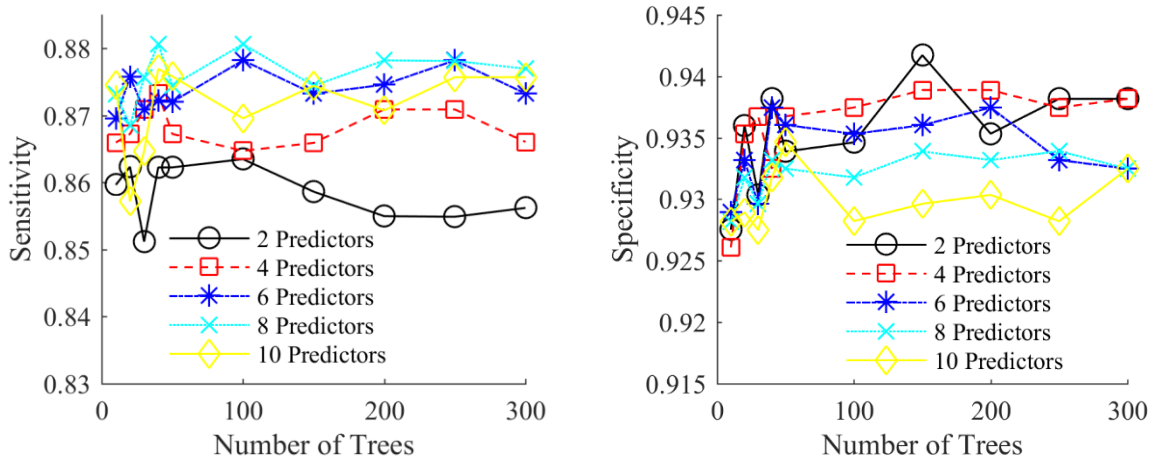

(c) (d)

Fig. 2-14. Parameter tuning for (a) CART and (b)-(d) Random Forests models trained using response patterns

Parameter tuning is also performed for the models trained using the damage patterns and the results are summarized in Fig. 2-15. A complexity parameter value of 1×10^{-6} is chosen as optimal as it maximizes the area under the ROC curve and balances the sensitivity and specificity, as shown in Fig. 2-15 (a). Fig. 2-15 (b) shows that the area under the ROC curve increases as the number of trees increases. The model with 10 predictors at each split is the best and is clearly distinguished from the other four. Fig. 2-15 (c) and (d) show that the model with only 1 predictor at each split has the lowest performance for sensitivity but highest performance for specificity, while all the other models are comparable. Based on these observations, the optimal model allows 5 predictors to be considered at split points and uses 150 trees.

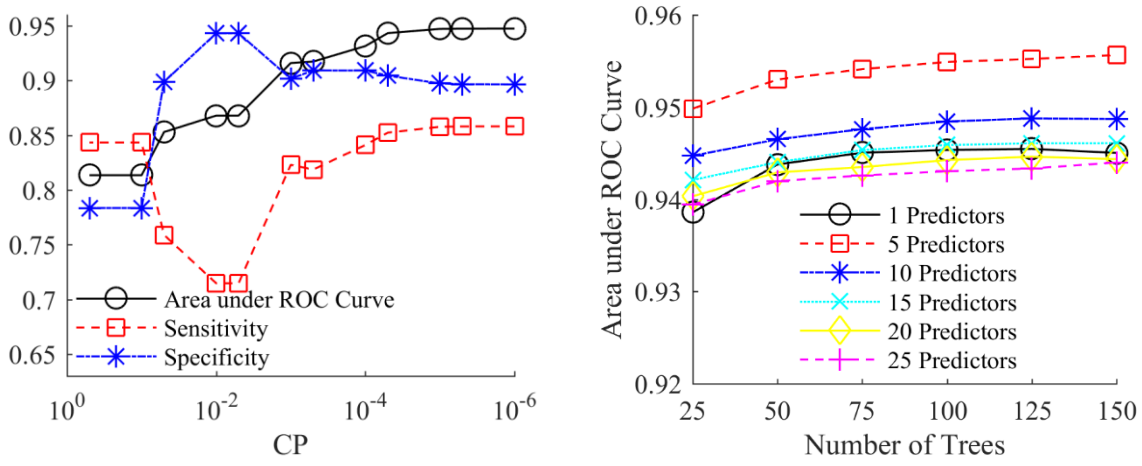

(a) (b)

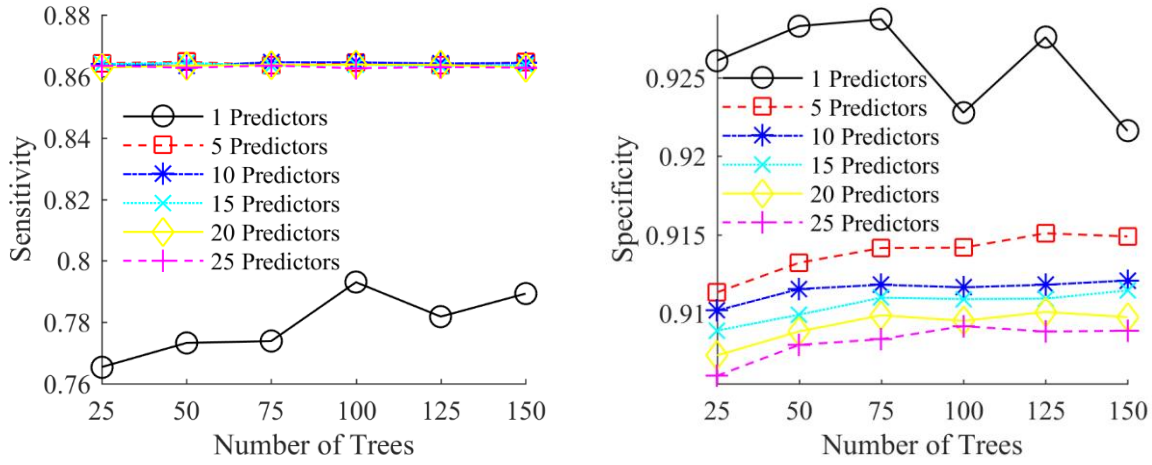

(c) (d)

Fig. 2-15. Parameter tuning for (a) CART and (b)-(d) Random Forests models trained using damage patterns

Table 2-2 summarizes the performance measures including sensitivity, specificity, and accuracy for the final CART and Random Forests models using 25% held-out testing datasets. Predictions obtained from all the final models are compared with their corresponding reference (real) states. 240 testing samples with response patterns are employed in the final CART model, where 74 true negative and 143 true positive predictions are observed. Only 19 cases are recognized as unsafe (negative) when they are actually safe (positive), while 4 unsafe ones are misclassified as safe. The overall accuracy of 90.4% is achieved, and more importantly, the false negative rate is only 1.7%, giving an acceptably low rate of risky predictions. The Random Forests model has similar behavior and only performs slightly better than the CART model, indicating that a single tree might be able to capture the key characteristic of the response patterns. 22900 testing damage patterns are fed into the final CART model, of which 7219 and 12646 correct predictions are found for the safe and unsafe states respectively. The false positive rate is 15.1% and the more critical false negative rate is 12.2%. Considerably better performance is observed for the Random Forests model. The improvements of 1.46%, 1.85% and 0.8% on accuracy, sensitivity, and specificity seem small, but in fact, there is a 15.2% (267 out of 1754) reduction in the critical false negative rate compared to the CART model.

The predictive models based on the response patterns have an overall slightly better performance than the damage pattern models. A possible explanation is that additional randomness is introduced by using component fragility curves and Monte Carlo simulation to generate the damage pattern from the EDPs. Moreover, the precision of the predictor information is somewhat reduced when continuous EDPs are converted to discrete damage

states. With that being said, it should be noted that exact or real EDP values are assumed in the response pattern models even though the field instruments used to record these EDPs may introduce measurement errors, which could potentially lower the performance. This issue is not addressed in the current study. More importantly, unlike the response patterns which require pre-installed instruments, the damage patterns can be more easily obtained after an earthquake through visual inspection.

Table 2-2. Performance measures of final models based on testing datasets

Dataset	Response Dataset				Damage State Dataset			
Model	CART		Random Forests		CART		Random Forests	
Confusion Matrix	Actually Safe (Negative)	Actually Unsafe (Positive)	Actually Safe (Negative)	Actually Unsafe (Positive)	Actually Safe (Negative)	Actually Unsafe (Positive)	Actually Safe (Negative)	Actually Unsafe (Positive)
Predicted Safe (Negative)	74	4	76	4	7219	1754	7287	1487
Predicted Unsafe (Positive)	19	143	17	143	1281	12646	1213	12913
Sensitivity	0.97		0.97		0.88		0.90	
Specificity	0.80		0.82		0.85		0.86	
Accuracy	0.90		0.91		0.87		0.88	
95% CI	0.86-0.94		0.87-0.95		0.86-0.87		0.88-0.89	

2.4 Conclusion

A machine learning framework for assessing post-earthquake structural safety is developed by integrating probabilistic seismic demand analysis, component-level damage simulation and robust assessments of the residual collapse capacity. Multiple instances of a damaged structure are created by subjecting a nonlinear structural model to a suite of "damaging" ground motions scaled to achieve pre-defined target drift demands. The spatial distribution of EDPs from a single damaging analysis is described as a response pattern. The term damage pattern is used to describe the spatial variation of component-level damage, which is generated through Monte Carlo Simulation, by coupling local EDPs with damage fragility functions. The collapse capacity of the intact and damaged structures is assessed by performing incremental dynamic analysis using a suite of "collapsing" ground motions. For the damaged structure, the model is subjected to a single damaging record followed by a collapsing ground motion whose spectral intensity is incrementally increased in order to cause collapse. The ratio of the median collapse

capacity of the damaged and intact structure is used as the measure of the reduced collapse safety and the criterion for the post-earthquake safety state (safe or unsafe) of the building. A robust dataset comprising of 935 response patterns, 93,500 damage patterns, and their corresponding safety state is used to define a classification problem.

Machine learning algorithms including CART and Random Forests are implemented to map the response and damage patterns to their classified structural safety states, where the predictor space is recursively partitioned to capture the underlying relationship. Previously developed post-earthquake structural evaluation methods have based the safety state criteria on the exceedance of pre-defined response demand levels or damage state ratios within individual structural component groups. In contrast to prior approaches, the outcome of the proposed framework consists of classification trees, each comprising a high-dimension space of response and damage patterns partitioned into multiple subspaces. Given an arbitrarily observed pattern for a damaged structure, each tree is intelligently searched to find the matching subspace, which will serve as the basis for classifying the safety state of the structure. The result is a discrete probability distribution of the structural safety state, which serves as an indicator of the confidence of the prediction.

The proposed methodology is applied to a 4-story reinforced concrete special moment frame building located in a region of high seismicity. The results show that, although different response and damage patterns exist for the safe and unsafe structural states, they cannot be separated by assigning a certain criterion for any individual EDP or damage measure. Such a criterion would result in considerable overlap between the two safety states. The predictive models presented in this study, which are trained using machine learning algorithms, can provide predictions with high performance in terms of accuracy, sensitivity, and specificity. The prediction accuracy is above 90% for both the CART and Random Forests models when applied to response patterns with unknown safety states. A minimum accuracy of 86% is achieved for damage patterns with unknown safety states. Relatively high sensitivity is also observed in the prediction models developed for the case study, which is critical for reducing the rate of high-risk erroneous predictions i.e. model predicts safe when the building is unsafe.

The proposed framework could be used for rapid probabilistic assessment of whether a damaged building is safe to reoccupy following an earthquake. Additionally, the trees generated by the machine learning algorithms could be used to prioritize field inspections following an earthquake. Moreover, the probabilistic safety state predictions could be used in

community resilience evaluations and individual building life-cycle performance assessment and optimization.

CHAPTER 3: Structural Modeling, Probabilistic Seismic Hazard Analysis and Ground Motion Selection of Tall Buildings with Core Walls and Special Moment Frames

---

This chapter is partially adopted from the following study:

Zhang, Y., Burton, H. V., Shokrabadi, M. & Wallace J. W. (2019). Seismic risk assessment of a 42-story reinforced concrete dual-system building considering mainshock and aftershock hazard. ASCE Journal of Structural Engineering (accepted for publication).

This chapter introduces a 42-story dual system tall building with core walls and special moment frames, which will be used as the archetype structure for the analyses performed from Chapter 4 to 6. The PSHA for the given site located in Southern California (118.25° W, 34.05° N), is conducted and a set of 34 pairs of as-recorded mainshock and aftershock ground motions are selected accordingly for the NLRAs in the following chapters.

3.1 Building Description

The reinforced concrete dual system (shear wall and moment frame) building used in the current study, which is denoted as Building 2B in the PEER TBI report [52], has 42 stories above the ground floor, four basement levels and a penthouse at the roof level. The isometric view and plan layout are shown in Fig. 3-1 (a) and (b) respectively. The core walls, which are labeled Pier 1 through Pier 3 in Fig. 1(b), are planar and L-shaped and are connected with coupling beams. A performance-based approach using the 2008 version of the LATBSDC guidelines [53] was adopted in the design. The structure was evaluated for serviceability and collapse prevention performance levels. The seismic demands for the serviceability level assessment were obtained from a site-specific response spectrum analysis corresponding to a 25-year return period event assuming 2.5% viscous damping. Up to 20% of the deformation-controlled components were permitted to reach 150% of their strength capacity at the serviceability level [52]. The minimum base shear requirement in 2008 LATBSDC was waived and the ACI 318-08 [43] strength reduction factors were applied to evaluate deformation-controlled actions at the service level. As part of the design process, a three-dimensional model of the structure was constructed in Perform-3D and analyzed using seven pairs of spectrally matched ground motions. NRHAs were used to evaluate the collapse prevention performance

level at the maximum considered earthquake (MCE) hazard level (2475-year return period). The reported period of the first three modes was 4.28sec, 3.87sec, and 2.26sec, respectively. Additional design details are provided in the TBI case study [52].

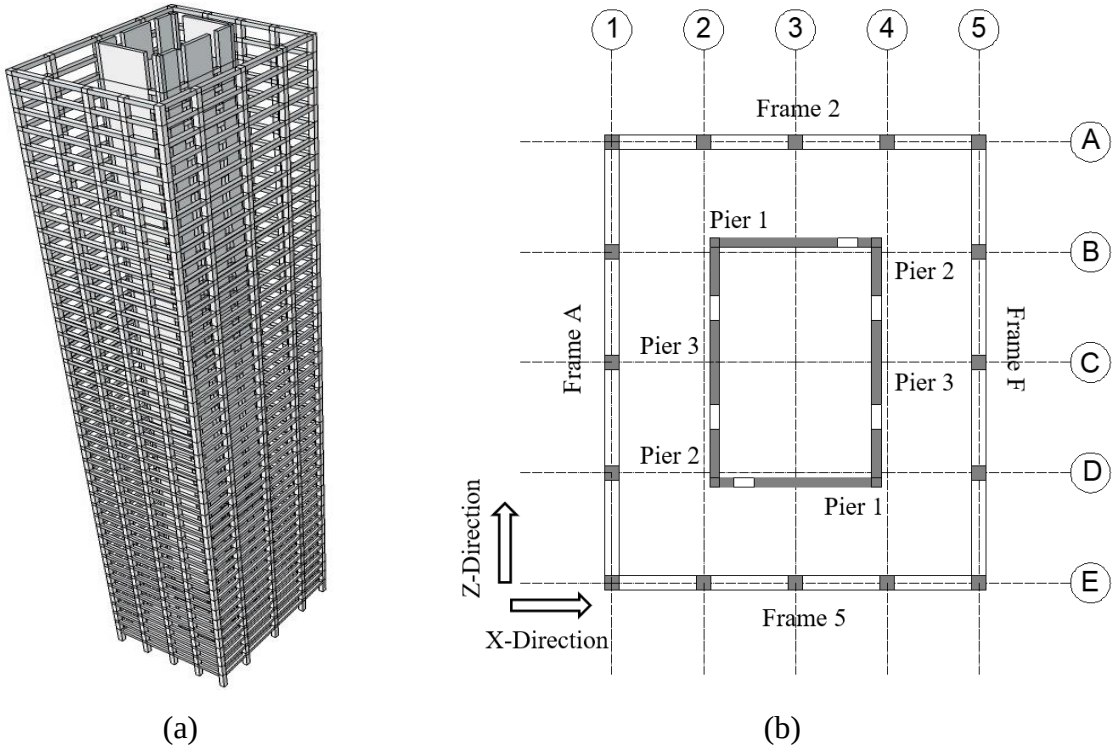

(a) (b)

Fig. 3-1 (a) Isometric view and (b) plan layout of the dual lateral resisting system

3.2 Structural Modeling

A three-dimensional structural model of the lateral force resisting system (gravity system not included) of the tower (basement levels not included) is constructed in OpenSees [44]. A rigid diaphragm, which is commonly used for the tower portion of tall buildings, is incorporated at all suspended floor levels by constraining the horizontal translational and vertical rotational degrees of freedom. The additional flexural strength and stiffness provided by the floor slabs is included in the calibration of coupling beams. The seismic mass is lumped at the center of mass at each floor. Expected gravity loads ($D + 0.25L$) are used in the model. The expected strengths of the concrete and steel are used by applying factors of 1.30 and 1.17 to the nominal values respectively. The damping is set as 2.5% at the periods of 0.2 and 0.9 of the fundamental period of the structure [52]. The lower bound of 0.2 is used to avoid over-damping in higher modes and is consistent with the TBI and LATBSDC guidelines. The upper bound of 0.9 is less than the 1.5 value recommended in the latest documents (LATBSDC 2017, TBI 2017). Therefore, the first mode response could be slightly overdamped. However, since

Rayleigh damping is low (2.5%), the impact is not significant and will not influence the key findings presented in this chapter. A leaning column is used to account for additional P-Delta effects resulting from the expected loads on the gravity system which is not explicitly modeled. The leaning column is axially rigid, has no lateral stiffness and the horizontal translational degrees of freedom of the end nodes are constrained to the floor nodes. The core walls and moment frame columns are fixed at the base.

The primary energy dissipation elements are the coupling beams and the core wall piers and moment frame beams serve as a secondary source of energy dissipation. The hysteretic behavior of these three types of elements is modeled to account for cumulative damaging effects of sequential ground motions.

3.2.1 Special Moment Frame

The moment frames and coupling beams are defined using elastic beam-column elements with flexural plastic hinges at the ends. While fiber models are able to explicitly account for P-M interaction, they are quite cumbersome for capturing rebar buckling. On the contrary, a flexural hinge model is more efficient in terms of computational expense and has been widely calibrated against physical experiments to properly capture the strength and stiffness loss associated with rebar buckling and is therefore deemed appropriate for this study. The nonlinear behavior of the flexural hinges in the frame beams and columns is based on the peak oriented hysteretic model developed by Ibarra et al. [45] and the predictive equations developed by Panagiotakos and Fardis [46] and Haselton [47] are used to calibrate the hysteretic parameters.

3.2.2 Shear Wall and Coupling Beam

The two-dimensional multiple vertical line element model (MVLEM) [54,55] is adopted and used in the three-dimensional model to capture the non-linear behavior of core walls. As shown in Fig. 2, two rigid beam elements are connected vertically using a set of two-node-link elements, where the parallel material models are used to integrate contributions from concrete and reinforcement. Zero-length elements are used to capture the shear behavior at the rotation center of wall panels. The L-shaped walls (Pier 1 and Pier 2) are simulated by two such models in each of the two directions with the vertical displacements coupled at the joint nodes. To achieve the balance between accuracy and efficiency of such a large numerical model, sensitivity analyses are conducted for modeling core walls with 4, 6 and 8 vertical links. The

confinement effects including an increase in both strength and ductility of the core concrete are incorporated using the rules suggested by Mander et al. [56]. This model is very similar to the planar (two-dimensional) version and the model that exists in Perform-3D. Prior studies have shown that such models reasonably capture the response of T- and C-shaped walls subjected to in-plane [55,57] and biaxial loading [58]. The periods of the first three modes of the model developed for this study were $4.08\,sec$, $3.37\,sec$ and $2.53\,sec$ respectively, which are comparable with the values reported in the TBI report [52]. Moreover, the MCE-level global and local demands from the OpenSees model developed for the current study was found to be comparable with those obtained from the Perform-3D model used in the Moehle et al. study. For the coupling beams with diagonal reinforcement, the flexural hinge parameters are based on test results by Naish et al (2013).

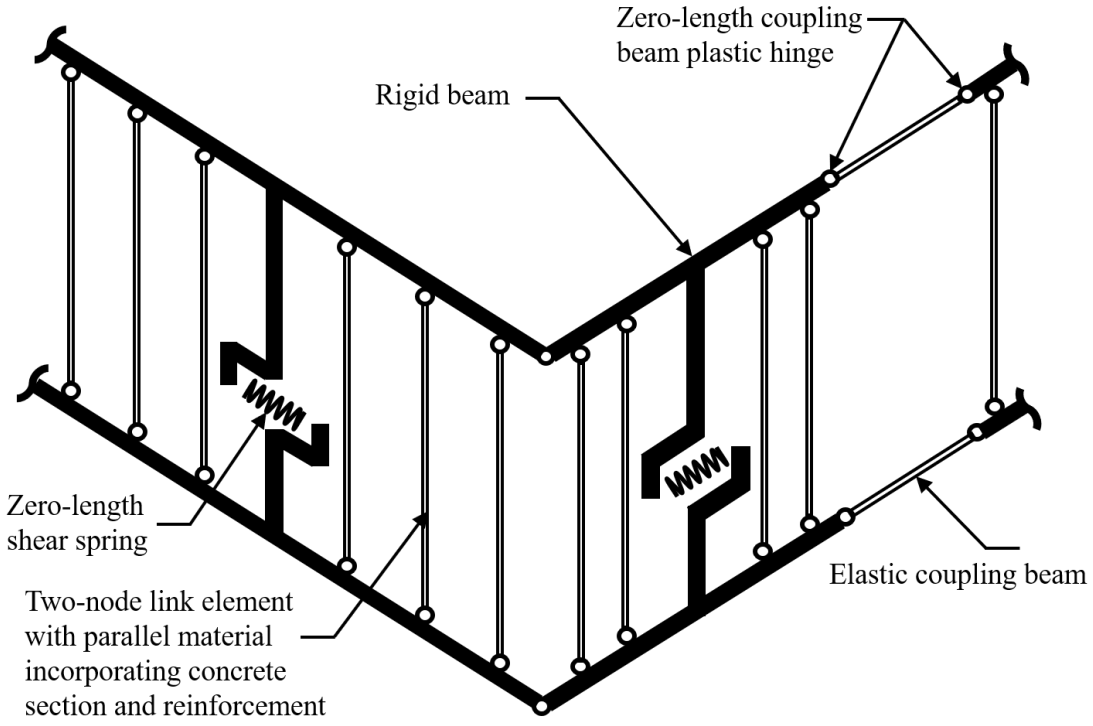

Fig. 3-2 A schematic illustration of shear wall modeling in OpenSees

3.3 Probabilistic Seismic Hazard Analysis and Ground Motion Selection

3.3.1 Seismic Hazard Analysis

The goal of PSHA is to provide an estimate of the mean annual rate of exceeding some intensity measure for a specific site. The PSHA methodology for mainshocks assumes a

homogeneous Poisson distribution for the recurrence rate of earthquakes. However, it has been well established that the rate of occurrence of aftershocks decays with the time elapsed since the occurrence of the causative mainshock, which is typically modeled using the modified Omori's law [60]. Utilizing the relationship by Reasenberg and Jones [61] for the occurrence rate of aftershocks, Yeo and Cornell [62] proposed an Aftershock PSHA (APSHA) methodology where the constant rate of occurrence of earthquakes in conventional PSHA is replaced by a time-varying rate. The relationship that forms the basis of both PSHA and APSHA is shown in Equation 3.1 for a single fault, and the total seismic hazard at the building location is obtained through the summation of the individual hazard from all the contributing faults.

$$\lambda_{IM,n}(im) = \nu_n \iiint_{M,R,\varepsilon} G[IM > im|\, M,R,\varepsilon]\, f_M(m) f_R(r) f_\varepsilon(\varepsilon) dM dR d\varepsilon \tag{3.1}$$

$$\nu_n^{AS}[t_0, t_1] = \left(10^{a+b(M_m - M_0)} - 10^a\right) \frac{(t_1 + c)^{1-\rho} - (t_0 + c)^{1-\rho}}{1-\rho} \tag{3.2}$$

where, in Equation 3.1, $G[IM > im|M,R,\varepsilon]$ is an indicator function that takes on the value of one if $IM > im$ and zero otherwise, n is the identification number of each fault being considered; $\lambda_{IM,n}(im)$ is the rate of occurrence of seismic events having $IM > im$ generated by fault n within a specific time window (usually one year); ν_n is the rate of occurrence of seismic events with magnitudes larger than a predefined lower-bound associated with fault n. When performing APSHA, the time-invariant ν_n in the conventional PSHA is replaced with $\nu_n^{AS}[t_0, t_1]$ in Equation 3.2, which gives the rate of aftershocks during the time interval $[t_0, t_1]$. a and b in Equation 3.2 are constants that define the magnitude distribution; c and ρ define the temporal decay in the number of aftershocks and are adopted from a generic California model [61]; M_0 and M_m are the minimum and maximum magnitudes of aftershocks, where M_m is taken as the magnitude of the causative mainshock. Both the upper and lower limits of the time window are defined as the time elapsed since the occurrence of the mainshock.

APSHA is used in this study to develop an aftershock seismic hazard curve for the building site located in Southern California ($118.25°$ W, $34.05°$ N, $\mathrm{Vs}_{30} = 360 m/s$), which is shown in Fig. 3-3 alongside the mainshock hazard curve, which was obtained using conventional PSHA. The hazard curves are presented in the form of the mean annual rate of exceeding Sa_{T1}. A total of 49 faults contribute to the hazard at the site of interest. However, it is worth noting

that, an implicit assumption in APSHA is that a mainshock has already occurred and the seismic hazard due to the following aftershocks is being evaluated. Since it is highly unlikely for simultaneous mainshocks to occur on the multiple faults that contribute to the seismic hazard at the location of the building, the APSHA curve is developed solely for the fault that contributes the most to the mainshock seismic hazard at the location of the building. On the other hand, the mainshock seismic hazard curve is developed accounting for all the sources that are likely to contribute to the seismic hazard at the site location of the building. APSHA is performed for a duration of one year after the mainshock, which is considered long enough for the hazard to decrease to a negligible level. The ground motion prediction equations developed by Boore and Atkinson [63] are used to perform both PSHA and APSHA. The minimum magnitude of mainshocks and aftershocks is taken as 5.0 since events with smaller magnitudes are not expected to induce notable damage in code-conforming structures and the magnitude of the largest aftershock is assumed to be equal to that of the largest mainshock.

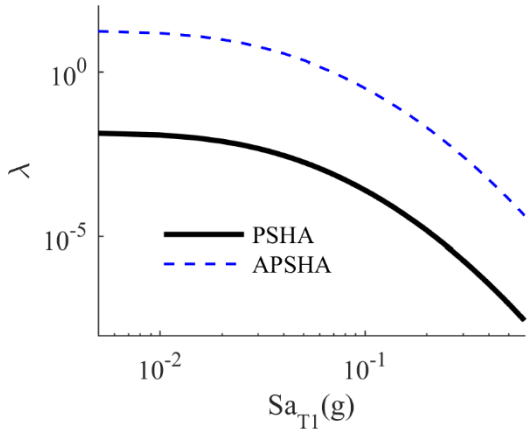

Fig. 3-3. PSHA for all the faults and ASPHA for the fault with the highest contribution to the mainshock hazard

3.3.2 Ground Motion Selection

A set of 34 ground motion sequences, each with one pair of mainshock and aftershock records, are selected and used for the NRHAs of the 42-story dual system tall building. All record-pairs are from actual earthquake sequences (meaning each pair was recorded in the same sequence) including the Imperial Valley 06, Northridge, Livermore, Coalinga, Landers, Mammoth Lakes 01, Chalfant Valley 02, Umbria Marche, Irpinia, Darfield and Chi-Chi earthquakes, and were obtained from the NGA West2 database [64]. The classification of the ground motions into mainshocks and aftershocks is based on the time and distance windowing algorithms by Knopoff and Gardner [65] and Wooddell and Abrahamson [66]. A magnitude-

dependent time window and a distance threshold of 40km measured in terms of the centroidal Joyner-Boore distance [66] is used to identify the aftershock ground motions following a mainshock event. The magnitudes of the mainshocks ranges from 5.8 to 7.6 whereas the aftershocks' magnitudes are between 4.7 and 6.7; response spectra for each case are presented in Fig. 3-4. The detailed properties of the selected ground motions are provided in Table 3-1.

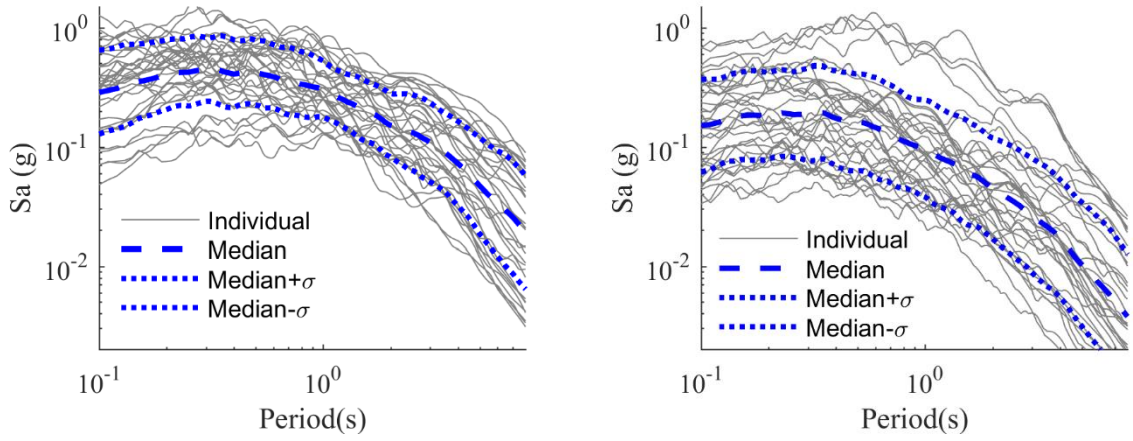

Fig. 3-4. (a) Mainshock and (b) aftershock ground motion spectra

Table 3-1. Properties of the mainshock-aftershock ground motion sequences

ID	Event name	Mainshock ground motion			Aftershock ground motion		
		M_w	R_{jb} (km)	Vs_{30} (m/s^2)	M_w	R_{jb} (km)	Vs_{30} (m/s^2)
1	Imperial Valley 06	6.53	10.4	208.7	5.01	11.2	205.6
2	Imperial Valley 06	6.53	7.3	192.1	5.01	10.4	203.2
3	Imperial Valley 06	6.53	0.1	264.6	5.01	10.6	202.9
4	Imperial Valley 06	6.53	4.0	205.6	5.62	9.8	193.7
5	Imperial Valley 06	6.53	1.4	203.2	5.90	19.4	362.4
6	Imperial Valley 06	6.53	0.6	210.5	5.90	6.5	193.7
7	Northridge	6.69	20.7	450.3	5.20	20.8	508.1
8	Livermore	5.80	25.0	403.4	5.42	30.0	517.1
9	Coalinga	6.36	24.0	274.7	5.38	13.5	352.2
10	Coalinga	6.36	42.0	178.3	5.38	12.6	286.4
11	Coalinga	6.36	29.5	246.1	5.38	13.3	617.4
12	Coalinga	6.36	39.0	294.3	5.77	11.1	474.2

13	Coalinga	6.36	32.9	266.7	5.77	11.1	474.2
14	Coalinga	6.36	27.5	648.1	5.77	12.1	458.1
15	Landers	7.28	69.2	382.9	6.46	78.2	282.1
16	Landers	7.28	144.9	269.3	6.46	107.3	339.6
17	Mammoth Lakes 01	6.06	15.5	537.2	4.73	5.2	353.2
18	Chalfant Valley 02	6.19	17.2	303.5	5.44	24.8	303.5
19	Umbria Marche, Italy	6.00	17.3	293.0	5.30	35.3	492.0
20	Irpinia, Italy	6.90	10.8	382.0	6.20	14.7	496.5
21	Darfield, New Zealand	7.00	7.3	326.0	6.20	41.1	337.0
22	Darfield, New Zealand	7.00	25.4	206.0	6.20	14.4	280.3
23	Darfield, New Zealand	7.00	30.5	255.0	6.20	5.6	187.0
24	Darfield, New Zealand	7.00	7.1	263.2	6.20	3.3	198.0
25	Darfield, New Zealand	7.00	24.6	206.0	6.20	4.9	194.0
26	Darfield, New Zealand	7.00	1.5	295.7	6.20	85.4	638.4
27	Darfield, New Zealand	7.00	20.9	247.5	6.20	40.6	295.7
28	Chi-Chi	7.62	9.6	427.7	6.20	80.9	190.6
29	Chi-Chi	7.62	29.5	226.0	6.20	72.3	497.5
30	Chi-Chi	7.62	16.0	233.1	6.20	28.7	277.5
31	Chi-Chi	7.62	78.7	203.0	6.20	38.9	226.0
32	Chi-Chi	7.62	9.9	258.9	6.20	55.5	210.0
33	Chi-Chi	7.62	56.1	1525.9	6.20	31.8	544.7
34	Chi-Chi	7.62	55.6	494.8	6.20	36.4	233.1

CHAPTER 4: Pattern Recognition Approach to Assess the Residual Structural Capacity of Damaged Tall Buildings

This chapter is adopted from the following study:

Zhang, Y., & Burton, H. V. (2019). Pattern recognition approach to assess the residual structural capacity of damaged tall buildings. Structural Safety, 78, 12-22.

4.1 Introduction and Background

The vertical extent and concentration of people and services in tall buildings is such that the adverse impact of earthquake damage can extend far beyond their footprint. When a tall building suffers earthquake damage, the ability to quantify its residual structural capacity is essential to informing whether it can be temporarily or permanently re-occupied (before repairs) in the aftershock environment when the seismic hazard is elevated. In the United States and other parts of the world, the ATC-20 [22,23] guidelines are used to evaluate the post-earthquake safety and occupiability of damaged buildings. Buildings are assigned red (unsafe to occupy), yellow (limited entry) and green (safe to reoccupy) tags based on the extent of damage to key structural and non-structural components. In terms of structural safety, the document generally relies on the judgment of structural engineers to make the link between the damage to individual components and the reduction in lateral load carrying capacity. As a result, numerical modeling is often used to augment engineering judgment by explicitly linking component-level damage to system level residual structural capacity.

There have been numerous studies that have employed NRHAs using sequential ground motions to evaluate residual structural capacity of earthquake-damaged buildings. Some studies have focused on post-mainshock or aftershock vulnerability (e.g. Raghunandan et al. [32]; Jeon et al. [67]) by assessing the likelihood that a mainshock-damaged building will exceed a predefined limit state (e.g. drift limit exceedance, collapse) given a specific ground motion intensity. Others have coupled the reduction in structural capacity of mainshock-damaged buildings with time-dependent aftershock hazard, to provide risk-based assessments (e.g. Yeo and Cornell [68]; Nazari et al. [69]; Shokrabadi and Burton [70]). To complement the ATC-20 procedure, Burton and Deierlein [33] developed a methodology that integrates component-level visual damage simulation with collapse performance assessment to evaluate post-earthquake structural safety. Triggering damage quantities for individual structural

components were established based on the implications of increased collapse vulnerability of the damaged building. The shortcoming of this methodology stemmed from the use of a one-dimensional mapping between component-level damage and system-level vulnerability. To address this limitation, Burton et al. [71] used multivariate statistical models to link physical damage indicators, structural response quantities and mainshock intensity to aftershock collapse vulnerability. The methods considered included Ordinary Least Squares (OLS), Best Subset Regression, Least Absolute Shrinkage and Selector Operator (LASSO), Principal Components Analysis and Kernel Ridge Regression. Zhang et al. [72] utilized the Random Forests algorithm to probabilistically classify earthquake-damaged buildings into safe and unsafe states based on the link between response and damage patterns and the reduction in collapse safety. The methodology was applied to a 4-story reinforced concrete (RC) frame building.

In contrast to the low- or mid-rise structures that have been the focus of earlier studies, two main challenges arise when evaluating the residual structural safety of earthquake-damaged tall buildings. Because of the large number of components, the response patterns of tall buildings consist of a high dimensional feature space of global and local EDPs, which makes it inefficient or even impossible to obtain and use them all in practice (e.g. through inspection or remote sensing). Moreover, the size, complexity and computational expense of tall building structural models makes it unfeasible to generate a large number of physical damage observations. These two issues are likely to result in more features than observations, making some of the aforementioned approaches to linking component-level damage to residual structural capacity unfeasible. For example, it is impossible to use the OLS regression, which requires at least the same number of observations and features to be applicable, and in practice, considerably more observations are needed to achieve a stable model. While some of the techniques used in the prior studies(e.g. [71,72]) are applicable to such dataset, they did not explicitly incorporate feature selection, let alone the interpretation and evaluation of selected features.

This study develops a pattern recognition approach to quantitatively assess the residual structural capacity for tall buildings. The methodology is applied to a 42-story building with RC shear walls and frames, which was developed as part of the Tall Buildings Initiative (TBI) project [52]. Sequential NRHAs are carried out using as-recorded mainshock-aftershock ground motions pairs, where the building is subjected to mainshocks scaled to different intensity levels, followed by an assessment of the residual structural capacity using a set of

aftershock ground motions. Global EDPs including peak story drift ratio (PSDR), residual story drift ratio (RSDR) as well as local or component-level EDPs, such as the maximum frame beam rotation (FBR), frame column rotation (FCR), coupling beam rotation (CBR), concrete compression strain (CCS) and rebar tensile strain (RTS) in shear walls, are recorded for each mainshock ground motion. To effectively reduce the dimensions of the raw features while keeping the ones that are most informative, dispersion-based filtering and LASSO-based feature selection are performed. Support Vector Machines (SVMs) are then used to map the measured responses in a subset of components to the residual structural capacity of the damaged tall building. In addition to guiding post-earthquake inspections and residual structural capacity assessments, the proposed methodology can inform optimal sensor placement in buildings with complex structural systems.

4.2 Overview of Methodology

Fig. 4-1 provides a conceptual illustration of the methodology for evaluating the residual structural capacity of the mainshock-damaged tall building. Beginning with the intact structure in Path A, the structure is subjected to a set of as-recorded aftershock ground motions to simulate the most desirable scenario where a mainshock occurs but the structural damage is inconsequential. This analysis result serves as the baseline for the evaluation and is used to calibrate the performance of the tall building for the mainshock damage scenarios that cause a reduction in the structural capacity. Several tools and models have been developed to assess the sideway collapse safety of frame structures (e.g. [73–75]). Comparatively, much less has been done in this area for shear wall structures. Therefore, a PSDR of 4.5% is used as the collapse prevention (CP) criteria as recommended in TBI [76] and Los Angeles Tall Buildings Structural Design Council (LATBSDC) [53]. Multiple Strip Analyses (MSAs) are conducted using the set of aftershock ground motions and the median first-mode spectral acceleration corresponding to the exceedance of the CP limit state, $\hat{S}a_{CP,INT}$, is adopted as the measure of residual structural capacity.

Sequential response history analyses are performed in Path B, where the intact structure is subjected to a mainshock ground motion scaled to a pre-defined first-mode spectral intensity level, $Sa_{T1,MS}$, followed by MSAs using the set of aftershock ground motions (same ones used in Path A). The distinct response patterns that lead to structural damage under the mainshock ground motion are recorded and the results from the aftershock MSAs are used to estimate the median first-mode spectral acceleration corresponding to exceedance of the CP limit state for

the damaged structure, $\hat{S}a_{CP,DMG}$. A dimensionless residual structural capacity index κ_{CP} is defined as the ratio between $\hat{S}a_{CP,DMG}$ and $\hat{S}a_{CP,INT}$ [71,72].

By combining the results of Paths A and B, this study seeks to map the response patterns of the mainshock-damaged building to its associated safety index κ_{CP}; however, two major challenges rise: 1) the response patterns of tall buildings consist of a high dimensional feature space of global and local EDPs, which makes it inefficient or even impossible to obtain and use them all in practice; 2) the size, complexity and computational expense of tall building structural models makes it unfeasible to generate a large number of physical damage observations. Therefore, dispersion-based filtering and LASSO are employed in Path C to reduce the EDPs recorded during the mainshock to a subset of selected features. For each selected feature, a correlation-based process is conducted to construct a feature group consisting of reserved features which survive the filtering but are excluded by LASSO and could potentially be used as alternatives in the absence of the selected features. In Path D, two SVM models are constructed for each EDP group: one based on the selected features and the other using the features randomly sampled from the corresponding reserved group.

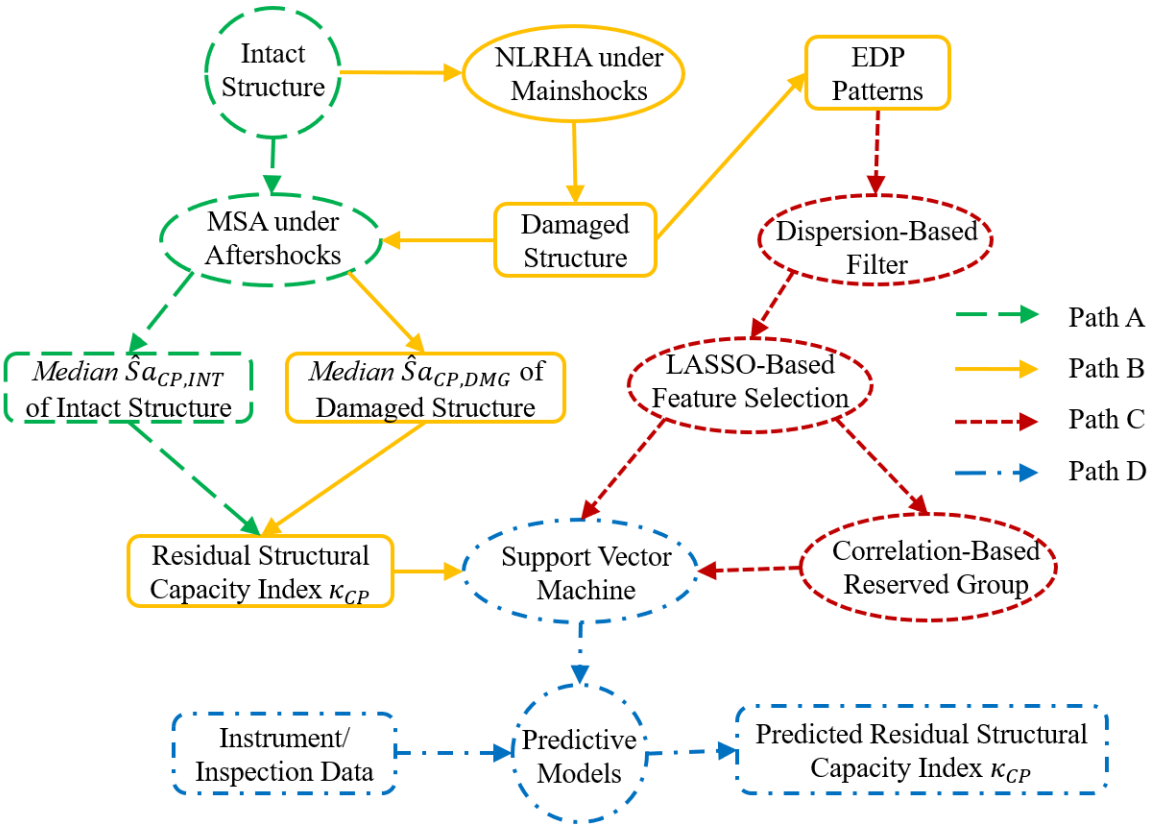

Fig. 4-1. Overview of methodology

4.3 Feature Selection and Grouping of Response Patterns Induced by Mainshock

The 42-story dual system tall building described and modeled in Chapter 3 is used as the archetype for the proposed pattern recognition approach. The set of 34 pairs of mainshock and aftershock ground motions are used for the sequential NRHAs.

4.3.1 Raw Dataset

The 272 observations of κ_{CP} are presented in Fig. **4-2** (a) for the damaged tall building corresponding to 34 mainshock ground motions scaled to 8 different intensity levels ($Sa_{T1,MS}$). Each data point represents the κ_{CP} associated with a single mainshock ground motion and intensity level. A clear descending trend is observed where the median κ_{CP} declines gradually from 1.0 (no mainshock damage) to 0.39 as $Sa_{T1,MS}$ increases. Fig. **4-2** (b) shows an example relationship between κ_{CP} and a single FBR. The κ_{CP} value is clustered around 1.0 when the FBR is less than 0.01 and then declines to as low as almost zero (the building is at the threshold of exceeding the CP limit state after being subjected to the mainshock) as the FBR increases. As the data points are considerably sparse in the region where FBR exceeds 0.01, a relatively low correlation of -0.44 is computed, indicating a weak linear relationship.

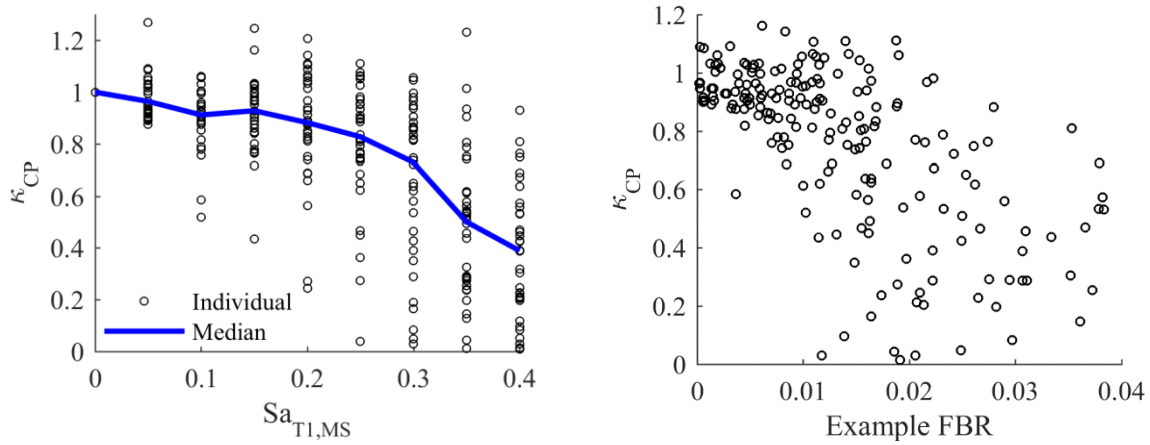

Fig. 4-2. Residual structural capacity index κ_{CP} in the aftershock environment versus (a) the mainshock intensity and (b) an example FBR

Each observation in the raw dataset includes 84 PSDRs and RSDRs (one per story in each direction), 672 FBRs and FCRs, 252 CBRs and 420 CCSs and RTSs. The dimension of this feature space (2604) is much larger than that of the number of observations (272), making it impossible to use some of the more traditional statistical learning methods (e.g. OLS) to map component response patterns to residual structural capacity. Moreover, although all the features

are assumed to be available in the current study, this is unlikely to be the case for post-earthquake inspection or even under remote sensing. As a result, a dispersion filter is combined with LASSO for feature selection, and SVM regression is used to predict residual structural capacity. The following procedure is used to incorporate pattern recognition in the assessment of residual structural capacity: 1) the observations in raw dataset are randomly partitioned into training (75%) and testing (25%) subsets; 2) the models are built based on pattern recognition using only the training subsets; 3) the optimal model selected from the previous step is applied to the testing subset. Residual Mean Squared Error (RMSE) is used as a measure of predictive performance. In Step 2, 10-fold cross-validation is performed, where a training set is randomly partitioned into 10 equal subsets and each time the data from 9 of the subsets are used to train a model while the RMSE from the remaining subset is measured to evaluate the model performance. This process is repeated 3 times to reduce the potential bias induced by data subset partitioning, and the final averaged RMSE is used to select the optimal model.

4.3.2 Dispersion Filter of Features

Our goal is to achieve an accurate assessment of residual structural capacity for the damaged tall building using a small subset of features that are relatively easy to measure and provide robust estimates. This could be addressed in two ways: 1) directly feed the raw data into advanced machine learning algorithms that have built-in feature selection or sparsity properties, which couples the feature search algorithm with the parameter estimation and performs optimization using a single objective function; 2) performing feature selection on the raw data before constructing predictive models. In many cases, the 1st way would be convenient and efficient enough to provide good predictions; however, the selected features could be very sensitive when multicollinearity exists as the model could randomly assign very different coefficients to highly correlated features. Moreover, some of the selected features could be very small (e.g. very small rotations or strains, which are vulnerable to noise) and very difficult to measure in engineering practice. In general, it is well understood that the dispersion in structural responses increases with the demand level and extent of inelastic response. Moreover, for elastic responses, the demand dispersions are generally very small (near zero) and provide very little information about the residual structural capacity of the damaged building. To reduce the number of uninformative features, the raw dataset of mainshock response demands are filtered by a cut-off value for the dispersion within each EDP group (e.g. rotations and strains). These cut-off values are treated as tuning parameters during model training. More specifically, they are obtained by searching within the range of measured

dispersions and selecting the optimal limits that give the best overall model performance. For example, the cut-off value for peak rotation dispersion [Fig. 4-3 (a)] is obtained by searching within the range of 0.005 to 0.030 at increments of 0.0025. Dispersions of 0.015 and 0.003 are used for rotations and strains respectively. The global EDPs (PSDRs and RSDRs) are not filtered because they have a limited number of raw features and relatively large dispersions. Fig. 4-3 shows the dispersion distributions together with corresponding cut-off values for two EDP groups (rotations and strains). For example, a total of 672 (corresponding to the number of beam hinges in the building) FBR dispersions are obtained from their associated 272 observed values [Fig. 4-3 (a)]. From the 672 measured dispersions, 39% fall below 0.015 and 432 remain after the filtering process. The number of post-filtered features in each EDP group is summarized in Table 4-1. Only 2 features are left for CCS, which are very close to the cut-off value. This is likely because most of the compressive strains of the shear wall concrete come from gravity loads with only small changes resulting from the lateral forces induced by mainshocks, indicating CCS provides little information about the overall residual capacity of the damaged building.

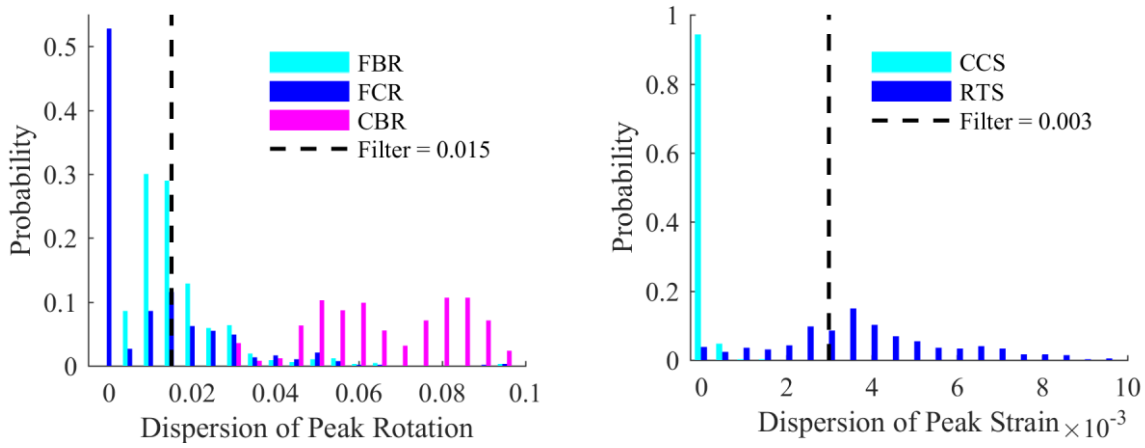

Fig. 4-3. Dispersion filter for (a) rotations and (b) strains

4.3.3 LASSO-based Feature Selection

First introduced by Tibshirani [77] in 1996, LASSO has been used to improve the stability and accuracy of traditional OLS models. This is achieved by penalizing the loss function of OLS regression using the l_1 norm of the feature coefficients, as shown in Equation 4.1. More importantly, it also enables efficient feature selection in the original high dimensional space as it allows the optimal coefficients of a subset of the original feature space to shrinkage to zeros. LASSO can also potentially reduce the multicollinearity in the selected features. For example,

if a subset of features is highly correlated, only the one with the highest dispersion will be selected and the remainder will be removed as they penalize the objective function without providing substantial additional information.

$$J(\boldsymbol{w}, \lambda) = \sum_{i=1}^{N} L(y_i, \hat{y}_i) + \lambda \|\boldsymbol{w}\|_1 \tag{4.1}$$

Where, y_i and $\hat{y}_i$ are observed and predicted responses (residual structural capacity index, κ_{CP} in the current study) respectively; $\boldsymbol{w}$ is the coefficient vector; $L(y_i, \hat{y}_i) = (y_i - \hat{y}_i)^2$ is the loss function of OLS regression where $\hat{y}_i = \boldsymbol{w^T x_i} + w_0$ and $\boldsymbol{x_i}$ is the feature vector representing each EDP group; N is the number of observations (204) in the training dataset; $\lambda \geq 0$ is a regularization term used to penalize the complexity of the model.

For a given value of λ, there is a corresponding number of nonzero coefficients, the effective degrees of freedom of the model, which is denoted as $df(\lambda)$. When $\lambda = 0$, there is no penalty and $df(\lambda)$ is simply the total number of the features in the original dataset and an OLS solution is obtained. As λ increases, $df(\lambda)$ shrinks to zero and the outcome is a naïve model, where the prediction is simply the mean of the observed responses. The approach described in Section 4.3.1 is performed to find the optimal value of $\lambda's$ for the 7 EDP groups (PSDR, RSDR, FBR, FCR, CBR, CCS, RTS) that remain after the filtering process described in Section 4.3.2. The parameter tuning ranges and the performance in terms of the mean RMSEs from 10-fold cross validation are presented in Fig. 4-4. a, while the corresponding $df(\lambda)$'s are summarized in Table 4-1. The optimal λ varies for different EDP groups to balance the amount of information (number of features) extracted from the original high dimension feature space and the complexity of the associated coefficients (overfitting). In general, features having relatively large dispersions and low correlations are desired by LASSO as they not only provide small absolute values but also reduce the size of coefficients. Therefore, LASSO regression is performed on the raw features without any preprocessing (e.g. centering and scaling) to avoid potential selection of features with small values and dispersions that are vulnerable to noise.

Through the LASSO feature selection process, only 11 and 13 features are kept for PSDRs and RSDRs, respectively, giving an 86% reduction for global EDPs. The associated RMSEs of 0.15 (PSDRs and RSDRs) are found for the training dataset, which are considerably higher than the 0.10 obtained from OLS regression using all 84 features in each group. Based on the more reliable measurement using the testing dataset, the PSDRs and RSDRs produce RMSEs

of 0.22 and 0.25, respectively for LASSO regression, while significantly poorer performance corresponding to RMSEs of 0.55 and 0.70, respectively, are obtained from the OLS regression, indicating obvious overfitting when all the features are included. More importantly, an OLS solution is not even possible for component EDPs such as FBR, which has much more features (412) even after the dispersion filter than the total available observations (204) in the training dataset. 38 features are selected for FBR, which comprises 9.2% of the dispersion-filtered features and only 5.6% of the raw feature space, while a relatively low RMSE of 0.30 is achieved. Even better prediction performances with RMSEs of 0.23 and 0.19 are found for the LASSO models constructed using 7.5% and 6.2% of the raw CBR and RTS features. However, when it comes to the FCR and CCS, none of the filtered features are selected, and the algorithm just prefers a naïve model with the prediction using the mean of the responses in the training dataset. It is somewhat self-explanatory for CCS as there are only two features left after the dispersion filter, which might not carry significant information; however, 241 features are still available for FCR after the filter but still none of them are selected. A possible explanation is that the strong-column-weak-beam principle used to design the RC frames makes most of the potential rotation demands or structural damage concentrated in the frame beams. Therefore, the rotation demands in the frame columns do not provide effective information about the overall performance of the tall building.

Fig. 4-4. b shows the comparison of pairwise within-group correlation distributions of the component EDPs before and after the feature selection. Multicollinearity is observed for a portion of FBR and CBR as a considerable amount of correlations are larger than 0.8. The filtered 412 FBR features have a flat correlation distribution with a median around 0.4, while the correlation distribution of the 38 post-LASSO FBRs is skewed to the right with a median less than 0.2, indicating a significant reduction of the multicollinearity within the FBR group. Slightly lower correlations are overserved for CBR, but even higher correlations are found for RTS. This could be due to the fact that most of the features in these two groups have relatively high dispersions and are informative to the overall performance of the tall building, so the algorithm makes a trade-off between the reduction of the number of coefficients and the corresponding multicollinearity among them.

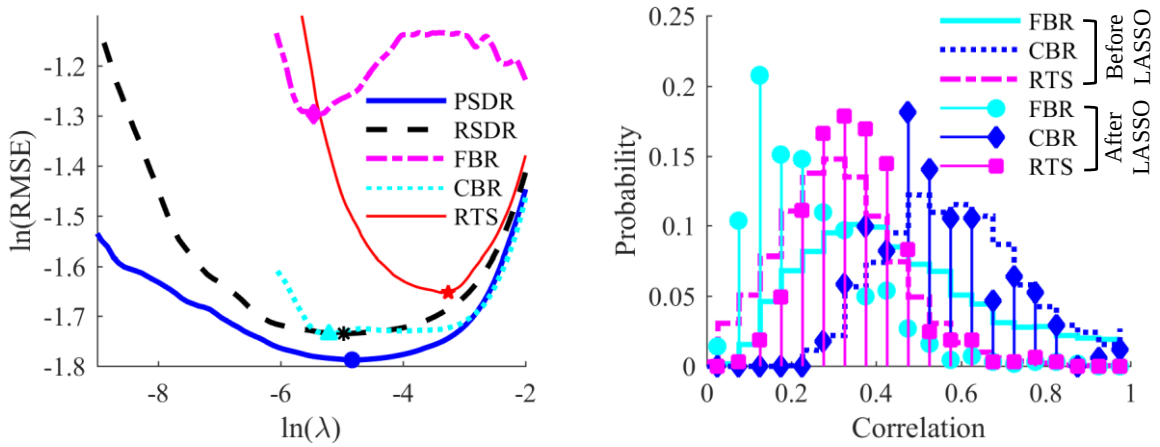

(a) (b)

Fig. 4-4. (a) Parameter tuning of $\boldsymbol{\lambda}$'s in LASSO models for different EDP groups and (b) the comparison of within-group correlation distributions of the component EDPs before and after the LASSO feature selection

Table 4-1. Results of dispersion filtering and LASSO regression

EDP	RMSE		Number of Features		
	Training	Testing	Raw	Post-Filter	Post-LASSO
PSDR	0.15	0.22	84	84	11
RSDR	0.15	0.25	84	84	13
FBR	0.13	0.26	672	412	38
FCR	0.29	0.30	672	241	0
CBR	0.14	0.23	252	252	19
CCS	0.29	0.30	420	2	0
RTS	0.16	0.19	420	307	26

A closer look at the locations and coefficients of the selected features in each EDP group could be useful for optimizing sensor layout. As none of the components in FCR and CCS survives the LASSO selection, only the results of PSDR, RSDR, FBR, CBR, and RTS are discussed. Fig. 4-5 (a) plots the dispersions of the raw features versus their corresponding locations in the building. The circles represent the selected features while the diamond dots denote the features that are excluded. The size of the circles indicates the relative importance of a feature as measured by the absolute value of the corresponding coefficient. In the X direction, PSDRs of the 34th, 10th and 19th stories are selected. The first two are the local maxima's and the third is close to the location where the thickness and concrete strength of the

shear wall change. For similar reasons, two small clusters are observed at the 23rd and 32nd stories.

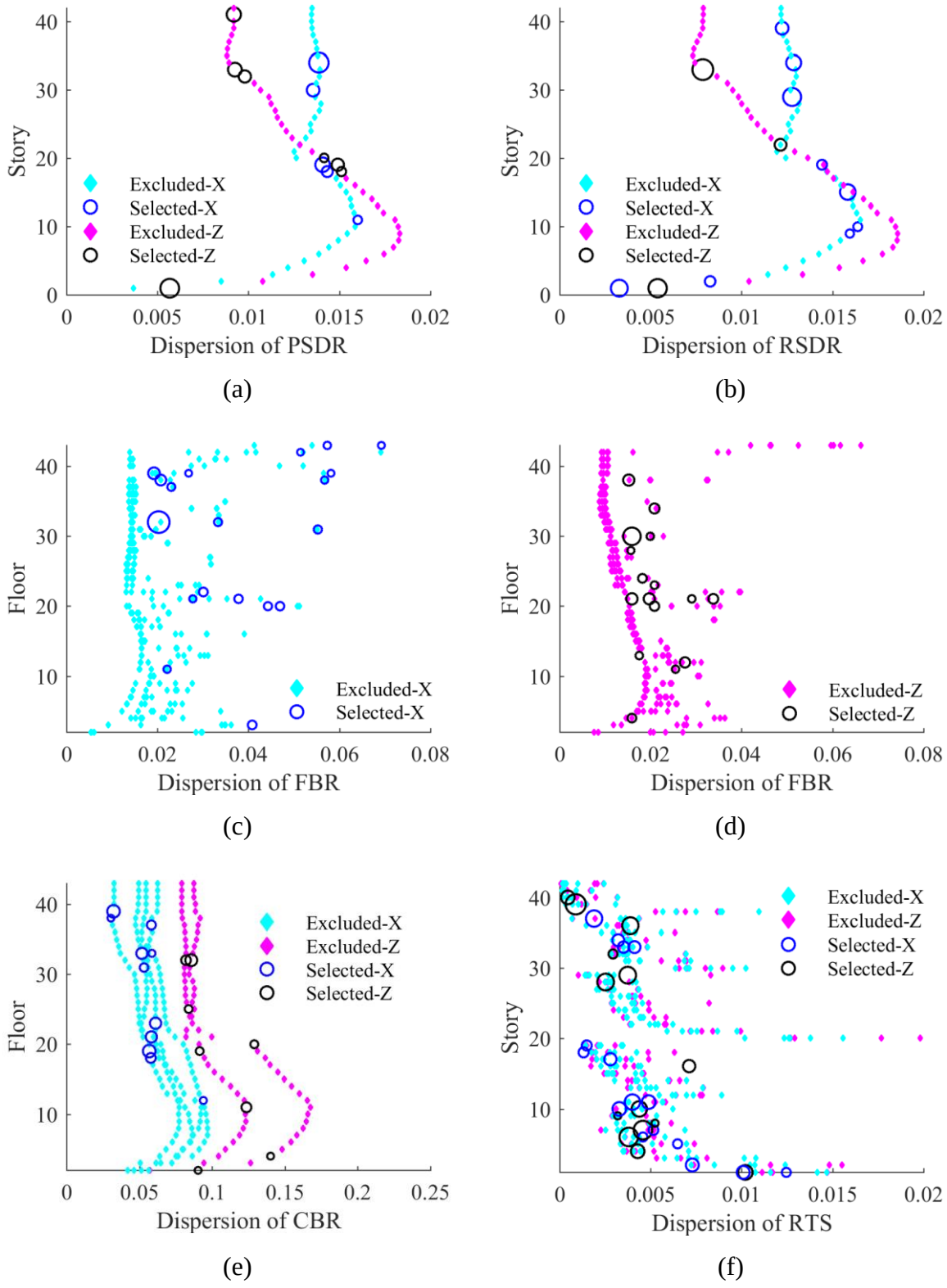

Fig. 4-5. LASSO-based selected and excluded features for (a) PSDR, (b) RSDR, FBR in the (c) X and (d) Z directions, (e) CBR and (f) RTS

A possible explanation for the selection of the PSDRs in the 1st and 41st stories is that they are at the very bottom and top of the building and may have lower correlations with the rest of the data and provides additional information. As shown Fig. 4-5 (b), the selected RSDRs in the two directions are somewhat comparable to the those of PSDRs, especially at the local maxima's and stories where there is a change in the structural design, but they are more evenly distributed. The selected FBRs in the X and Z directions are presented in Fig. 4-5 (c) and (d), respectively. While they are adequately distributed in terms of both the location and the dispersions, some clusters could still be found around the 10th, 20th and 30th floors where there are changes in the structural designs. Some attention is also paid to the FBRs above the 30th floor where the wall width is the smallest and more contribution of the lateral resistance from the frames is potentially needed. Fig. 4-5 (e) and (f) show the patterns for the selected CBRs and RTSs, respectively. Similar patterns with the selected FBRs could be found for both of them except that a considerable number of RTSs located at the first 10 stories are also selected. This is possibly because the demands at these stories are relatively large making the RTSs more sensitive to the overall building performance. Except for the abovementioned patterns, a few FBRs, CBRs, RTSs near the base and roof of the building are also selected. The possible reasons are the discontinuation of the RC frames at the 42nd story to accommodate a penthouse and the hinging that occurs in the walls at the lower stories.

4.4 Pattern Recognition Using Support Vector Machine

4.4.1 Support Vector Machine for Predicting Residual Structural Capacity Using the Selected Features

While LASSO provides effective feature selection from the original high dimensional feature space, the prediction performance is limited as it could only capture the linear part of the relationship between the responses and features. As shown in Fig. 4-2 (b), there is a highly nonlinear and sparse relationship between the residual structural capacity index κ_{CP} and selected features, which requires a more advanced model to ensure good predictive performance.

The SVM technique was first introduced by Vapnik [78] in 1995 to solve binary classification problems and has since been extended to regression problems [79]. The basic idea is to transform the features of the input data into a high dimensional feature space such that they are easier to separate using a hyperplane for classification or are closer to a linear relationship for regression. An l_2 norm is then used to regularize the risk objective function:

$$J(\boldsymbol{w}, \lambda) = \sum_{i=1}^{N} L(y_i, \hat{y}_i) + \lambda \|\boldsymbol{w}\|_2^2 \tag{4.2}$$

Two key modifications, sparse estimation and kernel trick, are employed by SVM to update the risk objective function. A variant of the Huber loss function called ϵ-insensitive loss function is proposed by Vapnik [79], where only the data points lying outside a ϵ-tube is penalized and is defined by:

$$L_\epsilon(y_i, \hat{y}_i) \stackrel{\text{def}}{=} \begin{cases} 0, & |y_i - \hat{y}_i| < \epsilon \\ |y_i - \hat{y}_i| - \epsilon, & otherwise \end{cases} \tag{4.3}$$

Where ϵ is the width of the ϵ-tube used to fit the training dataset.

By substituting $L_\epsilon(y_i, \hat{y}_i)$ into Equation 4.2 and dividing the objective function by $1/2\lambda$, one obtains:

$$J(\boldsymbol{w}, C) = C \sum_{i=1}^{N} L_\epsilon(y_i, \hat{y}_i) + \frac{1}{2} \|\boldsymbol{w}\|_2^2 \tag{4.4}$$

Where $C = 1/2\lambda$ is also a regularization term.

This objective function is convex and unconstrained, but not differentiable. Therefore, slack variables $\xi^+ \geq 0$ and $\xi^- \geq 0$ are then introduced by Equation 4.5 to transform it into the constrained optimization problem given by Equation 4.6.

$$\begin{cases} y_i \leq \hat{y}_i + \epsilon + \xi^+ \\ y_i \geq \hat{y}_i - \epsilon - \xi^- \end{cases} \tag{4.5}$$

$$J(\boldsymbol{w}, C) = C \sum_{i=1}^{N} (\xi^+ + \xi^-) + \frac{1}{2} \|\boldsymbol{w}\|_2^2 \tag{4.6}$$

It is known that the optimal solution of the optimization problem has the form $\hat{\boldsymbol{w}} = \sum_i \alpha_i \boldsymbol{x}_i$ [80]. As a key characteristic of the ϵ-insensitive loss function, the $\boldsymbol{\alpha}$ vector is sparse, and only $\boldsymbol{x}_i$ with $\alpha_i > 0$ are used in the model and are the so-called support vectors. The predicted response given a new data point $\boldsymbol{x}$ could be written as:

$$\hat{y}(x) = w_0 + \sum_i \alpha_i \boldsymbol{x}_i^T \boldsymbol{x} \tag{4.7}$$

The kernel trick is then applied using a radial basis function (RBF):

$$k(\boldsymbol{x}_i, \boldsymbol{x}) = \exp(-\frac{\|\boldsymbol{x}_i - \boldsymbol{x}\|_2^2}{2\sigma^2}) \tag{4.8}$$

Finally, the kernelized solution in Equation 4.9 is achieved by replacing the dot product $\boldsymbol{x}_i^T \boldsymbol{x}$ with the RBF kernel $k(\boldsymbol{x}_i, \boldsymbol{x})$, and optimization algorithms are used to estimate the sparse $\boldsymbol{\alpha}$. Readers are referred to [78] for details of the optimization algorithms.

$$\hat{y}(x) = w_0 + \sum_i \alpha_i k(\boldsymbol{x}_i, \boldsymbol{x}) \tag{4.9}$$

As it is almost impossible to have a simple answer for the best parameters $\sigma's$ and $C's$ using different selected features, SVM regression is performed repeatedly on a turning grid where σ ranges from 2^{-10} to 2^{10} and C ranges from 2^{-15} to 1. Example tuning results for PSDR and FBR are shown in Fig. 4-6. The optimal point with the lowest mean RMSE from the 10-fold cross-validation is found to be $\sigma = 0.02$ and $C = 8$ for the selected PSDRs and be $\sigma = 0.01$ and $C = 1$ for the selected FBRs.

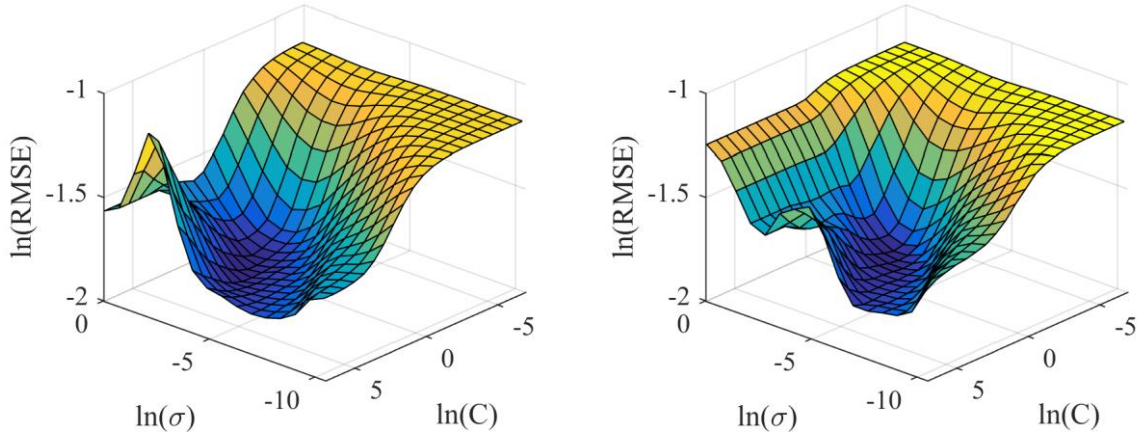

(a) (b)

Fig. 4-6. Tuning results of σ and C using selected futures from (a) PSDR and (b) FBR

The predictive performance (based on RMSE) of six SVM models, which are developed using the selected features, is summarized in Table 4-2. The models vary based on the EDP groups that are considered. Five of the models are based on individual EDP groups (PSDR,

RSDR, FBR, CBR, and RTS) and the sixth model incorporates all groups as predictors. The σ and C parameters used for each model is also shown in Table 4-2. The model based on all EDP groups represents an ideal situation where measurements of both local and global response parameters are available. As expected, this model has the lowest RMSE and therefore performs the best. The models based on individual EDPs represent a more likely scenario where only one type of measurement (e.g. only CBRs) is available. Among these models, the ones based on RSDR and CBR provide the best κ_{CP} predictions with testing set RMSE values that are less than 5% higher than that of the model based on all EDPs. The observed and predicted $\kappa_{CP}{}'s$ are compared in Fig. 4-7 for both the training and testing datasets using the selected CBR features. Despite some local variations, a strong trend along the diagonal (predicted = observed) is observed, which gives an overall indication of satisfactory predictive performance. To benchmark their predictive capability, the RMSEs of the SVM models based on individual EDP groups are compared with those obtained from LASSO models. Using the selected CBRs and RSDRs as the features, the RMSEs from the SVM models are found to be 36% and 30% less than those from the LASSO models, respectively.

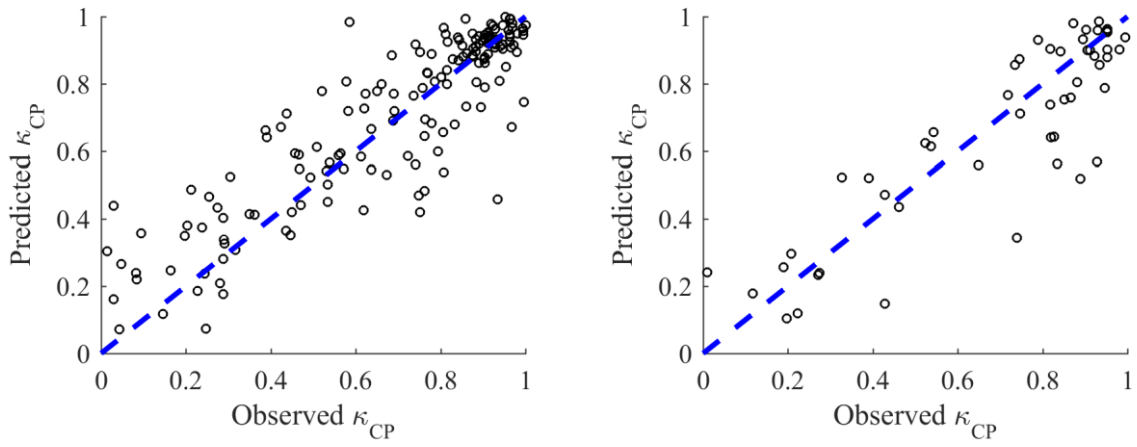

Fig. 4-7. Comparing the observed and predicted κ_{CP}'s in (a) the training and (b) testing dataset using the selected CBR features

4.4.2 Support Vector Machine Using the Randomly Sampled Reserved Features

Although the multicollinearity is not preferred in the feature selection, it is desired between the selected and reserved EDPs as it enables the possibility of using the latter to predict κ_{CP} when the selected features are unavailable. Take the case where the rotation of a coupling beam on the 20th floor level is needed by the model, but only the rotation of an 18th floor level coupling beam is available. If the demands in these two elements are highly correlated, the 18th

floor coupling beam rotation can be used to obtain a satisfactory prediction. For each selected feature, all reserved features that have correlations (with the selected feature) above a certain threshold are grouped. Fig. 4-8 shows 6 example groups of reserved features for FBR and CBR in the X and Z directions with correlation thresholds of 0.95 and 0.90, respectively. It can be seen that the features in the same group tend to be located in the same direction and on adjacent floors, but considerable variation still exist such that no simple rules could be used to define each group. It should be noted that all these features need proper preprocessing before they can be fed to the predictive models, i.e., centering by the means and scaling by the dispersions, which removes the individual scale effect but keeps the linear relationship. This procedure is not performed for PSDRs and RSDRs as they have considerably fewer features and lower correlations between the selected and the reserved features in their groups.

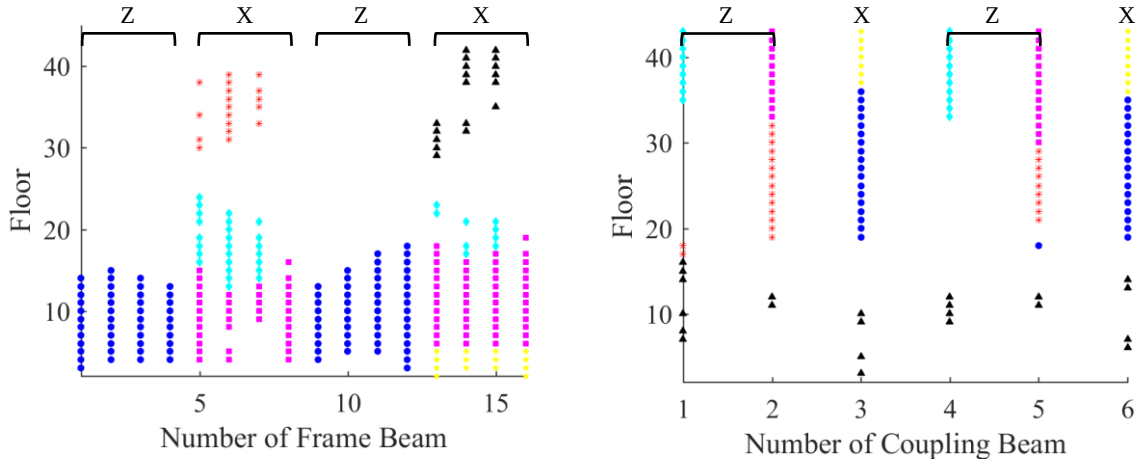

Fig. 4-8. Example groups of reserve features for (a) FBR and (b) CBR

An original observation consists of a residual structural capacity index κ_{CP} and corresponding features, which are categorized based on being filtered (pre-LASSO), reserved and selected. The models constructed earlier utilize only the selected features to predict κ_{CP}; to evaluate the predictive performance using the reserved features, a virtual observation could be simulated by replacing each selected feature with one that is randomly sampled from the corresponding reserved group and keeping the same κ_{CP}. For example, an original observation has 19 selected CBRs, and a virtual observation is generated by replacing each of them with a different CBR in its reserved group. For each original observation, 100 virtual observations are sampled resulting in 20,400 and 6,800 virtual observations for the training and testing datasets, respectively. As the characteristics of all the features are not fundamentally changed, the same tuning parameters $\sigma's$ and $C's$ from Section 4.4.1 are used to train the new SVM models,

whose predictive performances are also shown in Table 4-2. Consistent increases in RMSEs in the testing dataset are found, which is expected as additional randomness is introduced into the model. On the other hand, with a maximum increase of only 9.4% in the RMSE compared to the model constructed using the selected features, the SVM models based on the reserved features still perform significantly better than the LASSO models.

Table 4-2. Predictive performance of κ_{CP} using SVM

EDP	σ	C	RMSE				Change
			Selected Features		Reserved Features		
			Training	Testing	Training	Testing	
PSDR	0.02	8.0	0.14	0.17	NA[1]	NA[1]	NA[1]
RSDR	0.02	1.0	0.12	0.16	NA[1]	NA[1]	NA[1]
FBR	0.01	1.0	0.14	0.17	0.15	0.19	9.4%
CBR	0.06	4.0	0.12	0.16	0.13	0.17	6.3%
RTS	0.01	0.5	0.16	0.19	0.14	0.20	5.1%
All	0.01	1.0	0.11	0.15	0.11	0.18	NA[1]

[1]Reserved features are not used for PSDR and RSDR models

4.4.3 Example Application of Pattern Recognition Approach to Assessing Post-Earthquake Residual Capacity

This section presents an example application of the proposed pattern recognition approach to assessing the residual structural capacity of damaged tall buildings. A hypothetical scenario is considered, where an instrumented tall building is subjected to a sequence of earthquakes, each of which causes increasingly severe damage. The instrumentation layout can be informed by the results from Section 4.3.3 where sensors are only used for the responses parameters identified in the LASSO-based feature selection (e.g. 19 CBRs). Where feasible, an additional set of sensors can be used to capture a small number of reserved features. Once the SVM model is constructed based on these selected and reserved features, response measurements recorded during an earthquake can be used to generate real-time κ_{CP} predictions, which can inform decisions regarding the need for detailed inspections and/or whether the damaged building is safe to reoccupy. It is important to note that, in the case of a non-instrumented building, the EDP-based features used in the current study can be coupled with damage fragility functions and the SVM model constructed using physical damage states as the features. Using this

approach, κ_{CP} predictions can be obtained from observed damage gathered during field inspections.

Fig. 4-9 shows the results from a hypothetical scenario where the building is subjected to a mainshock followed by four aftershocks (denoted AS-1 through AS-4), which are assumed to occur on the 2nd, 4th, 12th and 26th day after the first event. Fig. 4-9 (a) shows that κ_{CP} drops to 0.94 right after a mainshock. Subsequent reductions in κ_{CP} are observed following each aftershock with the value dropping to as low as 0.78. To inform the decision regarding reoccupancy of the damaged building, a minimum κ_{CP} can be defined, whereby the building is deemed unsafe if the value falls below this threshold. Using a minimum κ_{CP} of 0.9 for the hypothetical scenario, the building is deemed safe to occupy right after the mainshock. However, given that the value of κ_{CP} drops to 0.82 following the third aftershock, which occurs on the 12th day, the building is considered unsafe and must be evacuated. Recall that κ_{CP} is the ratio of the median first-mode spectral acceleration associated with the CP limit state for the intact and damaged structure. Using an assumed dispersion of 0.6 [12] and using the predicted κ_{CP} to compute $\hat{S}a_{CP,DMG}$, the pattern recognition model can be used to generate a lognormal time-dependent fragility functions for the CP limit state [Fig. 4-9 (b)]. These fragility functions can be combined with time-dependent aftershock hazard curves to obtained risk-based assessments of the tall building performance in the aftershock environment [70].

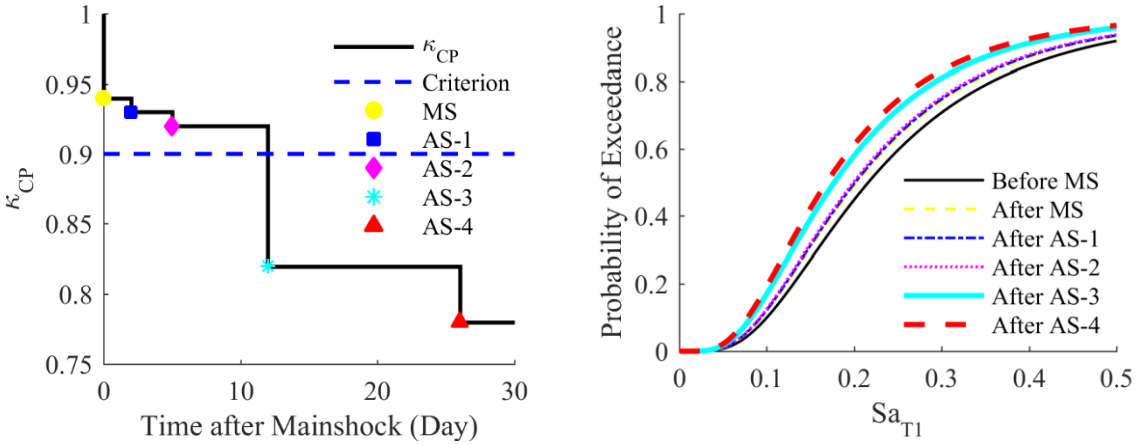

(a) (b)

Fig. 4-9. (a) Predicted κ_{CP} values and (b) CP fragility functions for a hypothetical scenario where the building is subjected to a mainshock followed by four aftershocks

4.5 Conclusion

A pattern recognition approach is developed to quantitatively assess the residual structural capacity of tall buildings. Sequential NRHAs are conducted using as-recorded mainshock-aftershock ground motions pairs, where the building is subjected to various mainshocks scaled to different intensity levels, followed by multiple stripe analyses using a set of aftershock ground motions. The peak story drift ratio (PSDR) corresponding to the collapse prevention (CP) performance criteria (0.045), which is recommended by the Tall Buildings Initiative and Los Angeles Tall Buildings Structural Design Council, is used as the basis of evaluating the performance of the mainshock-damaged building. More specifically, the ratio of the median first-mode spectral acceleration corresponding to the CP performance level for the intact and damaged structure, κ_{CP}, is used as the measure of the residual structural capacity.

A total of 7 EDP groups are examined in detail to understand how they contribute to the residual structural capacity. The global EDPs include PSDR and residual story drift ratios. Maximum frame beam and column rotation (FBR and FCR, respectively), coupling beam rotation (CBR), maximum concrete compression strain (CCS) and rebar tensile strain (RTS) in shear walls, are the local EDPs. Effective feature dimension reduction and informative feature selection are conducted using dispersion-based filtering and Least Absolute Shrinkage and Selection Operator (LASSO) regression. Support Vector Machines (SVMs) are then used to predict κ_{CP}. To train the LASSO and SVM models, 10-fold cross-validations are used to find the optimal model parameters. The features excluded by LASSO are used to generate the reserved dataset, which, through a random simulation process, enables the construction of alternative predictive models.

Pattern recognition models are constructed for the different EDP groups built on a significantly smaller (compared to the raw data) feature space. The global EDPs are observed to be strong indicators of the reduction in structural capacity possibly because they are directly associated with the CP performance metric. However, only the FBR, CBR and RTS give informative predictions and a weak relationship was found between the FCR and CCS and κ_{CP}. For FCR, this is likely due to the strong-column-weak-beam principle used to design the reinforced concrete frames, which seeks to limit plastic rotation demands in the frame columns. As for CCS, it is possible that most of the compressive strains in the shear wall concrete come from gravity loads with only small changes resulting from the lateral forces induced by mainshocks. While it is useful for feature selection, the predictive performance of LASSO is

limited due to the highly nonlinear relationship between κ_{CP} and features. SVM with radial basis function kernel is able to significantly reduce the root mean square errors using the selected features. Moreover, the reserved features can be used when the selected ones are unavailable, within minimal loss in the predictive accuracy.

The proposed methodology provides a rapid link between the structural responses measured during an earthquake to the building performance in subsequent events. This information can be used to optimize the placement of sensors used to measure such responses and guide engineers performing post-earthquake inspections and assessments of residual structural capacity, which can be updated in real-time as structural response data becomes available. Only a single tall building was considered in the development of the methodology. To generalize its feasibility, additional evaluations are needed using other tall buildings with different structural configurations and lateral force resisting systems. Finally, the analyses used to generate the response patterns only incorporated record-to-record uncertainty. Prior studies have shown that modeling uncertainty can affect both the dispersion and median values of limit-state-based performance metrics. Therefore, for implementation purposes, the effect of modeling uncertainty should be incorporated in future work.

CHAPTER 5: Seismic Risk Assessment of Tall Buildings Considering Mainshock and Aftershock Hazard

This chapter is adopted from the following study:

Zhang, Y., Burton, H. V., Shokrabadi, M. & Wallace J. W. (2019). Seismic risk assessment of a 42-story reinforced concrete dual-system building considering mainshock and aftershock hazard. ASCE Journal of Structural Engineering (accepted for publication).

5.1 Introduction and background

High-rise buildings are often an integral part of the residential, commercial and cultural development of urban centers. Several tall buildings, which are either newly-completed or under construction, can be found in high-seismicity hazard regions on the west coast of the United States in cities such as Seattle, Portland, San Francisco, Los Angeles, and San Diego. Aside from the direct financial losses resulting from structural and non-structural damage, significant downtime in high-rise buildings following a major earthquake could have a rippling negative effect on the local economy. Seismic risk assessment is one of the techniques that can be used to assess these concerns and can be used to inform decision-making in both pre- and post-earthquake environment.

Advancements in seismic hazard analysis, nonlinear response simulation, and performance-based engineering are enabling better assessment of the risk associated with tall buildings from earthquakes and other hazards. Organizations such as the Los Angeles Tall Buildings Structural Design Council (LATBSDC) and the Pacific Earthquake Engineering Research (PEER) Center have developed tools and guidelines that permit rigorous design and assessment procedures.

Several high-rise building cases were developed and analyzed as part of the PEER Tall Buildings Initiative (TBI) project [81], including a 42-story concrete core wall residential building, a 42-story concrete dual core wall/frame system and a 40-story office building with buckling restrained braces (BRB) [52,82–84]. These building cases have since been the subject of numerous studies. Jayaram et al. [85] implemented the ATC-58 guidelines to develop vulnerability functions for a set of tall buildings (including two of the TBI buildings) relating ground motion spectral intensities to direct economic losses. Jones and Zareian [86] evaluated

the seismic performance of three variations of the TBI 40-story BRB building. Tipler et al. [87] evaluated the seismic performance of several variants of the TBI, 42-story core wall building using financial losses and functional downtime as the performance metrics of interest and also examined the effect of incorporating damped outriggers and base isolation as alternative schemes intended to enhance seismic performance.

The aforementioned studies only considered mainshock hazard in the seismic performance assessment of tall buildings; however, major mainshock seismic events are known to be followed by a cluster of aftershock events in a relatively short time period. Despite being smaller in magnitude than their preceding mainshock, aftershocks could be particularly impactful because of their high rate of occurrence and the reduction in the structural capacity mainshock-damaged buildings. Documented losses from several earthquakes (e.g., 2011 Christchurch, 2011 Tohoku, and 2016 Central Italy earthquakes) have highlighted the role of aftershocks in exacerbating the financial and human implications of major mainshock events [9,10,88].

In recent years, several studies have attempted to characterize the impact of aftershocks on the seismic performance of buildings. Jeon et al. [67] proposed a framework for developing aftershock damage fragility curves for reinforced concrete frames. The application of the framework to a series of 4- to 12-story non-ductile frames showed that the aftershock vulnerability of buildings is greatly affected by the level of mainshock-damage. A study by Burton and Sharma [89] on the post-mainshock seismic performance of reinforced concrete frame buildings with infills found that infill strut axial deformations and story drift demand metrics are the most informative indicators of the aftershock residual collapse capacity. Burton et al. [71] also explored the accuracy and stability of different statistical models for estimating aftershock collapse vulnerability of buildings using predictors including mainshock intensity, structural response, and physical damage indicators. Yeo and Cornell [68] proposed a framework for estimating earthquake-induced monetary losses under mainshock-aftershock sequences. While these and other similar studies on mainshock-aftershock seismic performance assessment [32,90,91] have advanced our understanding of the additional seismic risk to buildings posed by aftershocks, none-to-date have focused on high-rise buildings, which are typically designed using alternative (or performance-based) procedures. Zhang and Burton [92] used a pattern recognition approach to assess the residual structural capacity of an earthquake-damaged tall building, however, the effect of time-dependent aftershock hazard was not considered.

The present study examines the seismic performance of a 42-story reinforced concrete dual system building considering mainshock and aftershock hazards. A Markov process is implemented, which accounts for the uncertainty in the seismic hazard (mainshock and aftershock) and the time-dependent building structural damage following the mainshock. The elevated seismic activity that follows the mainshock is captured using the aftershock probabilistic seismic hazard analysis (APSHA) methodology developed by Yeo and Cornell [62]. The time-dependent probability of exceeding various response demand limits over a pre-defined period considering only mainshock and mainshock-aftershock hazard is compared. The risk-based consistency (or lack thereof) of the limit state acceptance criteria for EDPs suggested by TBI [81] and LATBSDC [53] is also examined. It is worth noting that, while there are more recent versions of these guidelines (e.g. TBI 2017 and LATBSDC 2017), there are have been no major changes to the modeling and acceptance criteria that would influence the key findings of the current study.

5.2 Seismic Demand and Vulnerability Assessment

The 42-story dual system tall building described and modeled in Chapter 3 is used as the archetype in the assessment. The set of 34 pairs of mainshock and aftershock ground motions are used for the sequential NRHAs.

5.2.1 Nonlinear Response History Analyses

The design procedures provided by TBI Guidelines [76] and LATBSDC [93] use both local (component-level) and global EDPs to evaluate collapse prevention performance at the MCE hazard level. Table 5-1 summarizes the deformation-based EDPs and their demand limits associated with the collapse prevention performance level. Note that these limits are used as indicators of potential collapse and are not explicitly associated with the collapse state [94]. In other words, explicit collapse simulations are not within the scope of the current study. To characterize the structural response and evaluate the performance of the mainshock-damaged 42-story reinforced concrete dual system structure in the aftershock environment, NRHAs are performed using mainshock-aftershock sequential ground motions. A forty-five second free-vibration period is added following the mainshock record to ensure that the structure comes to rest (i.e. all nodes are at zero velocity) before it is subjected to the aftershock record. Prior to this, the performance of the intact or undamaged building is assessed by subjecting the structural model to only the mainshock ground motions scaled to MCE hazard level ($Sa_{T1} = 0.20g$). The principal horizontal directions of the building are referred to as the X- and Z-

Direction [Fig. 3-1 (b)]. Fig. 5-1 shows the peak story drift ratio (PSDR) profile in the two horizontal directions, including the response to the individual ground motions as well as the mean, median, 16th and 84th percentile response. Two analyses are conducted for each mainshock ground motion pair by switching the orthogonal direction of each record. The median PSDR in X-Direction is 1.1% at the 32nd story and the dispersion, which is described in terms of the log-standard deviation is 0.42. The median PSDR in Z-Direction is 1.0% at the 29th story and the lognormal dispersion is 0.43. The mean PSDR along height is 1.4% at the 29th story and 1.2% at the 10th story for X- and Z-Directions respectively, which satisfies the design requirements of the TBI report [84].

Table 5-1. Collapse prevention performance criteria defined based on EDP limits [52,76,93]

Description	Notation	Acceptance Criteria
Peak Story Drift Ratio	PSDR	3.0%
Residual Story Drift Ratio	RSDR	1.0%
Frame Beam Rotation	FBR	4.5%
Coupling Beam Rotation	CBR	6.0%
Concrete Compression Strain	CCS	0.015
Rebar Tension Strain	RTS	0.050

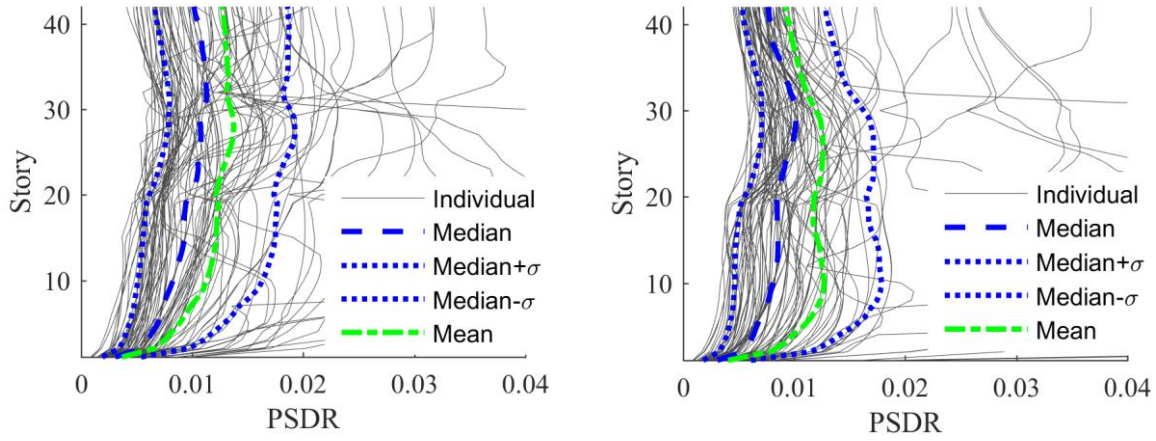

Fig. 5-1. PSDR profile in the X- and Z-Direction under the mainshock only

A comparative assessment of the effect of mainshock-damage on the amplification of the peak demand levels corresponding to the response parameters in Table 5-1 is presented. To

conduct this assessment, sequential NRHAs are performed with each mainshock ground motion scaled to the MCE hazard level, which is followed by incremental dynamic analyses (IDAs) with the aftershock ground motions scaled with Sa_{T1} ranging from $0.025g$ to $0.25g$ at increments of $0.025g$. Since the intent of the analyses performed in this section is not to quantify aftershock risk (this is done in the section of Aftershock Seismic Risk), the mean rate of exceedance for each of the aftershock intensities is not considered. The goal here is to evaluate whether there are systematic differences in the extent to which the demand levels for the various types of EDPs (e.g. PSDR versus CBR) are affected by mainshock damage. The MCE hazard level is chosen because it is expected to induce levels of damage that would highlight these differences. The range of aftershock intensities is selected to be sufficient for constructing the limit state fragility curves. The orthogonal directions of the ground motions are switched for each pair, which means that a single sequence corresponds to 4 analyses, which captures the uncertainty in the directions of mainshock-aftershock ground motions relative to the principal axes of the building.

Fig. 5-2 compares the median peak values of the 6 EDPs for the intact structure analyzed using MCE level shaking (mainshock-only analyses) and the mainshock-damaged structure (mainshock ground motion scaled to MCE) subjected to an aftershock ground motion scaled to $0.15g$ (mainshock-aftershock analyses). In each plot, X-MS and Z-MS denote the responses in the X and Z directions from the mainshock-only analyses and X-MSAS and Z-MSAS are from the mainshock-aftershock analyses. Fig. 5-2 (a) shows that the median PSDR in X-Direction increases from 1.1% in mainshock-only analyses to 1.2% under aftershock while the Z-Direction PSDRs are similar for mainshock-only and mainshock-aftershock. It is worth recalling that the intensity of the mainshock ($0.25g$) is higher than that of the aftershock ($0.15g$). Significant amplifications are observed in Fig. 5-2 (b) for residual story drift ratios (RSDR), with a 70% increase in the X-Direction at median demand level (0.17% to 0.29%) and 44% in the Z-Direction (0.34% to 0.49 %). This observation suggests that, in the aftershock environment, RSDR demands are more sensitive to mainshock-damage compared to PSDR. As shown in Fig. 5-2 (c), the mainshock-aftershock median of the maximum hinge rotations in the moment frame beams is 30% higher in Z-Direction but only 9% higher in X-Direction. In Fig. 5-2 (d), the median of the maximum coupling beam hinge rotations increases from 3.4% to 4.5% and from 5.1% to 7.1% in the X- and Z-Direction, respectively, representing 33% and 39% increases. Fig. 5-2 (d)-(e) compares the median peak compression and tension strains at wall boundaries. The mainshock-aftershock compressive strains are 16% and 47% higher in X-

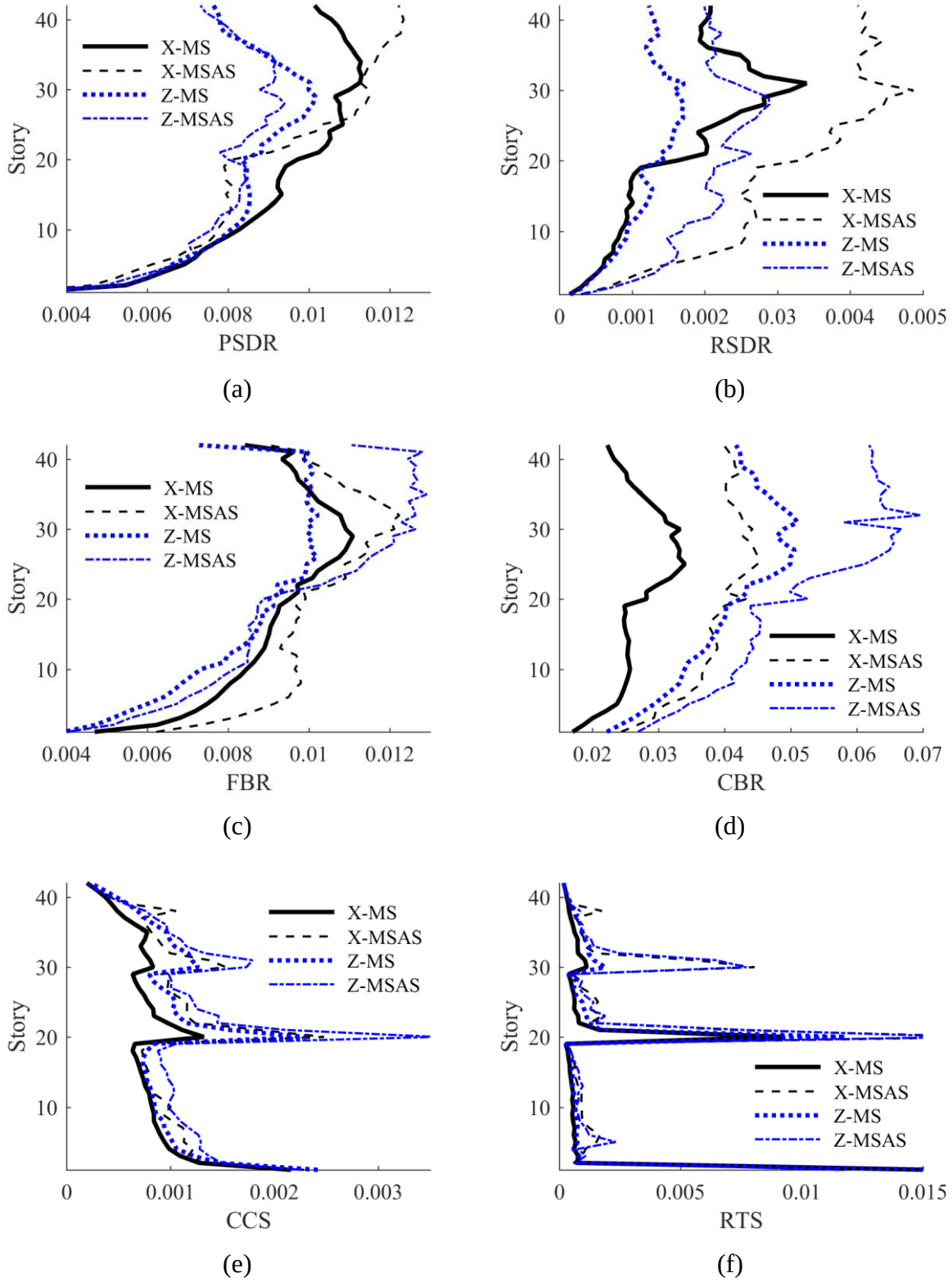

Fig. 5-2. Median profile of maximum (a) story drift ratio, (b) residual story drift ratio, (c) beam hinge rotation, (d) coupling beam hinge rotation, (e) wall compression strain and (f) wall tension strain.

and Z-Direction; while the corresponding tension strains increase by 16% and 7%, respectively. The strain increases are mainly concentrated at the 20th and 30th story where the design of wall sections and reinforcement are reduced.

Fig. 5-3 (a) shows a plot of the ratio of the median maximum response demands between the mainshock-only and mainshock-aftershock analyses (demand ratio) versus the ratio between the aftershock and mainshock intensity (intensity ratio), where the maximum of the X- and Z-Direction responses are used to compute the intensity ratio. It can be observed that, when the structure is damaged by MCE level mainshock, aftershock ground motions with only 75% intensity of that mainshock (intensity ratio of 0.75) can generate response demands which are higher than the mainshock (demand ratio greater than 1.0). The extent of this response amplification is different for different EDPs. For example, Fig. 5-3 (b) shows a plot of the intensity ratio that corresponds to a demand ratio of 1.0 for all six EDPs. RSDR is observed to have the lowest intensity ratio (0.31) and is, therefore, the most sensitive mainshock-damage. The CBR and CCS also have lower intensity ratios (0.35 and 0.36, respectively), while the FBR, PSDR, and RTS are considerably less sensitive.

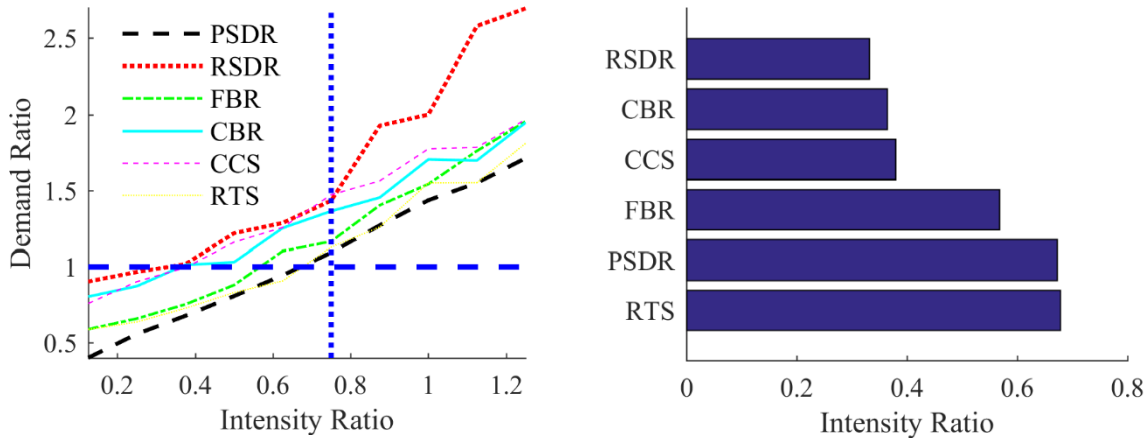

(a) (b)

Fig. 5-3. (a) Ratio of the response demands between the mainshock-only and mainshock-aftershock analyses (demand ratio) versus the ratio between the aftershock and mainshock intensity (intensity ratio) and (b) intensity ratio corresponding to a demand ratio of 1.0 for all six EDPs

5.2.2 Limit State Fragility Functions

Fragility functions linking the probability of exceeding the individual response demand limits in Table 5-1 and the ground motion intensity measure under mainshock-only and mainshock-aftershock analyses are presented in Fig. 5-4. The mainshock-aftershock fragility

functions all correspond to MCE level mainshock damage. Fragility functions showing the probability of not achieving the collapse prevention (CP) performance level (as defined by TBI), which corresponds to the case where any of the six EDP limits are exceeded, are also shown in Fig. 5-4. Comparing the mainshock-only [Fig. 5-4 (a)] and mainshock-aftershock fragility functions [Fig. 5-4 (b)], lower median intensity corresponding to each EDP limit state and higher levels of dispersion are observed for the latter. For example, the median capacity for FBRs for the mainshock-only fragility is $0.36g$ and the log-standard deviation is 0.40, while the same parameters for the mainshock-aftershock case are $0.17g$ and 1.74, respectively. Fig. 5-4 shows that the collapse prevention performance level is controlled by the CBR. In other words, the limit state for this EDP has the highest exceedance probability across all mainshock and aftershock intensity levels and the fragility function overlaps with that of the collapse prevention performance level. Recall from Table 5-1 that, in accordance with TBI and the LATBSDC design guidelines, a 6% coupling beam rotation limit is used for the collapse prevention performance level. However, prior experimental investigations on the cyclic response of coupling beams showed that residual strength (10% to 20% of the capping strength) is maintained at rotation demands as high as 10% [95]. RSDR limit state has the next highest exceedance probability and peak compression strain has the lowest. For the mainshock-only case, PSDR has higher exceedance probabilities than FBR and RTS. However, the reverse is true for the mainshock-aftershock case; the FBR and RTS states have higher exceedance probabilities compared to PSDR, which again highlights the differences in the extent to which mainshock damage is reflected in the different EDPs.

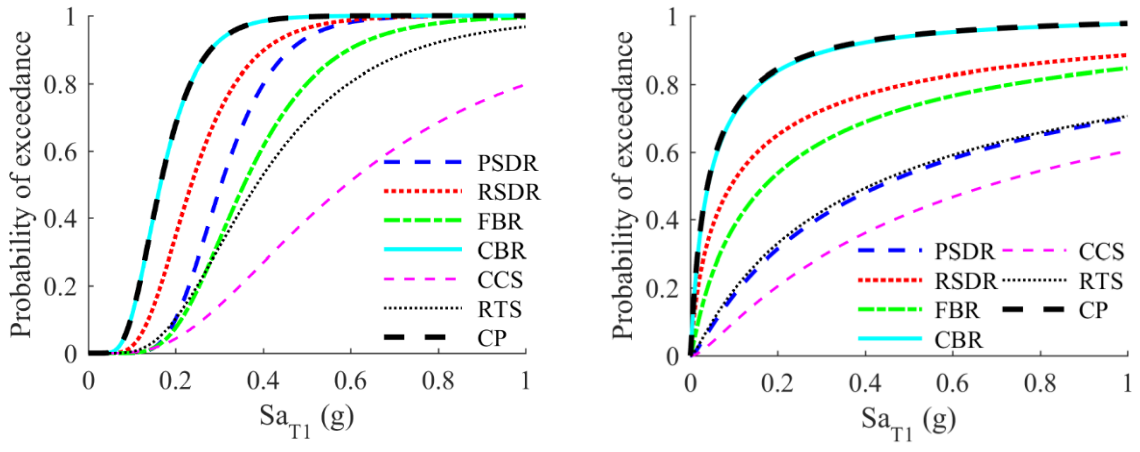

Fig. 5-4. Fragility functions of the 6 EDPs for (a) mainshock-only and (b) mainshock-aftershock cases, where the mainshock intensity is set at the MCE-level

5.3 Seismic Risk Assessment

Two categories of risk assessment are conducted in the aftershock environment. The first, which is described as aftershock risk, computes the probability of exceeding some limit state conditioned on a known mainshock event and immediate post-mainshock damage state of the structure. The second considers the uncertainty in the mainshock and aftershock hazard and is referred to as mainshock-aftershock risk. For both categories of assessments, a Markov process model is used to quantify the probability that the structure incrementally transitions through different states of damage at any point in time following a mainshock earthquake (Yeo and Cornell 2005).

5.3.1 PSDR-Based Building Damage States and Fragility Functions

PSDR is often used as an indicator of the reduction in the lateral force resisting capacity of damaged buildings under sequential ground motions [21,32,33,68,69,72] and is adopted in this study as a proxy for the building-level damage states. Limit states of primary interest are the EDP-based criteria defined in Table 5-1. The incremental PSDR-based damage states are only used to consider the uncertainty in building-level damage after being subjected to mainshock or aftershock ground motions. Alternatively, an energy-based measure of global damage [96] could be used; however, given the large number of components in the structure under consideration, this would significantly increase the computational expense of the proposed assessments as it requires recording the full cyclic hysteric response of all components and integration to compute the energy dissipation. In addition to the intact or undamaged structure, eleven damage states corresponding to PSDRs ranging from 0.25% to 5.25% at 0.5% increments are used for the Markov chain model described in the section of Aftershock Seismic Risk. In the following sections, the center point or median value of the associated increment interval denotes each PSDR-based damage state. For example, the 1st damage state has an interval from 0.25% to 0.75%, which is denoted by PSDR = 0.5%.

For both the mainshock and mainshock-aftershock risk assessment, fragility functions describing the probability of transitioning from the intact structure to a higher state of damage, conditioned on the mainshock intensity, are needed. These fragility functions are generated using the results from multiple stripe analyses (MSA) with the ground motion intensity (Sa_{T1}) ranging from $0.05g$ to $0.6g$ at increments of $0.025g$. The 34 mainshock ground motions described earlier are used, where the geometric mean Sa_{T1} of the two horizontal components of each record is used for scaling. For each Sa_{T1} increment, the building is subjected to the two

possible direction combinations of the two components of each ground motion, which results in a total of 1564 NRHAs. The lognormal cumulative distribution function (CDF) shown in Equation 5.3 is adopted for fitting the fragility function of each PSDR-based damage state.

$$f_k^{MS}(im) = \Phi\left(\frac{\ln(im) - \ln(\theta_k^{MS})}{\beta_k^{MS}}\right) \tag{5.3}$$

where; $f_k^{MS}(im)$ is the probability of exceeding the k^{th} PSDR-based damage state ($k = 1, \dots, 11$) when subjected to a mainshock ground motion with $IM = im$; Φ is the standard normal CDF; θ_k^{MS} and β_k^{MS} are the median and dispersion of the k^{th} PSDR-based damage fragility function. The maximum likelihood method [97–99] is used for parameter estimation and the median θ_k^{MS} increases monotonically with k since all the lower damage states must be exceeded before the building transitions into a higher state. The lognormal dispersion β_k^{MS}varies from 0.29 to 0.41, and is generally higher for the more severe damage states.

In the aftershock environment, the fragility functions capture the probability of transitioning from any PSDR-based damage state (including the intact state) to another that is more severe. The aftershock fragility functions are developed using sequential response history analyses where the mainshock ground motions are iteratively scaled to induce the desired PSDR corresponding to each damage state. The mainshock NRHA is followed by a series of MSAs using the aftershock ground motions to obtain the fragility functions for states that are higher than the known conditioning damage state. Ten Sa_{T1} increments ranging from $0.06g$ to $0.6g$ are used to balance computational expense with the accuracy of the maximum likelihood estimation. All 4 possible direction combinations of the two components from mainshock-aftershock ground motion pairs are considered, resulting in a total of 14,960 sequential NRHAs. The analyses were conducted using 500 cores on the UCLA Hoffman2 Cluster for 4 weeks. Equation 5.4 defines conditional fragility functions.

$$f_{i,j}^{AS}(im) = \Phi\left(\frac{\ln(im) - \ln(\theta_{i,j}^{AS})}{\beta_{i,j}^{AS}}\right) \tag{5.4}$$

where $i \leq j$; $i = 0, \dots, 10$ and $j = 1, \dots, 11$; $f_{i,j}^{AS}(im)$ is the probability that the building with an existing damage state i will exceed damage state j when subjected to an aftershock ground motion with $IM = im$; $\theta_{i,j}^{AS}$ and $\beta_{i,j}^{AS}$ are the median and dispersion of a conditional fragility function between damage states i and j. Repair activities in the aftershock

environment are not considered; therefore $f_{i,j}^{AS}(im) = 0$ when $i > j$ as transitions from higher to lower damage states are not possible. The lognormal dispersion β_k^{AS}varies from 0.37 to 1.39 and is generally higher for the more severe damage states. β_k^{AS} is generally larger than β_k^{MS} as more uncertainties are expected when aftershocks are incorporated.

Fig. 5-5 presents a sample comparison of fragility curves showing the probability of exceeding different PDSR levels for the intact building and the damage state corresponding to median PSDR = 1.5% (PSDR interval from 1.25% to 1.75%). Fragility functions for PSDRs ranging from 1.25% to 5.25% are shown for the intact case [Fig. 5-5 (a)] and 2.25% to 5.25% for the immediate post-mainshock PSDR = 1.5% case [Fig. 5-5 (b)]. Considerably lower medians and higher dispersions are observed for the latter, confirming that the conditional fragility functions capture the degradation of the structural capacity in the mainshock-damaged building.

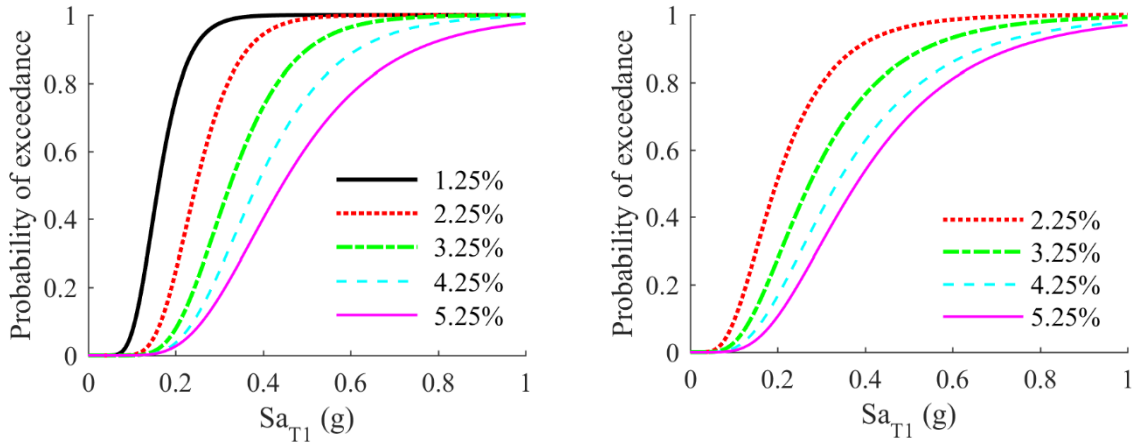

Fig. 5-5. Aftershock fragility functions for (a) the intact state and (b) the PSDR = 1.5% damage state

5.3.2 Conditional Probability of Exceeding EDP-based Limit States

In the next two sections, the seismic risk is assessed in terms of the time-dependent probability of exceeding the structural response demand limits set by the TBI and LATBSDC (shown in Table 5-1) considering both mainshock and aftershock hazards. To compute these exceedance probabilities, the relationship between the EDP limits shown in Table 5-1 and the PSDR-based damage states is established. For each EDP limit, the probability of exceedance conditioned on the PSDR-based damage state is obtained by fitting the empirical data with a lognormal distribution according to Equation 5.5.

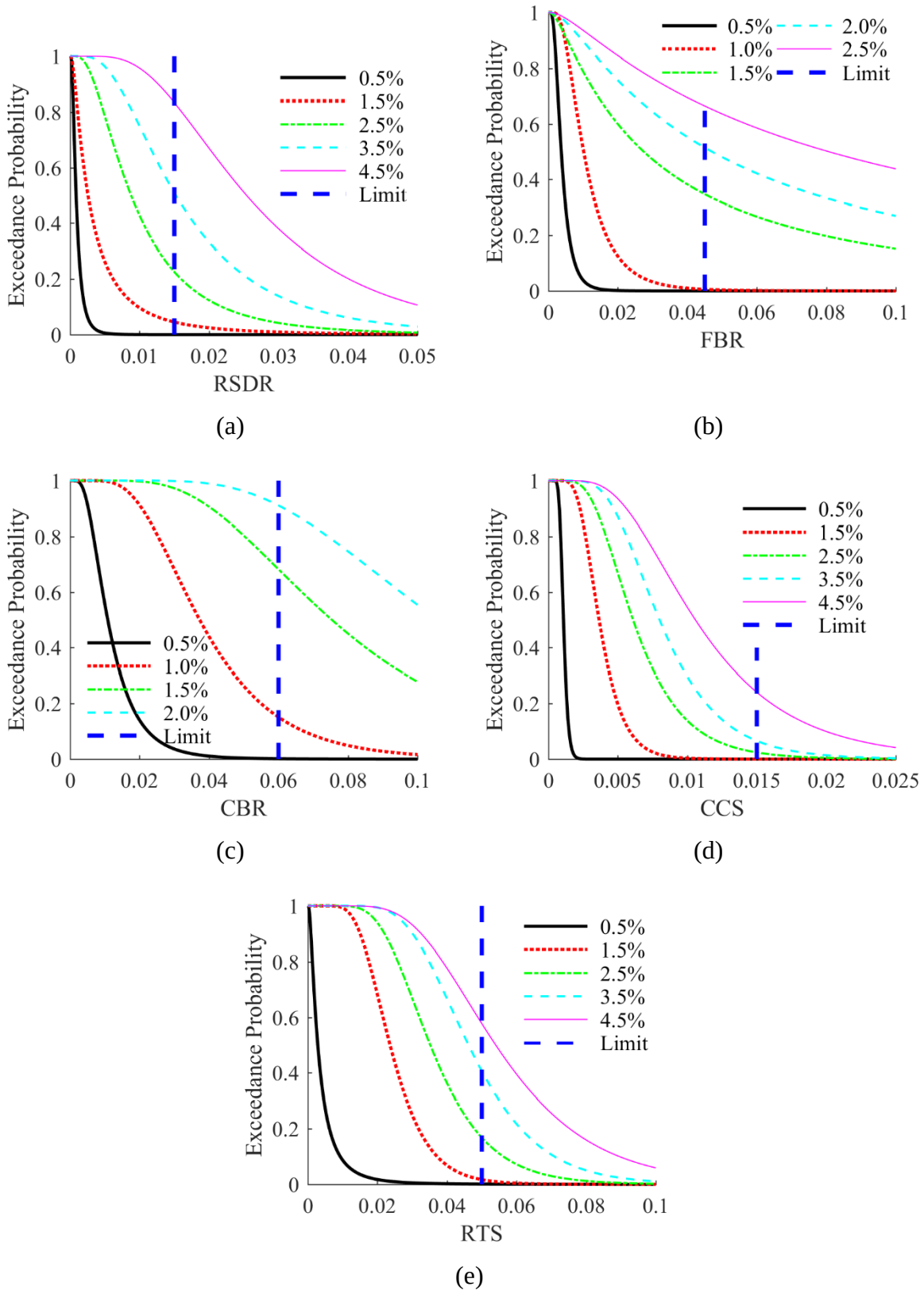

Fig. 5-6. Conditional probability of exceeding EDP levels for (a) RSDR, (b) FBR, (c) CBR, (d) CCS and (e) RTS given each PSDR-based damage state

$$u_k^g(edp) = 1 - \Phi\left(\frac{\ln(edp) - \ln(\theta_k^g)}{\beta_k^g}\right) \tag{5.5}$$

where g is the identification number of the EDP, $g = 1, \ldots, 6$; $u_k^g(edp)$ is the conditional exceedance probability that EDP-g > edp given a damage state of PSDR-k; θ_k^g and β_k^g are the median and dispersion of the conditional lognormal distribution.

Except for PSDR (since it is used as the conditioning EDP), the conditional probability of exceedance for each EDP is shown in Fig. 5-6 alongside its associated limit. Fig. 5-6 (a) indicates that the exceedance probability for RSDR increases significantly with each increment of PSDR damage state. Conditioned on the same PSDR-based damage state, the relative increase in the exceedance probabilities for CBRs are much larger than those of FBRs. For example, when the damage state corresponds to PSDR = 2.0% or higher, the probability of exceeding the CBR limit is more than 90%. For the same PSDR damage state, the probability of exceeding the FBR limit is only 51%. The exceedance probabilities of CCS and RTS are generally very low compared to the other EDPs. In fact, the probability of exceeding the CCS limit is essentially zero for PSDR damage levels of 1.5% or less. The RTS limit has low to moderate exceedance probabilities up to PSDR = 2.5% but exceeds 50% at PSDR = 4.5%. These observations are consistent with the design objectives of the building, as most of the inelastic deformations are intended to take place at CBRs and FBRs.

5.3.3 Aftershock Seismic Risk

For the case where a mainshock has occurred and the damage state of the building is known, the state-conditioned fragility function is combined with the exceedance probabilities and the aftershock hazard described in the previous sections to assess risk. As noted earlier, the aftershock hazard is time-dependent and decreases rapidly following the occurrence of the mainshock. Thus, a non-homogeneous Markov process is constructed to simulate the time-dependent probability of exceeding the EDP limits shown in Table 5-1.

The time period is discretized into small increments such that the probability of more than one aftershock is negligible [62]. Equation 5.6 shows the 12-by-12 upper triangular Markov transition matrix for one increment and a single fault. Each entry describes the probability of transitioning between any two damage states, which is computed using Equations 5.7 and 5.8. Given an initial probability distribution, the time-dependent probability distribution in the post-

mainshock environment is computed using Equation 5.9 by cumulatively multiplying the Markov transition matrices.

$$M_n^s = \begin{pmatrix} \pi_{n,0,0}^s & \cdots & \pi_{n,0,11}^s \\ \vdots & \ddots & \vdots \\ 0 & \cdots & \pi_{n,11,11}^s \end{pmatrix} \tag{5.6}$$

$$\pi_{n,i,j}^s = \lambda_{n,i,j}^s e^{-(\lambda_{n,i,j}^s)} \tag{5.7}$$

$$\lambda_{n,i,j}^s = \int_0^{+\infty} (f_{i,j}^{AS}(im) - f_{i,j+1}^{AS}(im)) d\lambda_{IM,n,s}^{AS}(im) \tag{5.8}$$

$$\left(p_{n,0}^{Ns} \; p_{n,1}^{Ns} \; \cdots \; p_{n,11}^{Ns}\right) = \left(p_{n,0}^{0} \; p_{n,1}^{0} \; \cdots \; p_{n,11}^{0}\right) \prod_{s=1}^{N_s} M_n^s \tag{5.9}$$

where s denotes the identification number of the time increment, N_s is the total number of increments in the time period considered, M_n^s is the Markov transition matrix at time increment s for Fault n; $\pi_{n,i,j}^s$ is the transition probability from PSDR-i to PSDR-j at Increment s for Fault n, $i, j = 0, \ldots, 11$; Δt is the uniform time increment; $\lambda_{n,i,j}^s$ is the mean rate of the building transitioning from PSDR-i to PSDR-j within time increment s based on aftershock generated at Fault n; $\lambda_{IM,n,s}^{AS}(im)$ is the mean rate of the seismic events having $IM > im$ generated by fault n within time increment s, and it is computed by replacing the t_0 and t_1 with t_{s-1} and t_s in Equation 5.2 at increment s and substituting the associated $\nu_n^{AS}[t_{s-1}, t_s]$ into Equation 5.1; $p_{n,k}^0$ and $p_{n,k}^{Ns}$ denote the probability of PSDR-k at the start and end of the time period only considering the influence of Fault n.

Examples of transition matrices for the PSDR-based damage states corresponding to (a) immediately following the mainshock and (b) 30 days after the mainshock considering a single fault are shown in Table 5-2 and

Table 5-3, respectively, which are obtained using a time-increment of 0.01 day. It is observed that the diagonal entries are always significantly larger than the off-diagonal ones in the same row, indicating low probabilities of transitioning to higher damage states in the aftershock environment. The off-diagonal entries drop significantly from M_n^1 to M_n^{3000} while the diagonal entries approach 1.0, which reflects the time-dependent decrease in aftershock hazard. However, the probabilities in both matrices are the stand-alone transition probabilities

(i.e., the history and cumulative effects of such transitions from M_n^1 up to M_n^{3000} are not shown), which are computed for a very short time interval (0.01 day).

Table 5-2. Markov transition matrix M_n^1 (10^{-3})

DS	0	1	2	3	4	5	6	7	8	9	10	11
0	891	95.6	10.4	1.54	0.556	0.172	0.065	0.028	0.044	0.018	0.019	0.074
1		979	16.0	2.85	1.120	0.372	0.147	0.069	0.100	0.040	0.045	0.189
2			997	1.57	0.584	0.181	0.104	0.083	0.036	0.029	0.010	0.073
3				997	2.040	0.559	0.339	0.154	0.102	0.110	0.013	0.146
4					997	1.82	0.631	0.134	0.452	0.171	0.062	0.142
5						997	1.940	0.797	0.255	0.087	0.046	0.105
6							992	4.970	1.520	0.379	0.351	0.527
7								992	3.350	0.945	1.360	1.960
8									992	2.630	2.190	3.630
9										988	3.930	8.100
10											993	7.050
11												1000

Table 5-3. Markov transition matrix M_n^{3000} (10^{-6})

DS	0	1	2	3	4	5	6	7	8	9	10	11
0	10^6	105	11.5	1.70	0.613	0.189	0.071	0.031	0.048	0.019	0.021	0.082
1		10^6	17.7	3.14	1.240	0.409	0.162	0.076	0.110	0.044	0.050	0.208
2			10^6	1.73	0.644	0.200	0.115	0.091	0.040	0.032	0.011	0.080
3				10^6	2.250	0.616	0.374	0.170	0.112	0.121	0.015	0.161
4					10^6	2.010	0.695	0.148	0.498	0.189	0.068	0.156
5						10^6	2.140	0.878	0.281	0.096	0.051	0.115
6							10^6	5.480	1.670	0.418	0.387	0.580
7								10^6	3.690	1.040	1.500	2.160
8									10^6	2.890	2.410	4.000
9										10^6	4.330	8.920
10											10^6	7.760
11												10^6

By setting $p_{n,1}^0 = 1$ (or $p_{n,2}^0 = 1$) and the rest zeros in Equation 5.9, the time-dependent probability of exceeding the six limit states in the aftershock environment is assessed given that a mainshock has occurred and the building is damaged with median PSDR of 0.5% (or 1.0%). Fig. 5-7 (a) shows how these exceedance probabilities vary in the 30-day period after the mainshock given that the building is damaged with median PSDR of 0.5%. It is observed that, with the exception of CBR, the probability of exceedance rapidly increases for all the limit states in the first 3-day period due to the high aftershock hazard right after the mainshock. This is followed by a much slower and gradual increase towards the end of the 30-day period as the hazard decreases. For example, the probability of exceeding FBR limit state rises from 0.6% to 3.0% in the first 3 days and is approximately 4.0% after 30 days. A higher initial value but the moderate increase is observed for the probability of exceeding CBR limit, which starts at 15%, and increases to 18% in 3 days, and reaches 20% after 30 days. The time-dependent probabilities of exceedance for the building damaged to PSDR = 1.0% in the mainshock are depicted in Fig. 5-7 (b). Significantly higher probabilities throughout the 30-day period are found for CBR, FBR, RSDR, and RTS. For example, the probability of exceeding FBR limit state is approximately 36% for the full 30 days during for which aftershock hazard is considered. For both Fig. 5-7 (a) and (b), the probabilities tend to stabilize at the end of the 30-day period, indicating that this time period is sufficient to incorporate the aftershock hazard and is adopted in the next section for mainshock-aftershock seismic risk assessment.

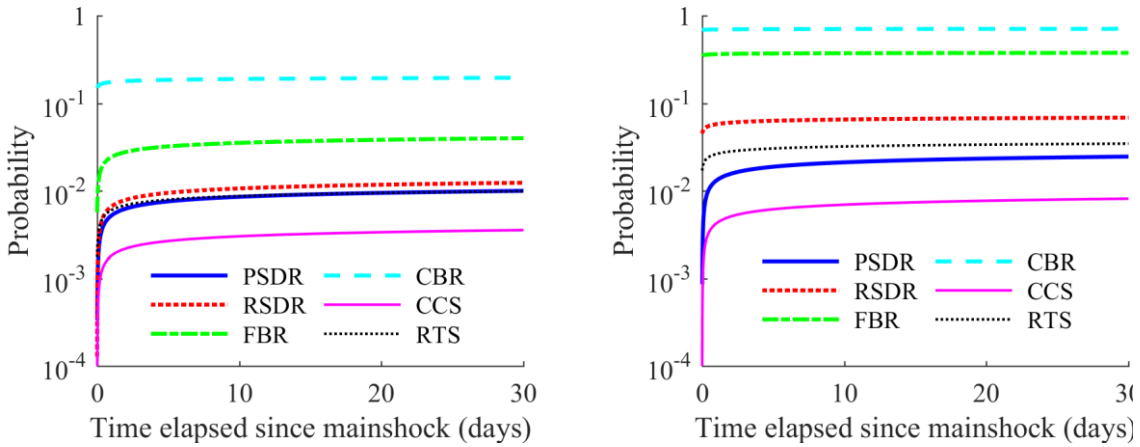

Fig. 5-7. The time-dependent probabilities of exceeding the EDP limit in the aftershock environment given that the building is damaged under mainshock with median PSDR of (a) 0.5% and (b) 1.0%.

5.3.4 Mainshock-Aftershock Seismic Risk

For a single fault, the mean annual rate of occurrence for each PSDR-based damage state is computed in Equation 5.10 by combining the fragility function of each damage state with the mainshock hazard at the building site from this fault only. The total mean annual rate for mainshock is obtained in Equation 5.11 by summing the contributions from all the considered faults, which are reported in Table 5-4.

$$\lambda_{n,k}^{MS} = \int_0^{+\infty} (f_k^{MS}(im) - f_{k+1}^{MS}(im)) d\lambda_{IM,n}^{MS}(im) \tag{5.10}$$

$$\lambda_k^{MS} = \sum_{n=1}^{N_F} \lambda_{n,k}^{MS} \tag{5.11}$$

where $\lambda_{n,k}^{MS}$ is the mean annual rate of the building being in PSDR-k due to the potential seismic event at Fault n, while λ_k^{MS} is for all faults, $k = 1, \dots, 11$; $N_f = 49$ is the number of total faults considered in this study.

The seismic risk from both the mainshock and aftershock hazard is obtained by incorporating the potential transitions to higher damage states under aftershock into the mean annual rate of occurrence of all the PSDR-based damage states under mainshock. Since the mainshock-aftershock hazards are pairwise at each fault, the above process needs to be performed fault by fault before being aggregated to obtain the total mainshock-aftershock mean annual rate as presented in Equations 5.12 and 5.13.

$$\left(\lambda_{n,0}^{MSAS} \ \lambda_{n,1}^{MSAS} \ \cdots \ \lambda_{n,11}^{MSAS}\right) = \left(\lambda_{n,0}^{MS} \ \lambda_{n,1}^{MS} \ \cdots \ \lambda_{n,11}^{MS}\right) \prod_{s=1}^{N_s} M_n^s \tag{5.12}$$

$$\lambda_k^{MSAS} = \sum_{n=1}^{N_F} \lambda_{n,k}^{MSAS} \tag{5.13}$$

where $\lambda_{n,k}^{MSAS}$ is the mean annual rate of occurrence of PSDR-k considering both the mainshock and aftershock hazards from Fault n; λ_k^{MSAS} is the total mainshock-aftershock mean annual rate of occurrence of PSDR-k.

Table 5-4 compares the mean annual rate of occurrence for different PSDR-based damage states when mainshock only and mainshock-aftershock hazard is considered. The mainshock-aftershock mean annual rate of PSDR = 0.5% and PSDR = 1.0% is roughly twice and 23% less

than the mainshock-only values, respectively. The lower mean annual rate for PSDR = 1.0% is fully explained by the significant increase in the mean annual rates of all the other higher damage states. In other words, the rate of transitioning from intact and PSDR = 0.5% to PSDR = 1.0% is less than the rate corresponding to transitions from PSDR = 1.0% to the higher damage states.

Table 5-4. Mean annual rates of occurrence for PSDR-based damage states (unit: 10^{-5})

DS	1	2	3	4	5	6	7	8	9	10	11
λ_k^{MS}	4429	1198	19.16	4.82	2.28	1.18	0.452	0.505	0.181	0.128	0.902
λ_k^{MSAS}	8980	924.4	157.8	61.0	21.7	9.31	4.942	5.620	2.493	2.469	11.42

With the exception of PSDR, the total probability theorem is used to compute the mean annual rate of exceeding the EDP limits in Table 5-1, as shown in Equation 5.14. Since PSDR is the conditioning EDP, and the mean annual rate of exceeding values ranging from 0.25% to 5.25% with an increment of 0.5% is obtained from Equation 5.15.

$$\gamma_g^{MS}(edp) = \sum_{k=1}^{N_{LS}} \lambda_k^{MS} \, u_k^g(edp) \tag{5.14}$$

$$\gamma_{1,k}^{MS} = \sum_{k}^{N_{LS}} \lambda_k^{MS} \tag{5.15}$$

where $\gamma_g^{MS}(edp)$ is the mean annual rate of exceedance that EDP-$g > edp$ considering only the mainshock hazard, $g = 2, \ldots, 7$; $\gamma_{1,k}^{MS}$ is the mean annual rate corresponding to PSDR being larger than the lower value in the range defining the increment; $N_{LS} = 10$ is the total number of damage states; $\gamma_g^{MS}(edp)$, $\gamma_{1,k}^{MS}$ and λ_k^{MS} could be substituted with $\gamma_g^{MSAS}(edp)$, $\gamma_{1,k}^{MSAS}$ and λ_k^{MSAS} for the mainshock-aftershock case.

The mean annual rate of exceedance is transformed into the probability of exceedance in 50 years using exponential distribution to quantify the risk as the latter is more common in engineering practice. Fig. 5-8 shows the probability of exceedance in 50 years for all limit states. For the same exceedance probability, significantly larger demands are found for all the EDPs when aftershock hazard is considered and this difference increases with demand level. For example, in Fig. 5-8 (a), for exceedance probability of 10%, 5% and 2% in 50 years, the

PSDR demands are 0.7%, 0.9% and 1.2% when only considering mainshock. These values increase to 1.4%, 1.8% and 2.5% when aftershock hazard is included. Similar relationships are presented in Fig. 5-8 (b) for RSDR. In Fig. 5-8 (c), CBR has a higher probability of exceedance than FBR for any rotation demand, indicating that, as expected, the coupling beams are the most susceptible to structural damage. Fig. 5-8 (d) shows that the demand and probability of exceedance for RTS are consistently larger than those for CCS at wall boundaries.

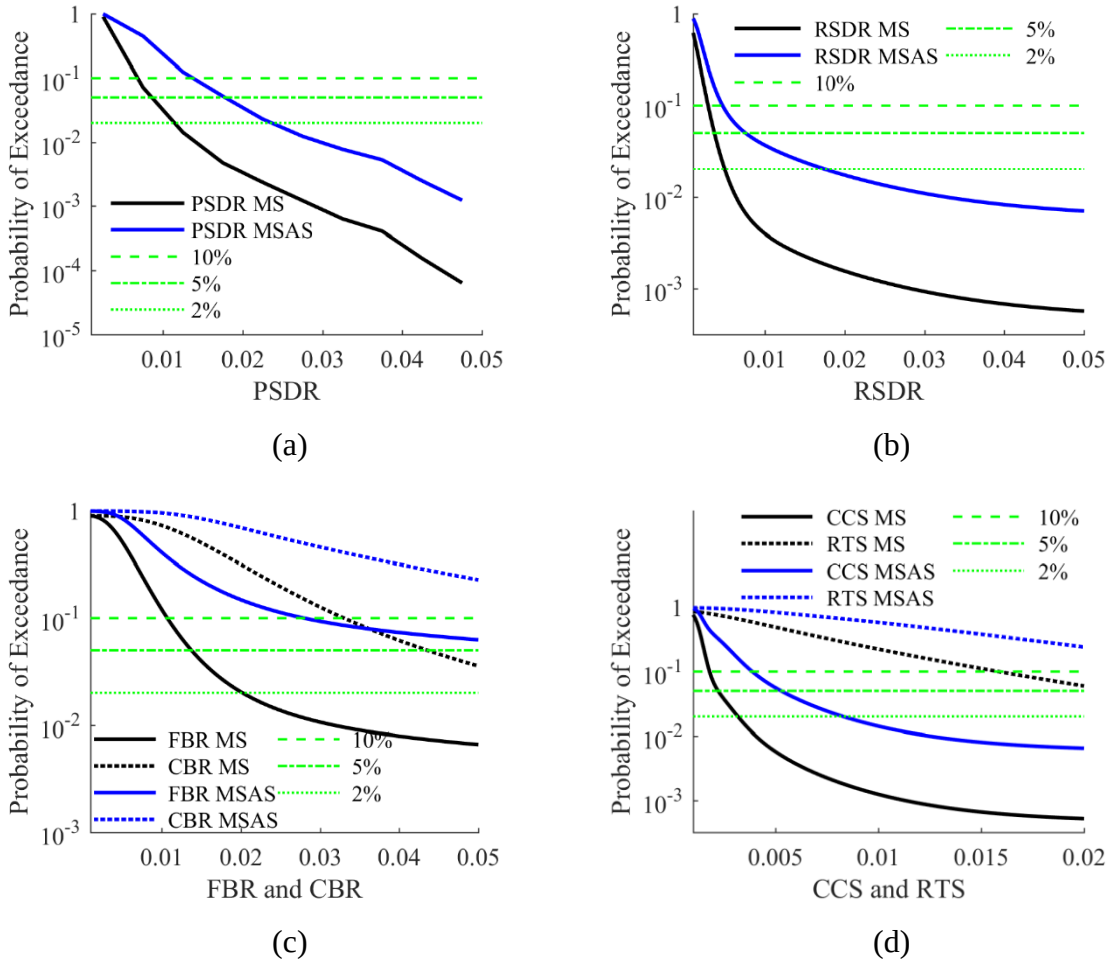

Fig. 5-8. 50-year exceedance probabilities for (a) PSDR, (b) RSDR, (c) FBR, and CBR and (d) CCS and RTS

The EDP value corresponding to three different risk levels are reported in Table 5-5. Recall that the limits presented in Table 5-1 are based on median or maximum (depending on the number of ground motions used) value and are intended to represent the collapse prevention limit state. Modern design codes target a risk threshold of 1% collapse probability in 50 years [3,100]. However, it should be noted that the demands used for the collapse prevention performance level are typically less than what is used for collapse. For example, a 10% PSDR is often associated with a collapse for low- to moderate-height moment frames [75,101,102],

whereas, a 3% PSDR is used for collapse prevention performance. Given these considerations, a risk level of 2% in 50 years is assumed acceptable for the collapse prevention limit state. From Table 5-5, it can be observed that, with the exception of CBR, all other EDP values corresponding to the 2% in 50-year risk level are less than the collapse prevention limits set by TBI and LATBSDC when only mainshock hazard is considered. The 2% in 50-year CBR is only 5% higher than the collapse prevention demand limit. On the other hand, when both mainshock and aftershock hazard are considered, the RSDR, FBR, and CBR are significantly larger than the collapse prevention limits. This result is consistent with earlier findings (e.g. Fig. 5-3 and Fig. 5-4), which show that these demand parameters are most affected by the inclusion of aftershock hazard. Lower response demand limits are expected for higher performance levels such as life safety and immediate occupancy, which are associated with lower risk levels and higher 50-year exceedance probabilities. While further work is needed to calibrate these higher performance levels, response demands for two additional risk levels with 50-year exceedance probabilities of 5% and 10%, are shown in Table 5-5. Note that, for performance levels related to post-earthquake functionality, non-structural damage, which is beyond the scope of the current study, must be considered.

Table 5-5. EDP values corresponding to three risk levels

EDP	10% in 50 years		5% in 50 years		2% in 50 years	
	MS	MSAS	MS	MSAS	MS	MSAS
PSDR	0.7%	1.4%	0.9%	1.8%	1.2%	2.5%
RSDR	0.3%	0.5%	0.4%	0.8%	0.5%	1.7%
FBR	1.1%	2.8%	1.4%	6.9%	2.0%	>10%
CBR	3.2%	8.1%	4.3%	>10%	6.3%	>10%
CCS	0.002	0.004	0.002	0.005	0.003	0.008
RTS	0.016	0.030	0.021	0.037	0.030	0.050

Shown in Table 5-6 are the 50-year exceedance probabilities implied by the collapse prevention EDP limits when only mainshock and mainshock-aftershock seismic hazard is considered. It can be observed that, when only mainshock hazard is considered, most of the 50-year probabilities of exceedance are less than 2%. However, these 50-year exceedance probabilities vary widely across EDPs, ranging from 0.07% for CCS to 2.3% for CBR, which represents a 30-fold difference. For the mainshock-aftershock hazard case, the exceedance

probabilities of RSDR, FBR and CBR are much greater than 2%. The variation in exceedance probabilities is also significant for the mainshock-aftershock case with the highest and lowest values differing by a factor of about 20. Given that all the EDP limits are associated with the collapse prevention performance level, the large differences in 50-year exceedance probabilities reveal a high level of risk inconsistency in the acceptance criteria.

Table 5-6. Implied Probability of exceedance given the acceptance criteria of EDPs (Unit: %)

Hazard	PSDR	RSDR	FBR	CBR	CCS	RTS	Risk
MS	0.17	0.40	0.72	2.30	0.07	0.37	2.00
MSAS	1.67	3.68	6.74	16.92	0.79	1.20	

It is noted that the 6% limit on CBR is associated with strength loss, whereas laboratory tests have shown that modest residual strength (e.g., 10 to 20% of peak strength) is typically maintained for CBRs exceeding 10% [95,103]; therefore, exceeding the 6% CBR limit is unlikely to produce system collapse. If component (e.g., CB) strength loss is modeled, the TBI and LATBSDC documents limit the loss of story strength to 20%. This limit state is not considered in this study, as the limit states given in TBI and LATBSDC are intentionally set to preclude any significant component or system strength loss because of uncertainties associated with modeling components and component level and system level interactions, as well as modeling simplifications employed to reduce computational effort. None-the-less, use of these limits states provides a basis for comparing mainshock and mainshock-aftershock seismic risk in this study.

5.4 Conclusions

The mainshock, aftershock and mainshock-aftershock seismic risk of a typical high-rise building with reinforced concrete core walls and a perimeter special moment frame is assessed. Two key sources of increased risk of exceeding the collapse prevention performance level (relative to mainshock-only assessments) are incorporated: the reduction in the deformation capacity of the lateral force resisting system due to mainshock damage and the elevated seismic hazard in aftershock environment during a short period after the mainshock. Conventional (mainshock) and aftershock probabilistic seismic hazard analysis are conducted for the site that is the basis of the building design, considering hazard contributions from 49 faults. 34 pairs of as-recorded mainshock-aftershock ground motion sequences are selected.

NRHAs are conducted using mainshock ground motions scaled to the MCE hazard level followed by multiple stripe analysis using the aftershock records. The objective of this part of the study was to evaluate and compare the extent to which the response measured by six demand parameters are amplified. These EDPs, which form the basis of the performance-based design criteria for tall buildings, include peak story drifts ratios (PSDRs), residual story drift ratios (RSDR), coupling beam rotation (CBR), frame beam rotation (FBR), concrete compressive strain (CCS) and rebar tensile strain (RTS). The demand amplification was assessed by computing the aftershock intensity, which is normalized by that of the mainshock, at which the demand associated with the maximum considered earthquake (MCE) level mainshock hazard is exceeded (denoted as intensity ratio). RSDR, CBR, and CCS were observed to have the smallest intensity ratios – the ratio between the aftershock and mainshock intensity at the point where the demand under the former is the same as the latter –, which implies that these EDPs are reflected the most in mainshock damage and aftershock performance. Fragility functions describing the probability of exceeding the EDP limits set by the Pacific Earthquake Engineering Research Center Tall Buildings Initiative (TBI) and Los Angeles Tall Building Structural Design Council (LATBSDC) were developed from the results of the mainshock analyses as well as the aftershock analyses conditioned on MCE level mainshock ground motions. For both cases, CBR controlled the collapse prevention performance level implied by the EDP limits set by TBI and LATBSDC.

Two types of risk assessments were conducted. The first, which is referred to as aftershock risk, considers the case where the mainshock has occurred and the immediate post-mainshock building-level damage state is known. A non-homogenous Markov process model is used to couple the probability of exceeding the limit for each of the six response parameters, which is conditioned on a known PSDR-based building-level damage state, with the time-dependent aftershock hazard, to produce exceedance probabilities at different time points over a 30-day period following the mainshock. Except for CBR, a sharp increase and plateauing of the exceedance probability for the EDP limits were observed in the first 3 days when conditioned on immediate post-mainshock PSDR = 0.5%. For the same immediate post-mainshock PSDR, the probability of exceeding the CBR limit is consistently high over the 30-day period. This type of assessment could inform the timing, cost and duration of repairs after a mainshock has occurred. For example, the results from this study showed that delaying repairs for approximately the first week after the mainshock could avoid having to perform redundant repair work caused by subsequent aftershock damage.

The second risk assessment category, which is described as mainshock-aftershock risk, accounts for the uncertainty in the intensity and damage caused by both the mainshock and aftershock, and is compared with the mainshock-only risk. A Markov process model is also used for this assessment and the probability of exceeding each EDP limit over the 50-year life of the building is computed. When a 2% probability of exceedance in 50 years is used as the risk threshold for life safety, most of the associated response demands (except for CBR) are within the collapse prevention performance criteria when only mainshock hazard is considered. However, when the mainshock-aftershock hazard is considered, the demand levels for RSDR, FBR and CBR are much higher than the those corresponding to collapse prevention performance. Even though the limits set by TBI and LATBSDC are targeted towards collapse prevention performance, the implied 50-year exceedance probabilities were found to be non-uniform across the various EDPs for the mainshock only and mainshock-aftershock case, differing by a factor of 30 in the extreme case. This finding highlights the need to develop risk-consistent respond demand limits when the acceptance criteria are targeted towards a single performance level.

CHAPTER 6: Optimal Decision-Making for Tall Buildings in the Aftershock Environment

6.1 Introduction and Background

Ensuring a certain level of life safety during a major earthquake has been the priority for the modern seismic design codes and guidelines. By integrating this primary requirement with the direct and indirect financial losses caused by seismic events into a probabilistic framework, the Performance-Based Earthquake Engineering (PBEE) [15] induces a more robust alternative performance assessment and design approach which have been widely used in recent engineering practices. However, the PBEE only considers major seismic events with long return periods, i.e. mainshocks, which in many cases could be followed by a series of subsequent earthquakes referred as aftershocks with relatively lower magnitudes and shorter periods, but higher occurrence rates. The additional fatality and financial losses caused by aftershocks have drawn attention in such sequential seismic events. For example, several buildings that survived the mainshock of magnitude 7.4 in the 1999 Kocaeli earthquake collapsed during an aftershock with magnitude 5.9 that occurred one month later, killing seven people and injuring more than two hundred [104]. In the 2010 Darfield earthquake, the mainshock with a magnitude of 7.1 is followed by two major aftershocks with magnitudes of 6.2 and 6.0 respectively, which alone lead to 185 more fatalities and add up to over 30 billion dollars financial losses [10]. Similar situations are also found in 1999 Chi-Chi, 2008 Wenchuan, 2011 Tohoku and 2016 Central Italy earthquakes [88,105].

Special attention has been paid to evaluating the structural vulnerability or residual capacity of mainshock-damaged buildings in the aftershock environment. The increased demands of certain critical EDPs (for example, Peak Story Drift Ratio (PSDRs), Residual Story Drift Ratio (RSDRs) and plastic hinge rotations of beams and columns) have been quantified in many researches for different types of structures, such as steel moment frames [91,106,107], Reinforced Concrete (RC) moment frames with [89,108] or without infills [30,109–112] and tall buildings with shear walls [92]. More recently, researches are carried out to build the statistical relationship between the EDPs and component damages under mainshocks and the performance of the damaged building in the aftershocks. Univariate analysis for individual EDP [32] and triggering damage quantile [33] are performed to evaluate their effects on the reduction in the collapse capacity. To address the potential interaction among different EDPs

or component damages, multivariate statistical models [71] are employed to map physical damage indicators, structural response quantities and mainshock intensity to aftershock collapse vulnerability. More advanced machine learning and pattern recognition techniques [72,92] are also applied to predict the residual structural capacity of damaged buildings using response and damage patterns. In other works [69,70], the time-dependency of the aftershock hazard were coupled with residual structural capacity of damaged buildings to achieve risk assessment. Moreover, the financial losses for structures damaged by sequential seismic events have also been studied for life-cycle loss assessment [21,68,113] and corresponding decision-making [114,115].

The above-mentioned studies provide crucial information about the post-mainshock performance of damaged buildings from various perspectives, which could be directly or indirectly used for decision-making in the aftershock environment. For example, the certain threshold for the collapse probability, residual structural capacity, financial loss or seismic risk could be used to decide whether to evacuate a damaged building, which could serve as powerful support in addition to the widely used judgment-based tagging process [12,13]. However, this is one-time decision-making rather than a series of optimal decision-making over an entire time period of interest. Time-dependent stochastic process, specifically Markov process [68,70,113,116], has been employed to probabilistically evaluate the distribution of the damage states of buildings in the aftershock environment, where the damage initially induced by the mainshock, the time-varying aftershock rates, and further progression damages due to aftershock occurrences are considered. In addition to the Markov process, Yeo and Cornell [117] further incorporated Dynamic Programming to determine the optimal action at any time point by minimizing the expected financial losses and maintaining an acceptable Equivalent-Constant Rate (ECR) of collapse [118–120] to ensure individual life-safety. In their work, constant transition probabilities under aftershocks with random magnitudes and locations were computed and scaled by the occurrence rates to account for the time-dependent transition probabilities; the repairs could be considered, but was treated as a random event rather than an optional action; linearly proportional relationship was assumed for the expected transition and disruption losses.

This chapter incorporates the aftershock hazard, the residual structural capacity of damaged tall buildings, and the expected financial losses from various sources into a time-dependent probabilistic framework based on the discrete nonstationary Markov Process. Building-level damage states are calibrated using the PSDR. Sequential NRHAs are performed

to quantify the residual structural capacity, which is then coupled with time-dependent aftershock hazard to obtain the nonstationary transition probabilities among different damage states. Expected structural and nonstructural losses are assessed for each damage state, together with the associated repair time. Two sets of actions after the mainshock are considered at any time point: whether to evacuate the building and when to reoccupy the building if it is previously evacuated; whether to repair the building and when to stop if the building had been retrofitted to a satisfactory state. Dynamic Programming is performed to find the optimal actions throughout the entire time period of interest with the objective to minimize the expected financial losses after mainshocks and the constraint defined as the transition probability into unsafety damage states. Sensitivity analyses are finally carried out to quantify the impact of the key parameters on the decision-making, including time window, safety threshold, fatality loss, disruption loss, and repair cost.

6.2 Optimal Decision-Making Framework

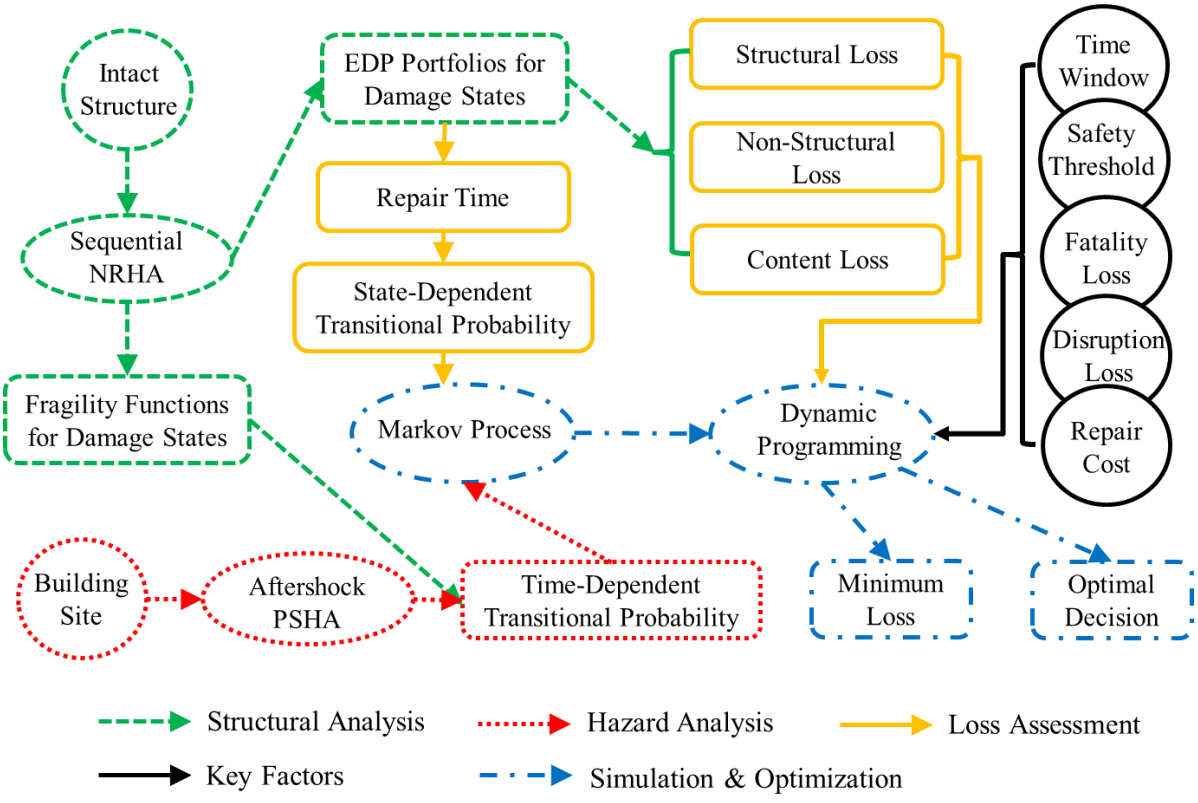

Fig. 6-1. Flow charts of framework

Fig. 6-1 provides the flow charts of the optimal decision-making framework integrating seismic hazard and structural analyses, direct (structural, nonstructural, fatality) and indirect (disruption) loss assessment, time-dependent simulation using Markov process and decision

optimization using Dynamic Programming. The 42-story dual-system archetype building introduced in Chapter 3 and used in Chapter 4 and 5 are also adopted in this chapter for illustration of the proposed framework, and the Aftershock Probabilistic Seismic Hazard Analysis (APSHA), structural modeling and ground motion selection are identical to Section 3.3. The computed APSHAs for two scenarios with relatively low and high seismicity are shown in Fig. 6-2. The daily aftershock rates right after the mainshock (0 days), 3 days and 30 days after the mainshock are compared for the two scenarios. While consistent higher rates are observed for the fault with high seismicity as time elapses in Fig. 6-2 (a), both aftershock hazards decline rapidly in the aftershock environment as shown in Fig. 6-2 (b), where the Spectra Accelerations (SAs) of 0.05g, 0.1g and 0.2g are used for illustration.

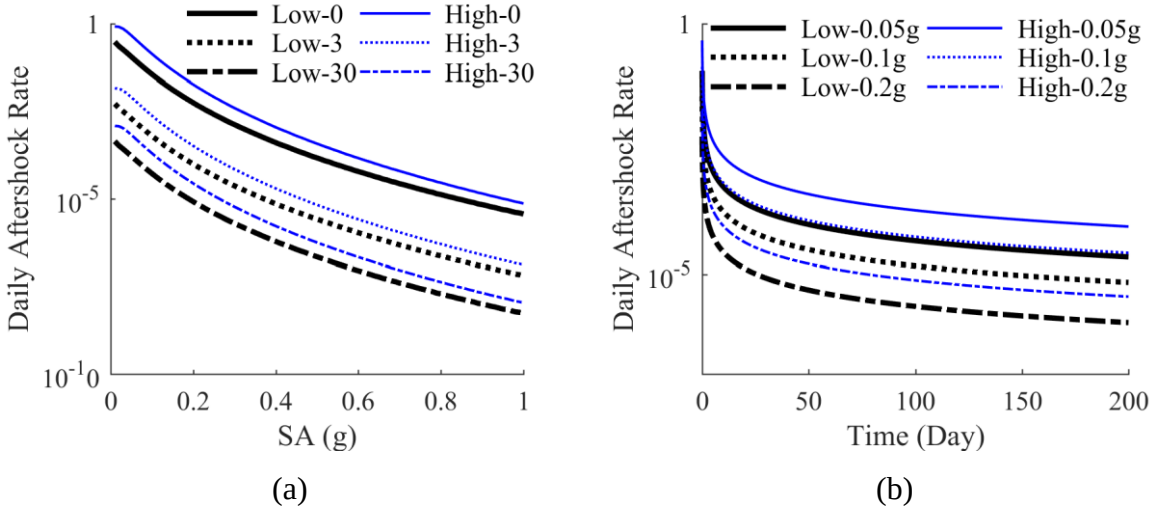

(a) (b)

Fig. 6-2. Comparison of daily aftershock rates (a) at 0, 3 and 30 days after the mainshock as SA increases and (b) with SAs of 0.05g, 0.1g and 0.2g as time elapses for the low- and high-seismicity faults, respectively

Sequential NRHAs are carried out for the structural analysis, where the intact building is subjected to a set of as-recorded mainshock-aftershock ground motions. PSDR is widely used as an indicator of the reduction in the lateral force resisting capacity of damaged buildings under sequential ground motions [21,32,33,68,69,72] and is adopted in this study as a proxy for the building damage states or performance levels. The mainshocks are first scaled such that the corresponding PSDRs fall into 10 equal intervals with a size of 0.5% and center ranging from 0.5% to 5.0% with an increment of 0.5%. The center point or median value of the associated increment interval denotes each PSDR-based damage state. For example, the 1st damage state has an interval from 0.25% to 0.75%, which is denoted by PSDR = 0.5%. Aftershocks are then applied to the damaged building to quantify the residual structural capacity in terms of fragility functions from a given damage state to all the higher ones,

conditioned on the aftershock intensities. More details are referred to Section 5.3.1. A sample comparison of fragility curves showing the probability of exceeding different PDSR levels for the intact building and the damage state corresponding to median PSDR = 1.5% (PSDR interval from 1.25% to 1.75%) is shown in Fig. 5-5. The EDP portfolios for each damage states under mainshocks and aftershocks are used for the assessment of structural and nonstructural losses as well as repair times. The details are presented in the following Section 6.3.1 and Section 6.3.2, respectively.

The time period is discretized into small increments such that the probability of more than one aftershock is negligible [62]. By integrating the fragility functions and the time-dependent aftershock hazard, transition probabilities of the nonstationary Markov process considering only progressive damages under aftershocks could be obtained to simulate the expected distribution of damage states. The expected repair times associated with different building damage states are used to generate the state-dependent stationary transition probabilities from higher damage states to lower ones, where exponential distributions are assumed for the time periods needed by the repairs to cause a damage state downgrade of the building.

Dynamic programming is then employed to efficiently target the optimal actions at each time step such that the expected financial loss is minimized at the time of decision-making, i.e., right after the mainshock. The expected financial loss integrates various sources from structural and nonstructural component damages, fatality due to collapse, disruption of residence and business and repair cost. It is the expected cumulative loss within a certain time window of interest and obtained by summing up the discounted values of all the potential losses in the future. In the following analyses, it will be referred as the financial loss for simplification. Aside from the fatality loss used to penalize the extreme scenarios where collapses occur, a certain safety threshold is also enforced in dynamic programming.

6.3 Loss Assessment of Damaged Tall Building

6.3.1 Structural and Nonstructural Loss

The portfolios of 5 EDPs for each building damage state are needed for the assessment of the expected structural and nonstructural losses using the methodology developed in FEMA P-58 [12,13], including PSDR, RSDR, Peak Floor Acceleration (PFA), CBR and Wall Chord Rotation (WCR). The losses associated with beams and columns of the special moment frames are indirectly evaluated using the PSDR. For each EDP, the 68 individual responses (recall

from Section 5.2.1, two analyses are conducted for each ground motion pair by switching the orthogonal direction of each record) for DS-5 (PSDR of 2.5%) in the X- and Z- direction [see Fig. 3-1 (b)] are shown alongside their medians and standard deviations following lognormal distributions. The median portfolios for all the 10 damage states are then presented in the two directions.

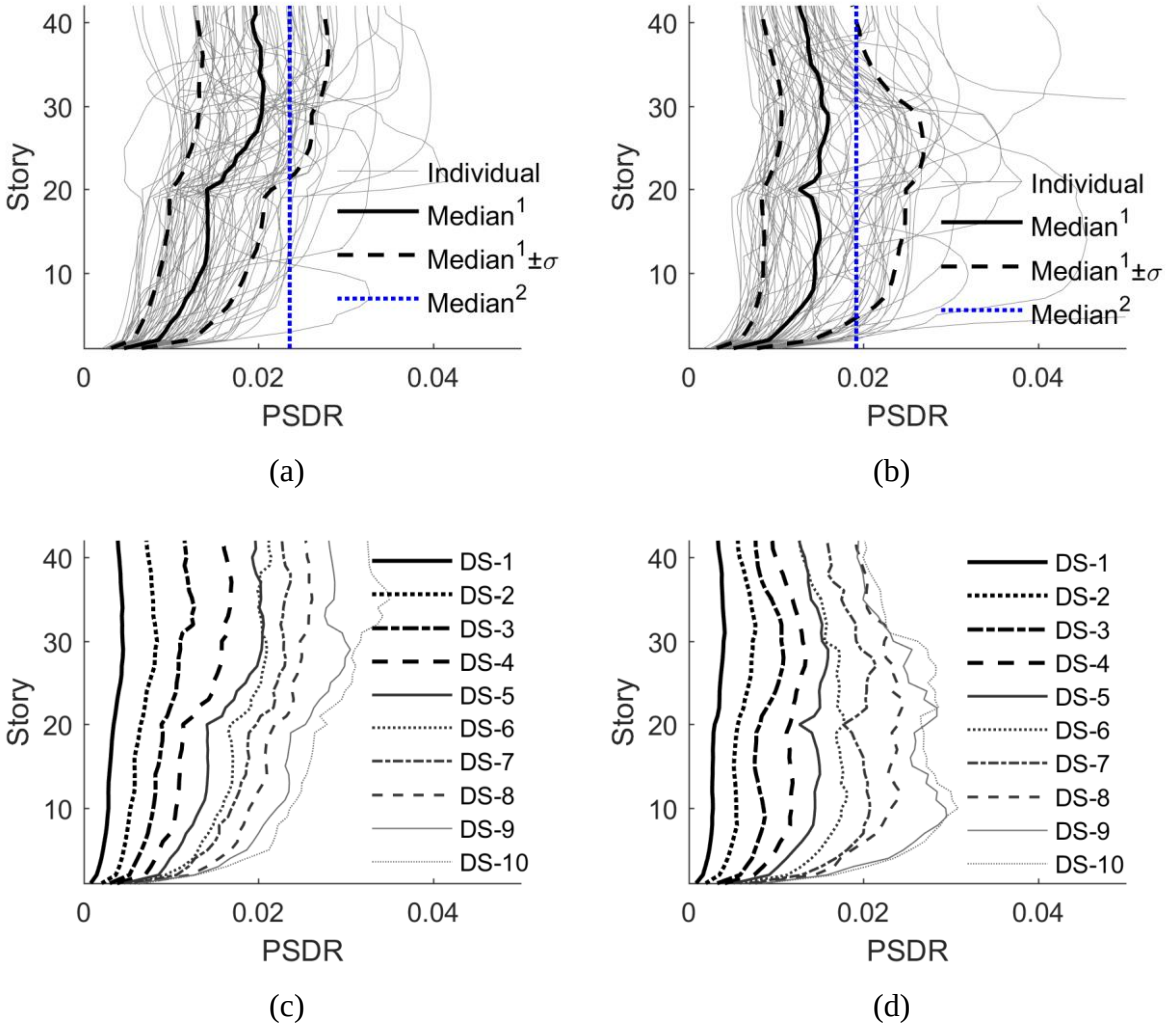

[1]Median of the PSDRs at each story from 34 ground motion pairs given DS-5

[2]Median of the maxima of PSDRs along all stories from 34 ground motion pairs given DS-5

Fig. 6-3. PSDR portfolio for DS-5 in (a) X- and (b) Z-Direction and medians for each damage sates in (c) X- and (d) Z-Direction

In Fig. 6-3 (a), while the individual PSDR responses have large variation in terms of both peak values and shapes along building height, the median as well as the standard deviations of PSDR given DS-5 show sharp change at the 20th story, possibly due to the reduce of thickness and concrete strength of the shear wall. Local maxima of median PSDRs are found within the

30th-40th stories (2.0%) and 20th-30th stories (1.5%) in X- and Z-Direction, respectively. To be consistent with the calibration of damage states, the median of the maxima of PSDRs along all stories is also presented in the two directions. 2.5% is found for X-Direction while 1.9% for Z-Direction, indicating that the performance of the former controls at this damage state. Fig. 6-3 (c) and (d) show that the median PSDR increases from 1.1% to 1.2% in X-Direction and from 1.1% to 1.2% in Z-Direction as the damage state gets higher. Consistent local maxima are reached within the 30th-40th stories in the X-Direction for all damage states, while the PSDRs near the 10th story take control beyond DS-6 in the Z-Direction. Relatively uniform and smooth shapes of PSDR portfolios are observed for lower damage states while those of the higher damage states tend to be choppier. This might be caused by the fact that the progressive damages induced by aftershocks concentrate at some of the more vulnerable stories, which significantly undermine the overall structural performance, rather than uniformly distributed into all stories. PSDR is widely used as the indicator of the sideways collapse of buildings [73–75], and the assumed thresholds vary for different structure types. The highest damage state used in this study is DS-10 with the center at 5.0% and increment interval from 4.75% to 5.25%, and the PSDR at any story exceeds 5.25% is assumed to cause collapse.

RSDR is widely used to decide whether the demolition is appropriate for severely damaged buildings when the repairs are not possible or not economic. As shown in Fig. 6-4 (a) and (b), the overall shapes of the RSDRs for DS-5 are similar with those of PSDRs in both directions, indicating a significant correlation between the two EDPs in the same direction and story. The medians of RSDRs at each story reach local maxima of 0.6% and 0.4% in the X- and Z-Directions, while the median of the maxima along all stories have slightly higher values of 0.8% and 0.5%, respectively. Per FEMA P-58 [12,13], a lognormal distribution is assumed for the RSDR that triggers demolition and the associated fragility function, where the median and dispersion are set as 2.5% and 10% for the 42-story dual-system building under study. For a given record, the maxima RSDR along all stories is used in the fragility function. Fig. 6-4 (c) and (d) show that the medians of RSDRs for the first three damage states are very limited, but they increase more aggressively beyond DS-4, i.e., considerable RSDRs have remained when the PSDR exceeds 2%.

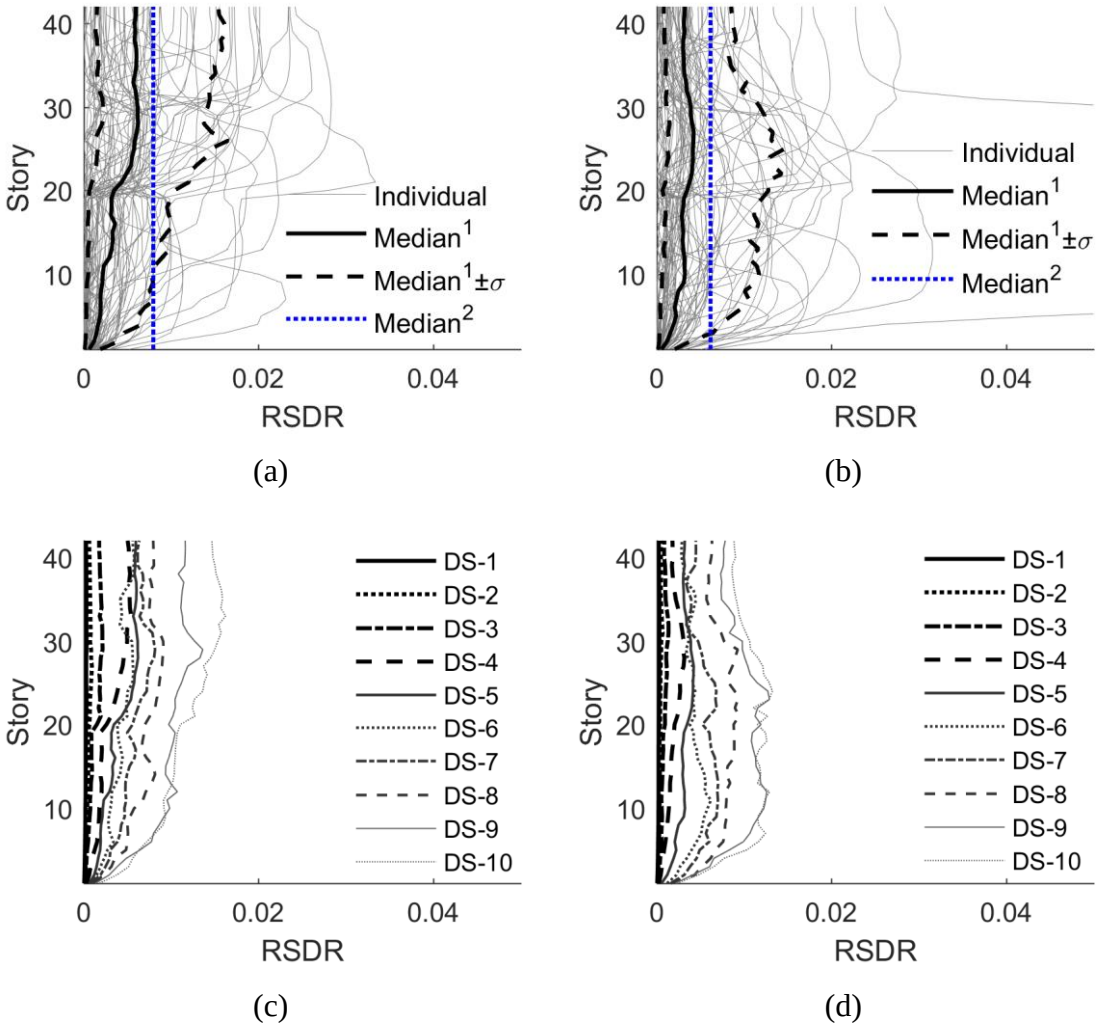

[1]Median of the RSDRs at each story from 34 ground motion pairs given DS-5

[2]Median of the maxima of RSDRs along all stories from 34 ground motion pairs given DS-5

Fig. 6-4. RSDR portfolio for DS-5 in (a) X- and (b) Z-Direction and medians for each damage sates in (c) X- and (d) Z-Direction

PFA is used to simulate damage to acceleration sensitive non-structural components and contents such as ceiling tiles and plumbing lines. Fig. 6-5 (a) and (b) show the individual PFA responses as well as their median profiles in the X- and Z-Direction, respectively. The magnitude and shape of the PFAS are very close to each other in the two directions. The PFA gets local minima at the base level and keeps decreasing as the height increases until it reaches around the 40th floor, where a sharp reverse is observed. This is because the 42-story archetype building has a penthouse at the top. As shown in Fig. 6-5 (c) and (d), the medians of the PFAs in the two directions have considerable increments from DS-1 to DS-5; however, they tend to cluster beyond DS-6 and no significant increases are found.

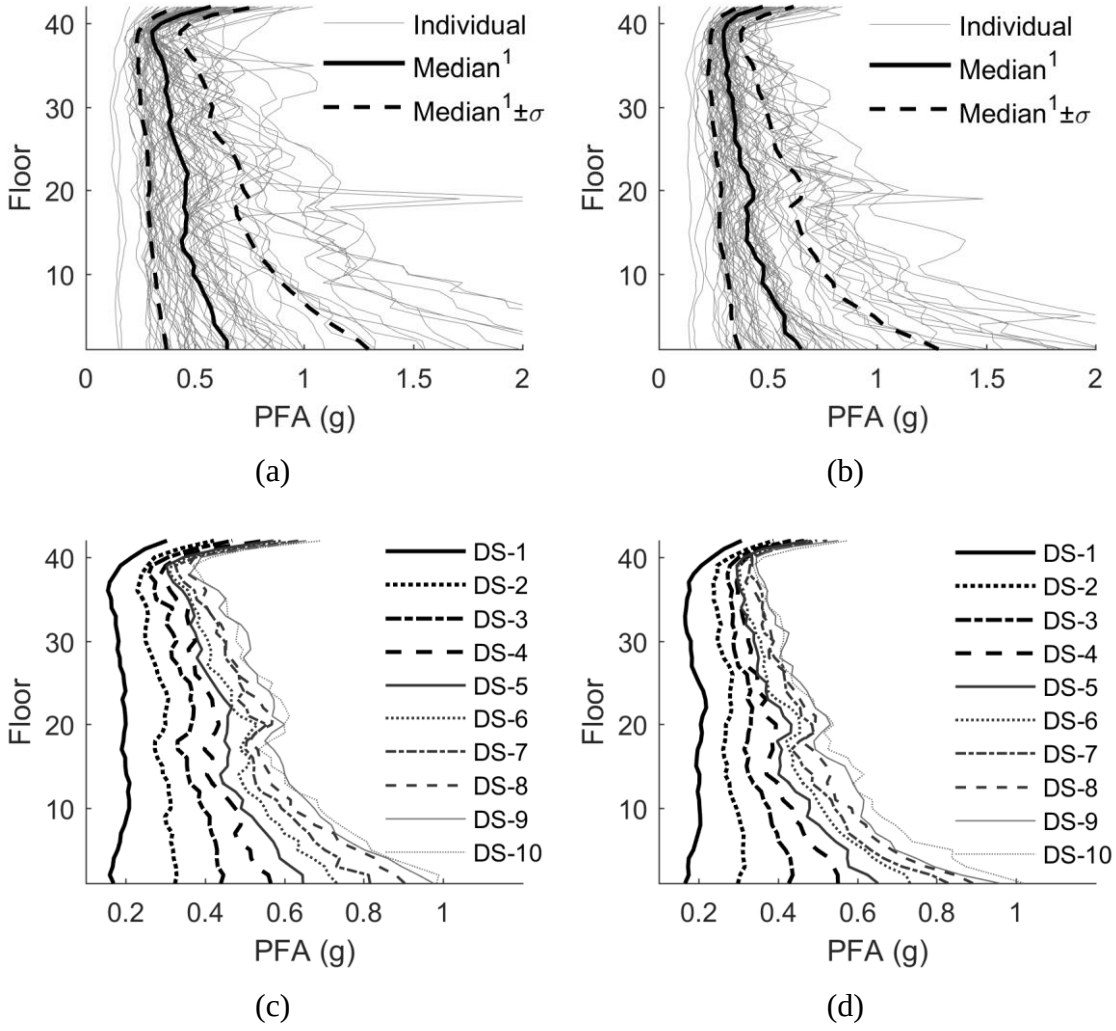

Fig. 6-5. PFA portfolio for DS-5 in (a) X- and (b) Z-Direction and medians for each damage sates in (c) X- and (d) Z-Direction

In Fig. 6-6 (a) and (b), significant variations are observed for individual responses of CBR in terms of both peak values and shapes along the building height, indicating that the CBR is very sensitive to the record-to-record uncertainty of ground motion records and potentially to the seismic performance of the damaged tall buildings, which will be discussed in detail in the following chapters. This is also confirmed by the large standard deviations of CBR in both directions. The median of the CBR in DS-5 increases almost monotonically in the X-Direction, with a sharp jump around the 21st Floor. As for the Z-Direction, the median reaches the local minima within the 20th to the 30th floor and decreases beyond the 30th floor. Both could possibly be explained by the concrete strength and cross section changes in the corresponding stories. In Fig. 6-6 (c) and (d) show shifts with similar increments and shapes for the medians of CBRs when the damage states go up to DS-5 and DS-7 (inclusively) in the X- and Z-Directions. The

higher damage states are observed to have the medians of CBRs beyond 8 %, indicating significant component damages.

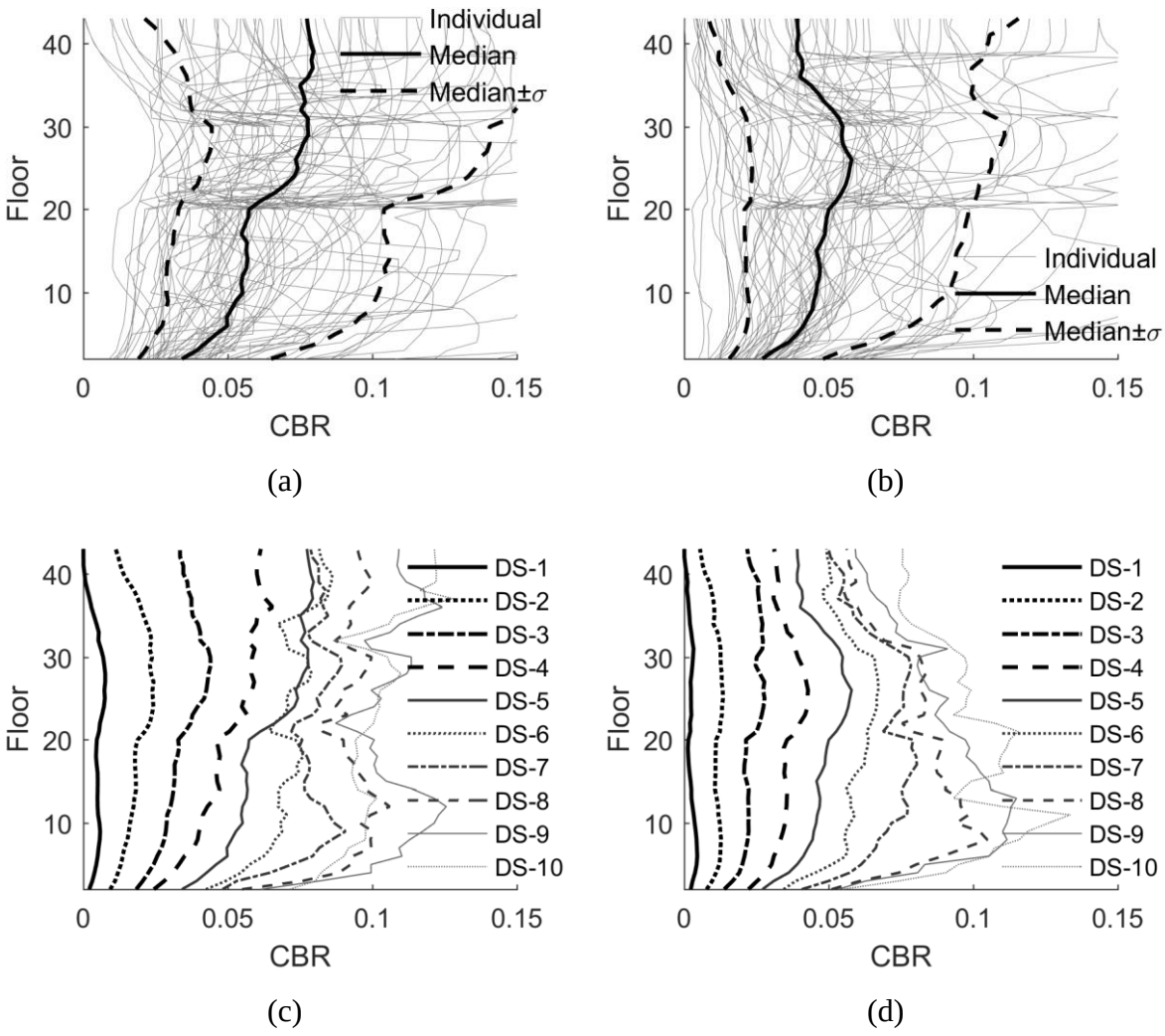

Fig. 6-6. CBR portfolio for DS-5 in (a) X- and (b) Z-Direction and medians for each damage sates in (c) X- and (d) Z-Direction

The WCR portfolios including individual responses, medians and standard deviations for DS-5 in X- and Z-Direction in depicted in Fig. 6-7 (a) and (b), respectively. As mentioned in Section 0, the shear walls are weakened in the design as the story gets higher. As a result, some sharp jumps are observed for the medians of WCRs at the boundaries of different designs of shear walls, i.e., 20th and 30th stories. The 1st story also has a local minimum for the medians of WCRs because of the hinge effects of shear walls and an increase in the story height. The medians of WCRs shown in Fig. 6-7 (c) and (d) all have very similar shapes and almost increase linearly as the damage state is severer. In general, the WCRs are limited across all damage states and the associated financial losses are expected to be not significant.

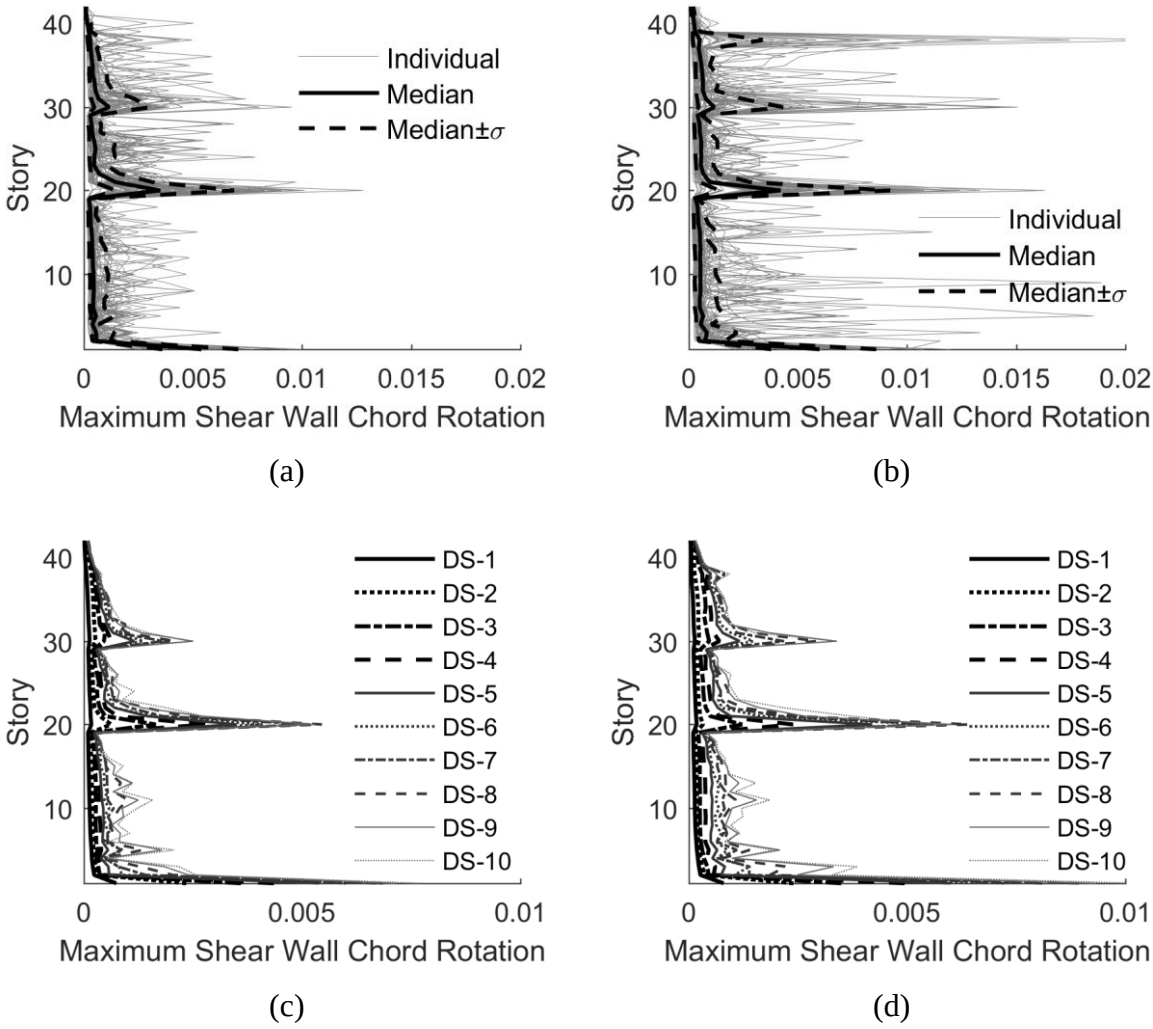

Fig. 6-7. WCR portfolio for DS-5 in (a) X- and (b) Z-Direction and medians for each damage sates in (c) X- and (d) Z-Direction

With the EDPs for all the damage states available, the expected loss assessment of structural and nonstructural components can finally be performed using the methodology developed in FEMA P-58 [12,13]. Given the EDP portfolios from the 34 pairs of ground motions, significantly more instances are sampled based on their joint correlations. The instances of damaged buildings are first classified into collapse and non-collapse cases, followed by further splits into reparable or nonrepairable ones, of which the latter trigger the demolition. If an instance is deemed as reparable, Monte Carlo simulation is then employed to sample component-level damage states and associated financial losses from the given EDP based on the fragility curves established by previous component experiments or engineering experiences. The Seismic Performance Prediction Program (SP3) developed by Haselton Baker Risk Group is used for the numerical computation of the loss and downtime assessment.

The archetype tall building is evaluated with a total value of 228 million dollars including 197 and 31 million dollars for the construction and content costs respectively. The expected number of residents is assumed to be 1471 based on the total building area. The methodology is applied using to obtain the estimation of the mean financial losses for all damage states shown in Fig. 6-8. As PSDR itself is used to calibrate the damage state of the building and the maximum PSDR is capped at 5.25% for DS-10, the collapse cases are not considered for the loss assessment here but are addressed directly in the dynamic programming later. As we can see from Fig. 6-8, the financial losses from structural damages dominate up to DS-4 (inclusively), but those caused by the excessive RSDR (demolition) take control after DS-5. A more detailed list for the factions of damages from various sources is presented in Table 6-1.

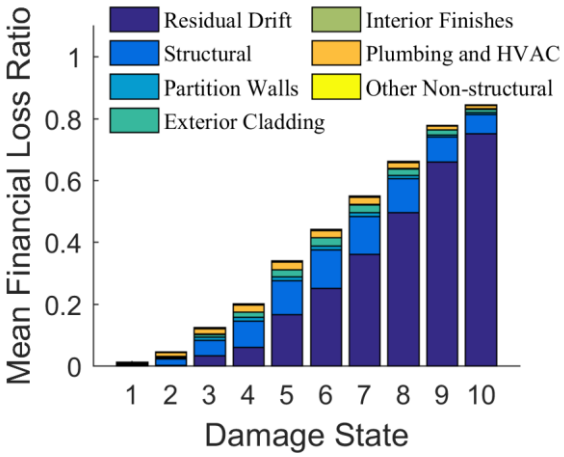

Fig. 6-8. Estimation of the mean financial losses from different categories for each damage state using SP3

Table 6-1. Details of losses from different categories for each damage state using SP3 (unit: %)

Category	1	2	3	4	5	6	7	8	9	10
Residual Drift	0.00	0.25	3.39	6.03	16.7	25.2	36.0	49.7	66.0	75.3
Structural Component	0.40	1.97	4.99	8.52	11.0	12.4	12.4	10.9	8.05	6.18
Partition Walls	0.20	0.58	0.91	1.20	1.29	1.29	1.19	0.99	0.70	0.52
Exterior Cladding	0.04	0.30	0.95	1.72	2.25	2.51	2.48	2.17	1.58	1.21
Interior Finishes	0.01	0.04	0.08	0.11	0.13	0.15	0.19	0.15	0.10	0.12
Plumbing and HVAC	0.40	1.22	1.82	2.19	2.16	2.16	2.25	1.86	1.15	1.05
Other Non-structural	0.11	0.25	0.34	0.40	0.43	0.46	0.46	0.41	0.29	0.24
Total	1.15	4.61	12.5	20.2	33.9	44.1	55.0	66.2	78.0	84.6

6.3.2 Repair Time and Cost

The expected repair times needed for recovery to intact state from any higher damage states are shown in Fig. 6-9. Two approaches are used, i.e., the FEMA P-58 and REDi. The parallel and series approaches of P-58 are observed to be the lower and upper bounds of the expected repair times across all damage states. This is trivial as the former allows all the repairs of different components being conducted at the same time as the latter require the repairs being performed one by one. REDi [121] is a detailed downtime assessment methodology proposed by Comerio to probabilistically estimate the contribution from different components and account for both direct repairs and impeding factors. More applications, discussions, and updates could be found for the REDi methodology in recent researches [122–125], which is out of the scope of the current study. The expected repair time for the series approach reaches a plateau more than 1000 days beyond DS-5 while that of the parallel approach shows an almost linear increase after DS-4 (110 days). The expected repair times for the three performance levels (re-occupancy, functional recovery, and full recovery) following REDi are very close to each other and come somewhere in between the previous P-58 approaches.

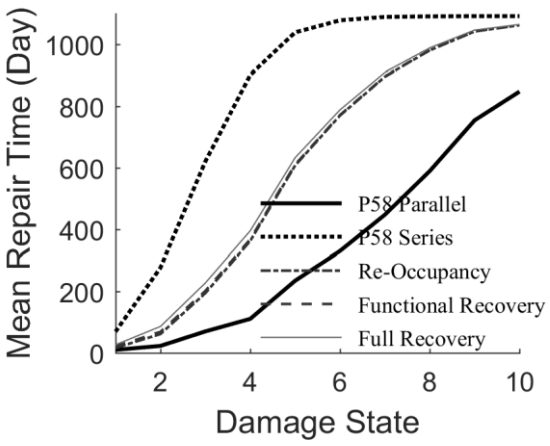

Fig. 6-9. Estimation of the mean repair time following P-58 and REDi methodologies for each damage state using SP3

Another piece of useful information, the expected repair time $T_{i,j}^{R}$ from a given higher damage state DS-i back to a target lower one DS-j, is assumed to following the relationship shown in Equation 6.1. The obtained lower-triangular matrix is depicted in Table 6-2. The damage state is capped at DS-8 as higher damage states are assumed to be unrepairable or not economic to repair. A constant repair cost of 0.15 million dollars per day is used in the following analysis if not otherwise declared, for example, in the sensitivity analyses.

$$T_{i,j}^{R} = T_{i,0}^{R} - T_{j,0}^{R} \quad (6.1)$$

where $i > j$ denote a higher damage state i and a lower damage state j; $T_{i,0}^{R}$ is the expected time to DS-0 from a given DS-i for the performance level of reoccupancy obtained by REDi.

Table 6-2. Expected repair time to retrofit the tall building from a higher damage state[1] back to a lower one (unit: day)

DS	0	1	2	3	4	5	6	7
1	16							
2	61	45						
3	195	178	133					
4	362	346	301	168				
5	608	591	546	413	245			
6	770	754	709	576	408	163		
7	896	880	835	702	534	288	126	
8	980	964	919	786	618	373	210	84

[1]The building is assumed to be non-reparable beyond DS-9 (inclusively)

6.3.3 Fatality and Disruption Loss

The fatality loss is assumed to be 5 million dollars per person if not otherwise adjusted, and no survivals are considered if the building is occupied at the time of the collapse, meaning a total fatality loss is assigned to the collapse state, DS-12.

A full (cap) disruption loss of 0.7 million dollars per day is used when the damaged building is evacuated or collapses in the aftershock environment. If reoccupancy is allowed, the disruption loss from DS-0 to DS-10 is assumed to be proportional to the cap disruption loss. Starting from 0% of DS-0, the fraction goes up to 50% for DS-10 with an increment of 5%.

6.4 Markov Process Based on the Damage States

6.4.1 Considering Progressive Damage under Aftershocks

A nonstationary Markov process is adopted to probabilistically evaluate the expected distribution of building-level damage states by incorporating the progressive damages of the building and time-dependent aftershock hazard, which starts from significantly higher rates compared with those of mainshocks but decreases rapidly. A given time window of interest is

discretized into small time steps to exclude the scenario where more than one aftershock occur [62] and to ensure the accuracy for numerical integration where shape descending slopes are observed for the aftershock hazard curves in Fig. 6-2. After a series of preliminary analyses, the time step of 0.05 day is deemed as appropriate for the current study. A total of 12 building-level damage states are defined by adding the intact state DS-0 and the collapse state DS-11 (PSDR > 5.25%) in addition to the previously mentioned 10 ones. Recall from Section 5.3.3, Equation 5.6 shows the 12-by-12 upper triangular Markov transition matrix at each time step for a single fault. Each entry describes the probability of transitioning between any two damage states, which is computed using Equations 5.7 and 5.8. Given an initial probability distribution, the time-dependent probability distribution in the post-mainshock environment is computed using Equation 5.9 by cumulatively multiplying the Markov transition matrices. The only notation change is that the variable *n* used as the identification of a fault is set to *L* and *H* to represent the low- and high-seismicity scenarios used for comparison in this chapter.

A time window of 200 days after a mainshock is used in this chapter to provide optimal decision-making throughout a long enough period. Examples of transition matrices for the damage states corresponding to (a) immediately following the mainshock, (b) 30 days and (c) 200 days after the mainshock of the low- and high-seismicity scenarios are shown from Table 6-3 to Table 6-5 and from Table 6-6 to Table 6-8, respectively. As shown earlier in Fig. 6-2, the transition probability decreases fast as the aftershock hazard declines. Almost consistent larger transition probabilities are almost always found for the high-seismicity fault for the same entries. It is observed that the diagonal entries are always significantly larger than the off-diagonal ones in the same row, indicating low probabilities of transitioning to higher damage states in the aftershock environment. The M_n^s in Equation 5.6 is replaced by M_L^s and M_H^s here to denote the Markov transition matrix of the low- and high-seismicity faults at time step *s*, respectively. For the same fault, the off-diagonal entries drop significantly from M_L^1 (M_H^1) to M_L^{600} (M_H^{600}) and almost close to zeros in M_L^{4000} (M_H^{4000}) for while the diagonal entries approach 1.0, which reflects the time-dependent decrease in aftershock hazard. As expected, consistently considerable higher transition probabilities are found at the corresponding entries for the high-seismicity fault over the low-seismicity one. It is noted that these matrices only reflect the stand-alone transition probabilities during the very short time step (0.05 day).

Table 6-3. Markov transition matrix M_L^1 (unit: 10^{-3})

DS	0	1	2	3	4	5	6	7	8	9	10	11
0	807	135	38.1	9.17	4.628	1.826	0.779	0.459	0.561	0.250	0.276	1.191
1		922	47.1	13.11	7.308	3.053	1.368	0.877	0.955	0.445	0.525	1.438
2			979	10.06	4.695	1.795	1.294	0.665	0.623	0.359	0.270	1.792
3				979	8.497	4.383	2.097	1.474	0.866	0.923	0.203	2.096
4					980	8.350	3.614	1.882	2.398	1.267	0.689	2.423
5						978	9.912	5.084	2.071	1.738	0.711	2.878
6							973	10.48	5.770	2.413	2.738	4.832
7								980	7.568	3.149	3.058	5.692
8									963	6.709	6.640	22.75
9										961	4.983	26.60
10											973	33.64
11												1000

Table 6-4. Markov transition matrix M_L^{600} (unit: 10^{-6})

DS	0	1	2	3	4	5	6	7	8	9	10	11
0	10^6	199	56.50	13.57	6.851	2.703	1.153	0.679	0.831	0.370	0.409	1.763
1		10^6	69.79	19.41	10.81	4.519	2.025	1.299	1.414	0.659	0.777	2.128
2			10^6	14.89	6.950	2.657	1.916	0.984	0.922	0.532	0.399	2.652
3				10^6	12.57	6.488	3.104	2.183	1.282	1.366	0.300	3.103
4					10^6	12.36	5.351	2.786	3.550	1.875	1.020	3.587
5						10^6	14.67	7.526	3.066	2.573	1.053	4.261
6							10^6	15.52	8.541	3.572	4.053	7.152
7								10^6	11.20	4.661	4.527	8.426
8									10^6	9.931	9.829	33.69
9										10^6	7.376	39.38
10											10^6	49.81
11												10^6

Table 6-5. Markov transition matrix M_L^{4000} (unit: 10^{-7})

DS	0	1	2	3	4	5	6	7	8	9	10	11
0	10^7	257	72.87	17.51	8.836	3.486	1.487	0.876	1.071	0.477	0.527	2.273
1		10^7	90.01	25.03	13.95	5.829	2.612	1.675	1.824	0.850	1.002	2.745
2			10^7	19.21	8.963	3.427	2.471	1.269	1.189	0.686	0.515	3.421
3				10^7	16.22	8.368	4.004	2.815	1.653	1.762	0.387	4.003
4					10^7	15.94	6.901	3.594	4.579	2.419	1.316	4.626
5						10^7	18.92	9.707	3.955	3.318	1.358	5.496
6							10^7	20.02	11.01	4.607	5.228	9.225
7								10^7	14.44	6.012	5.839	10.86
8									10^7	12.80	12.67	43.45
9										10^7	9.513	50.80
10											10^7	64.24
11												10^7

Table 6-6. Markov transition matrix M_H^1 (unit: 10^{-3})

DS	0	1	2	3	4	5	6	7	8	9	10	11
0	294	477	154.6	35.89	17.41	6.634	2.774	1.561	1.971	0.863	0.951	3.871
1		690	191.9	52.48	28.36	11.51	5.053	3.138	3.484	1.598	1.883	4.680
2			921.0	39.46	17.78	6.485	4.707	2.317	2.158	1.270	0.907	5.927
3				922.0	33.30	16.86	7.847	5.492	3.162	3.427	0.660	7.165
4					923.5	32.85	13.93	7.070	9.331	4.785	2.541	8.595
5						915.2	39.00	19.92	7.982	6.676	2.563	9.742
6							898.5	41.01	22.65	9.418	10.77	17.62
7								924.9	29.69	12.31	12.06	21.00
8									860.1	26.39	25.63	87.80
9										853.1	19.08	102.9
10											897.0	127.7
11												1000

Table 6-7. Markov transition matrix M_H^{600} (unit: 10^{-6})

DS	0	1	2	3	4	5	6	7	8	9	10	11
0	10^6	70.73	22.88	5.314	2.578	0.982	0.411	0.231	0.292	0.128	0.141	0.573
1		10^6	28.41	7.770	4.199	1.705	0.748	0.465	0.516	0.237	0.279	0.693
2			10^6	5.843	2.633	0.960	0.697	0.343	0.320	0.188	0.134	0.877
3				10^6	4.930	2.497	1.162	0.813	0.468	0.507	0.098	1.061
4					10^6	4.863	2.063	1.047	1.381	0.708	0.376	1.272
5						10^6	5.774	2.949	1.182	0.988	0.379	1.442
6							10^6	6.071	3.354	1.394	1.595	2.609
7								10^6	4.396	1.823	1.786	3.109
8									10^6	3.907	3.795	12.99
9										10^6	2.825	15.24
10											10^6	18.91
11												10^6

Table 6-8. Markov transition matrix M_H^{4000} (unit: 10^{-7})

DS	0	1	2	3	4	5	6	7	8	9	10	11
0	10^7	912	295.1	68.53	33.24	12.666	5.297	2.979	3.764	1.648	1.816	7.392
1		10^7	366.4	100.2	54.16	21.98	9.648	5.991	6.653	3.051	3.595	8.936
2			10^7	75.357	33.95	12.38	8.987	4.424	4.121	2.425	1.731	11.31
3				10^7	63.58	32.20	14.98	10.48	6.037	6.544	1.259	13.68
4					10^7	62.72	26.61	13.49	17.81	9.136	4.851	16.41
5						10^7	74.47	38.03	15.24	12.74	4.894	18.60
6							10^7	78.30	43.25	17.98	20.57	33.65
7								10^7	56.70	23.50	23.03	40.09
8									10^7	50.39	48.94	167.6
9										10^7	36.43	196.5
10											10^7	243.9
11												10^7

A vector representing the initial distribution of the building damage states are needed to start the Markov process. For the case where the damage state right after a mainshock is known for sure, 1 is assigned at the entry corresponding to the specific damage state and 0's for all the other entries. A predefined distribution representing the partial belief with the uncertainty of the damage states could also be an alternative option when desired. In the following section, only the former scenario is considered. Using the low-seismicity fault for illustration, the initial damage state of the building right after a mainshock could be assigned as $p_{L,0}^0 = 1$ (or $p_{L,5}^0 = 1$) and the rest 0's in Equation 5.9, indicating the building remains intact (or suffers the PSDR of 2.5%) in the mainshock.

6.4.2 Considering Recovery by Repair

The matrices of the Markov process in Section 6.4.1 only have the diagonal and upper-triangular entries as they exclude the scenarios where the damaged buildings recover from a higher damage state to a lower one, but this could happen when the repairs are performed. To effectively account for such possibilities, the Poisson process is used to simulate the event of transition between building-level damage state triggered by the repairs. For any given damage state higher than DS-1 (inclusively) but lower than DS-8 (inclusively), a damaged building is assumed to be able to recover to any lower damage state bounded by DS-0 (inclusively). Given the property of the Poisson process, the time interval of the occurrence of any two events follows an exponential distribution. The daily rate of an event where the building is recovered from higher DS-i back to a target lower DS-j is then assumed to be the inverse of the corresponding expected times obtained from Section 6.3.2. The transition probability from a higher DS-i back to a target lower DS-j for time step s is denoted as $\pi_{R,i,j}^s$ and defined in Equation 6.2. Different with the transition matrix for the progressive damage under aftershocks, the transition matrix for repairs is independent of time and thus stationary.

$$\pi_{R,i,j}^s = \left(\frac{1}{T_{i,j}^R}\Delta_t\right)e^{-\left(\frac{1}{T_{i,j}^R}\Delta_t\right)} \tag{6.2}$$

where $i > j$ denote a higher damage state i and a lower damage state j; $T_{i,j}^R$ is the expected time to retrofit the damaged building from DS-i back to a target DS-j, and $\frac{1}{T_{i,j}^R}$ is the daily rate of the corresponding event; Δ_t is the time step; $\frac{1}{T_{i,j}^R}\Delta_t$ gives the rate for the exponential distribution.

Table 6-9. Constant transition probabilities for the tall building from certain damage state[1] back to any lower ones in each time step (unit: 10^{-6})

DS	0	1	2	3	4	5	6	7
1	609							
2	162	221						
3	51.4	56.1	75.1					
4	27.6	28.9	33.2	59.5				
5	16.4	16.9	18.3	24.2	40.7			
6	12.9	13.2	14.1	17.3	24.5	61.5		
7	11.1	11.3	11.9	14.2	18.7	34.6	79.4	
8	10.2	10.3	10.8	12.7	16.1	26.8	47.5	118

[1]The building is assumed to be non-reparable beyond DS-9 (inclusively)

6.5 Dynamic Programming for Optimal Decision-Making

Given the Markova process and financial loss assessment for different damage states established in previous sections, the optimal action at each time step could be obtained by minimizing the financial loss right after a mainshock by considering the entire time period of interest. The available actions at each time step are whether to evacuate the building or reoccupy the building if previously evacuated and whether to repair the damaged building and when to stop if previously started. This ends up with four possible actions: *Evacuate* & *Repair* (*ER*), *Evacuate* & *Non-Repair* (*ENR*), Reoccupy & *Repair* (*RR*), *Reoccupy* & *Non-Repair* (*RNR*). A strict constraint is applied to ensure life safety in addition to the fatality loss already incorporated in the objective of financial loss. Damage states beyond DS-9 (inclusively) are deemed as unsafe, and the building is forced to evacuate, and no repairs are allowed if the total probability of transition into these damage states exceeds a certain threshold. This leaves only *ENR* available for this scenario. However, when the building is evacuated only as a result of minimizing the financial loss, *ER* and *ENR* are both valid. A time window of 200 days is used in the following sections if not otherwise declared.

A naïve approach to solve for the optimal action at each time step would be enumerating all the possible sequences from the start all the way to the end of the time window of interest, and then selecting the one gives the minimal financial loss. However, this could be very time consuming as the time complexity is exponential. For example, the 4000 time steps each with 12 damage states and a maximum of 4 possible actions would give a total of $(4 \times 12)^{4000}$

distinct sequences to explore, which is not feasible. As a result, dynamic programming is employed to achieve a far more efficient solution, where only linear time complexity is needed. This is done by recognizing the fact that we can easily choose the optimal action at time step s if all the optimal actions are already available for all possible building damage states at time step $s+1$. By working backward step by step to obtain the optimal actions and associated minimal financial loss, dynamic programming is able to reduce all the repeated calculation in the naïve approach. Based on the loss assessment and the Markov process introduced in previous sections and the initial work of Yeo and Cornell's [117], the dynamic programming with simplified equations, the action option of repairs and more realistic financial losses is finally applied.

As shown in Equation 6.3, looping over all the possible actions (A_i^s) at time step s when the building starts with DS-i would give the optimal actions $\left(a_i^{s,*}\right)$ and its associated minimal financial losses $[L_i^{s,*}\left(a_i^{s,*}\right)]$. For the damaged building in DS-i at time step s, $L_i^s(a_i^s)$ denotes the financial loss from the last time step all the way to the current step s if a_i^s is the action at time step s, which consists of the losses from 1) the building transferring to a higher damage state $[L_{T,i}^s(a_i^s)]$, 2) remaining in the same damage state ($L_{N,i}^s$), and 3) the gains when the building recovers to a lower damage state $[R_i^s(a_i^s)]$ if the current action (a_i^s) includes repairs. These different scenarios are mutually exclusive and collectively exhaustive and defined through Equation 6.4 and 6.6 using recursion, meaning any value at time step s is expressed in terms of the corresponding one in time step $s+1$. For the scenario where the building transforms to a higher damage state, Equation 6.4 sums up the financial losses from all possible damage states weighted by the transition probabilities at time step s ($\pi_{i,j}^s$). From DS-i to DS-j, it includes a one-time damage-state transition loss $[l_{i,j}^B(a_i^s)]$ given any possible action (a_i^s), the mean disruption loss $[\frac{1}{2}(l_i^D + l_j^D)\Delta_t]$ by assuming the expected arrival time of the transition is in the middle of the time step and the discounted minimal financial loss from the higher damage state DS-j ($L_j^{s+1,*}e^{-\alpha\Delta_t}$). When the building is occupied, the damage-state transition loss $[l_{i,j}^B(a_i^s))$ is obtained by taking the difference of the expected financial losses of the DS-i and DS-j assessed in Section 6.3.1; however, only 86% of those are used when the building is evacuated to exclude the content losses. Equation 6.5 quantifies the expected loss when the building remains in the same damage state, including the disruption loss for DS-i and the discounted minimal financial loss from the same damage state ($L_i^{s+1,*}e^{-\alpha\Delta_t}$). The potential gain

for the repairs defined in Equation 6.6 has similar components with Equation 6.4 with three key differences: 1) the additional cost for performing the repair at time step s $[l^R(a_i^s)\Delta_t]$; 2) the one-time damage-state transition gain $[-l_{i,j}^B(a_i^s)]$ given any possible action (a_i^s), 3) transition is only considered from a higher damage state to a lower one. The term $R_i^s(a_i^s)$ could be simply set to zero if no repairs are considered. Equation 6.7 restricts the action to *ENR* when the transition probability into unsafety damage states exceeds the predefined threshold.

$$L_i^{s,*}\left(a_i^{s,*}\right) = \min_{a_i^s \in A_i^s}[L_{T,i}^s(a_i^s) + L_{N,i}^s + R_i^s(a_i^s)] \tag{6.3}$$

$$L_{T,i}^s(a_i^s) = \sum_{j=i+1}^{k} \pi_{i,j}^s \left[l_{i,j}^B(a_i^s) + \frac{1}{2}(l_i^D + l_j^D)\Delta_t + L_j^{s+1,*}e^{-\alpha\Delta_t}\right] \tag{6.4}$$

$$L_{N,i}^s = \pi_{i,i}^s(l_i^D\Delta_t + L_i^{s+1,*}e^{-\alpha\Delta_t}) \tag{6.5}$$

$$R_i^s(a_i^s) = l^R(a_i^s)\Delta_t + \sum_{1}^{i-1} \pi_{i,j}^s \left[-l_{i,j}^B(a_i^s) + \frac{1}{2}(l_i^D + l_j^D)\Delta_t + L_j^{s+1,*}e^{-\alpha\Delta_t}\right] \tag{6.6}$$

$$A_i^s \overset{\text{def}}{=} \begin{cases} \{ER, ENR, RR, RNR\}, \text{if } P_u^s < P_0 \\ \{ENR\}, \text{if } P_u^s \geq P_0 \end{cases} \tag{6.7}$$

where $i, j = 0, \ldots, 11$ identifies the damage state in time step s and $s+1$; $*$ marks the optimal value; α denotes the daily discount rate corresponding to an assumed annual discount rate of 4%; Δt is the size of the time step; $\pi_{i,j}^s$ is the transition probability from DS-i to DS-j at time step s, where the identification for fault in previous sections is removed for simplification here; a_i^s is the action at time step s given the building ends in DS-i from time step $s-1$; $l_{i,j}^B(a_i^s)$ is the one-time damage-state transition loss given action a_i^s; l_i^D (l_j^D) is the disruption loss if the building is in DS-i (j); $l^R(a_i^s)$ represents the constant daily cost for repairs if $a_i^s \in \{ER, RR\}$, otherwise equals 0; P_u^s is the probability of transition into unsafe damage sates (higher or equal to DS-9) and P_0 is the corresponding acceptable threshold.

In the following sections, the optimal actions and corresponding minimal financial losses are obtained following the dynamic programming, where both low- and high-intensity scenarios are considered for comparison. Four distinct cases are explored by considering 1) safety threshold only, 2) financial loss and safety threshold, 3) financial loss and repair and 4) financial loss, safety threshold, and repair. While only the last case applies the full process of the dynamic programming introduced earlier, the first 3 ones also give insights into the partially

simplified process when deemed appropriate in engineering practices. For all the cases, no policy is presented for damage state beyond DS-9 (inclusively) as they are assumed to be unsafe and simply be evacuated without question. It is noted that the financial loss is the additional loss in the aftershock environment, and the one-time transition loss of the building from intact to any damage state already happened and is set aside. The financial loss is the sum of these two parts, but only the former is used for decision-making as we can only make arrangement for the future. It is important to note that the results of the dynamic programming are only valid for the time window considered, and the seismic hazard includes only the aftershock hazard following the already occurred mainshock without considering the mainshock hazard in the future. For example, the optimal policy in this study might end with stopping the repairs when aftershock seismic risk drops significantly and leaving the building with considerable damages; however, it could be more beneficial to keep repairing the building to the full recovery state when considering any future mainshock hazard.

6.5.1 Safety Threshold Only

The seismic risk, which is quantified as the probability of a damaged building transforming into unsafe damage sates, is the only constraint for the optimization in this case. The policy is simple, i.e., the building remains occupied if the seismic risk always below the threshold or will be issuing a permit for reoccupation as soon as the seismic risk drops below the threshold. By following this policy, this case, in fact, has no optimization for financial loss.

The dynamic programming is performed by simplifying Equation 6.3 to $L_i^{s,*}\left(a_i^{s,*}\right) = L_{T,i}^{s}\left(a_i^{s,*}\right) + L_{N,i}^{s}$, and $A_i^{s,*} = ENR$ if $P_u^s \geq P_0$ and $A_i^{s,*} = RNR$ otherwise. The exceedance rate of 2% in 50 years is used for the seismic design for the Maximum Considered Earthquake (MCE) to limit the collapse probability and ensure life safety in the pre-mainshock environment. 5 times this rate is adopted by Yeo and Cornell's [117] to compute the corresponding ECR in a much shorter time period of 0.5 days. As collapse is very rare compared with the unsafe damage sate and the time step is even reduced to 0.05 day in the current study, we further increase the threshold P_0 to 250 times the corresponding rate in 50 years for MCE in the pre-mainshock environment. Sensitivity analyses regarding this threshold are performed in the following sections to better understand its impact on the optimal decision-making and address any concerns on its assumption.

As we can see from Fig. 6-10 (a), for all post-mainshock damage states, the optimal decision is to evacuate the building right after the mainshock due to the high seismic risk within

a certain time period even for the low-seismicity scenario. The waiting time to reoccupy the building gradually increases from 6 days for the intact building to 18 days for the damaged building of DS-5. A considerably longer time of 32 and 38 days are observed for higher damage states DS-6 and DS-7, and a huge jump to 106 days for DS-8. Similar patterns could be found for the high-seismicity scenario in Fig. 6-10 (b), but as expected, consistently longer times are needed for all damage states before the reoccupancy. For example, the times for DS-0 and DS-6 rise to 19 and 109 days respectively, while the DS-8 building remains to be evacuated for the entire 200 days under consideration.

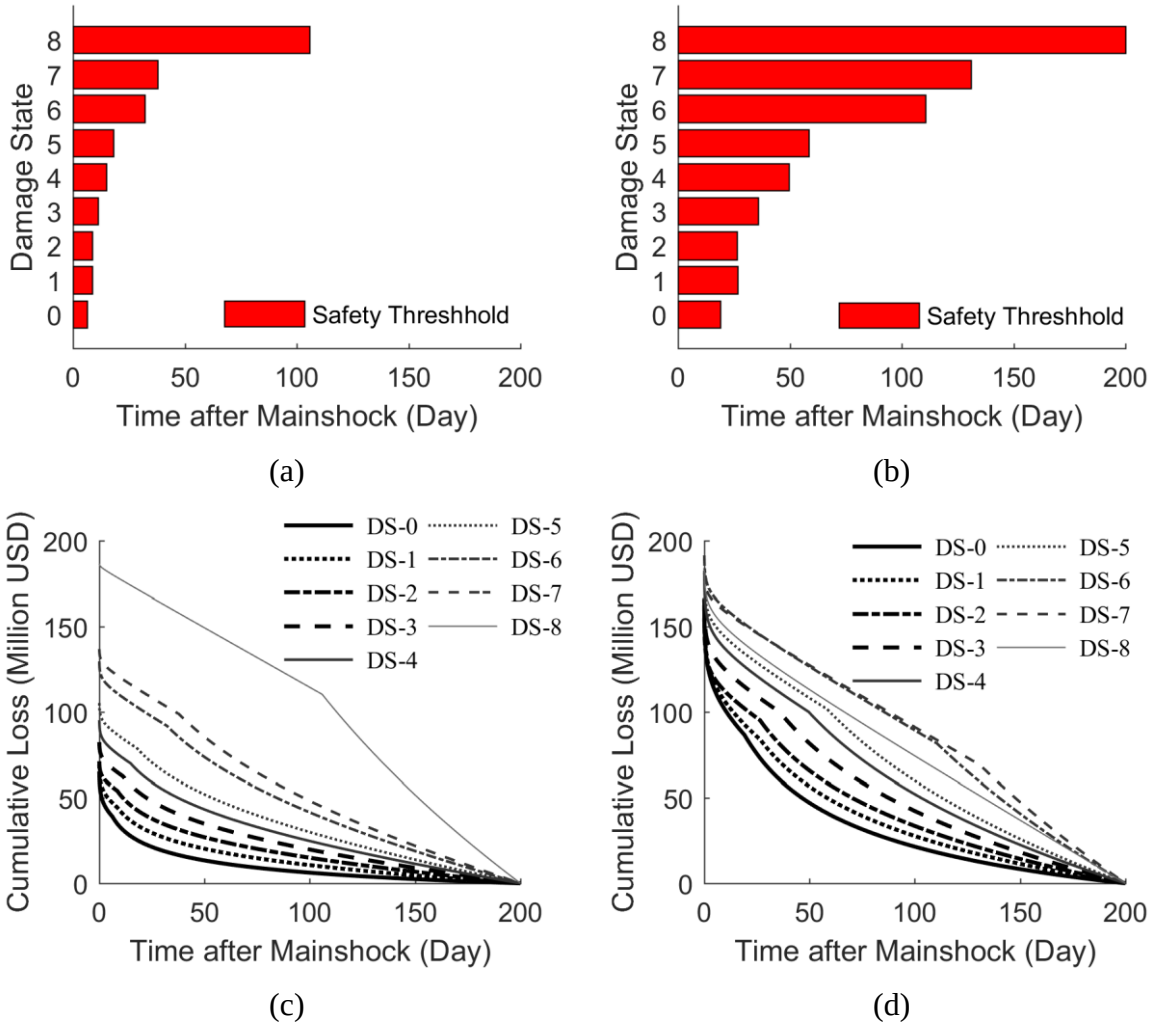

Fig. 6-10. (a-b) Actions following the safety threshold policy and (c-d) corresponding minimal financial losses for the low- and high-seismicity scenarios within 200 days after mainshock, respectively

Fig. 6-10 (c) shows the financial losses for the low-seismicity scenario given the building starts from different damage states under the mainshock. Recall from the backward calculation in dynamic programming, these curves start to cumulate from the 200 days and all the way

back to right after the mainshock, i.e., the time point we are making these decisions. By keeping the ascending order in terms of the damage state throughout the entire time period (except for DS-8 for the high-seismicity scenario, which will be discussed later), the curves reach a range of 65 to 105 million dollars right after the mainshock for DS-0 to DS-5 and 129, 136 and 185 million dollars for the last three damage states, respectively. Some sharp drops on the cumulative curves are observed at the times corresponding to the reoccupancy as a result of the difference between the significant reduction in disruption losses and a moderate increase in the fatality loss due to collapse. The larger the difference, the shaper the drop in the slope. As for the high-seismicity scenario, Fig. 6-10 (d) gives consistently higher financial losses compared with those for the low-seismicity one. A cluster within 155 and 191 million dollars of all damage states right after the mainshock. A possible explanation is that the significantly longer waiting times to reoccupy the damaged building limit the reduction of disruption losses and the higher seismic risk adds to the increase in the fatality loss due to collapse. As a result, the differences in the cumulative losses are not obvious. An interesting finding is that the financial loss of DS-8 is lower than those of the DS-6 and DS-7. This is because that reoccupying the damaged building as soon as the safety threshold is satisfied might not be the optimal action, i.e., the increase in the fatality losses due to collapse could already exceed the reduction of disruption losses. This is further proved in the next section.

6.5.2 Financial Loss and Safety Threshold

This case seeks to use dynamic programming to obtain the optimal action by minimizing the financial losses in addition to the enforcement of the safety threshold. This is achieved by setting $R_i^s(a_i^s) = 0$ at all times and $A_i^{s,*} = \{ENR\}$ if $P_u^s \geq P_0$ and $A_i^{s,*} = \{ENR,\ RNR\}$ otherwise. The key difference with Case 1 is that a second thought considering the minimal financial losses are conducted before reoccupying the damaged building when the safety threshold is satisfied.

The optimal policies for both low- and high-seismic scenarios versus the elapsed days after the mainshock for all post-mainshock damage states are shown in Fig. 6-11 (a) and (b), respectively. Again, the optimal actions right after the mainshock are always to evacuate the building. This decision is obtained by two independent criteria, the safety threshold, and the minimal financial loss, where the former always takes control from the beginning and then hands over to the latter. As we can see, the times for evacuation due to the safety threshold in Fig. 6-11 (a-b) are identical to those in Fig. 6-10 (a-b); however, considerable additional

waiting times for reoccupancy are required for all the damage states. For example, the times of building closure are elongated by 6-38 days from DS-0 to DS-7 for the low-seismicity scenario. Moreover, the building is evacuated for the entire 200 days in Case 2 compared with 106 days in Case 1. For the high-seismicity scenario, 19-58 days are added to the total evacuation times from DS-0 to DS-5, and those are extended to the end of the 200 days for DS-6 and DS-7. Recall from Case 1, this proves that the policy considering only safety threshold is indeed not the optimal one.

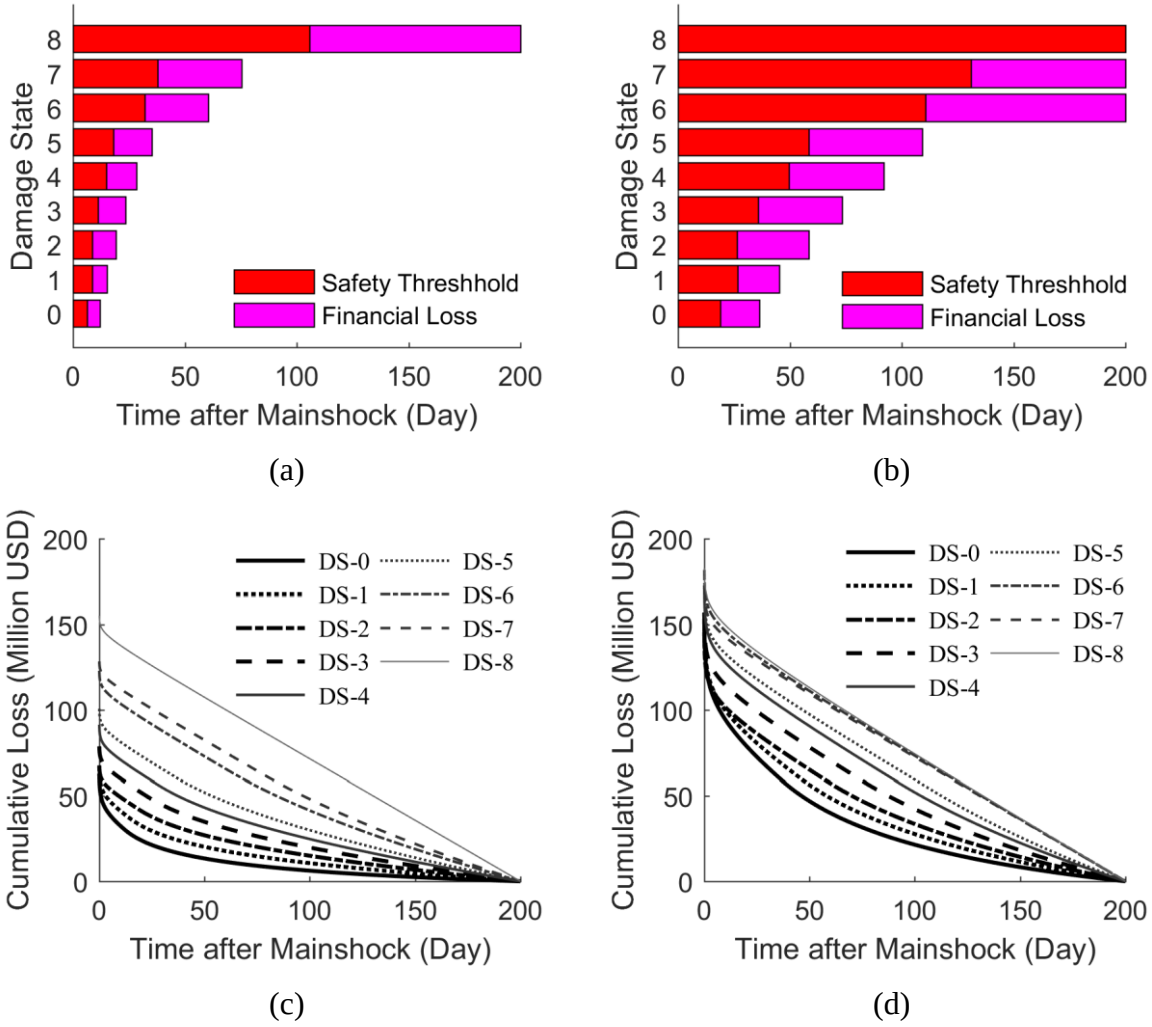

Fig. 6-11. (a-b) Optimal actions considering financial loss and safety threshold and (c-d) corresponding minimal financial losses for the low- and high-seismicity scenarios within 200 days after mainshock, respectively

Fig. 6-11 (c) and (d) show the financial losses for the low- and high-seismicity scenario given the building starts from different damage state under the mainshock, where the ascending order in terms of the damage state is observed throughout the entire time period. The financial losses for the low-seismicity scenario are in the range of 63 to 101 million dollars for DS-0 to

DS-5, and 121, 127 and 155 million dollars for the last three damage states, respectively. The financial losses for the high-seismicity scenario concentrate from 145 to 183 million dollars, which are consistently higher than the previous ones for the low-seismicity scenario. Each of the financial losses, in this case, are less than the corresponding one in Case 1. Different from the sharp drops found in Case 1, the curves tend to be smooth in this case. This might because most of the switches of the actions from evacuation to reoccupancy happen where the trade-off between the reduction in disruption losses and the increase in the fatality loss due to collapse are very small.

6.5.3 Financial Loss and Repair

Case 3 considers the financial loss and the option for repair without enforcing the safety threshold, which could be easily applied using dynamic programming by removing the constraint in Equation 6.7. All the four actions *ER, ENR, RR,* and *RNR* are always available and minimizing the financial loss is the only objective. In this case, the action of evacuation and repair are independent with each other. As the minimal financial loss serves as the control criterion in both Case 2 and Case 3, the evacuation times of the building are identical in these two cases [see Fig. 6-11 (a-b)].

As one can expect from Fig. 6-12 (a-b), the financial losses achieve the minimum across the 4 cases, where the ranges of 56-118 million dollars and 131-174 million dollars are observed with consistent ascending order in damage states for the low- and high-seismicity scenarios, respectively. The significant reduction of the financial loss benefits solely from the consideration of repairs.

No simple pattern could be used to explain the optimal repair periods for the low- and high-seismicity scenarios shown in Fig. 6-12 (c-d). No repairs are needed for the intact building in both scenarios. In Fig. 6-12 (c), the repairs start immediately after the mainshock from DS-2 to DS-7, but each has a different duration which could be as long as 160 days for DS-7 and as short as 100 days for DS-5. The repairs start 2 and 15 days after the mainshock for DS-1 and DS-8 respectively. The former continues for 142 days and the latter remains to the end of 200 days. For the high-seismicity scenario in Fig. 6-12 (d), the repair periods for DS-1 and DS-2 are postponed by roughly 20 days with similar durations. DS-3 through DS-5 have longer durations than those in the low-seismicity scenario. The repairs are delayed by 31-43 days and extended to the end of the time window for DS-6 to DS-8. The fact that the repairs do not start immediately nor continue to the end of the time window for some damage states is the nature

of the optimization. The repairs are performed by paying a constant daily cost in exchange for the potential benefits to reduce the financial losses: 1) one-time gain when building recoveries to a lower damage state, 2) continuing lower expected disruption loss, 3) lower expected financial losses of the building with lower damage state in the future and 4) less expected fatality loss as the probability of staying or transforming into higher damage states are reduced. The repair strategy could vary a lot for different damage states in the aftershock environment as a result of the time-dependent interactive relationship among these factors.

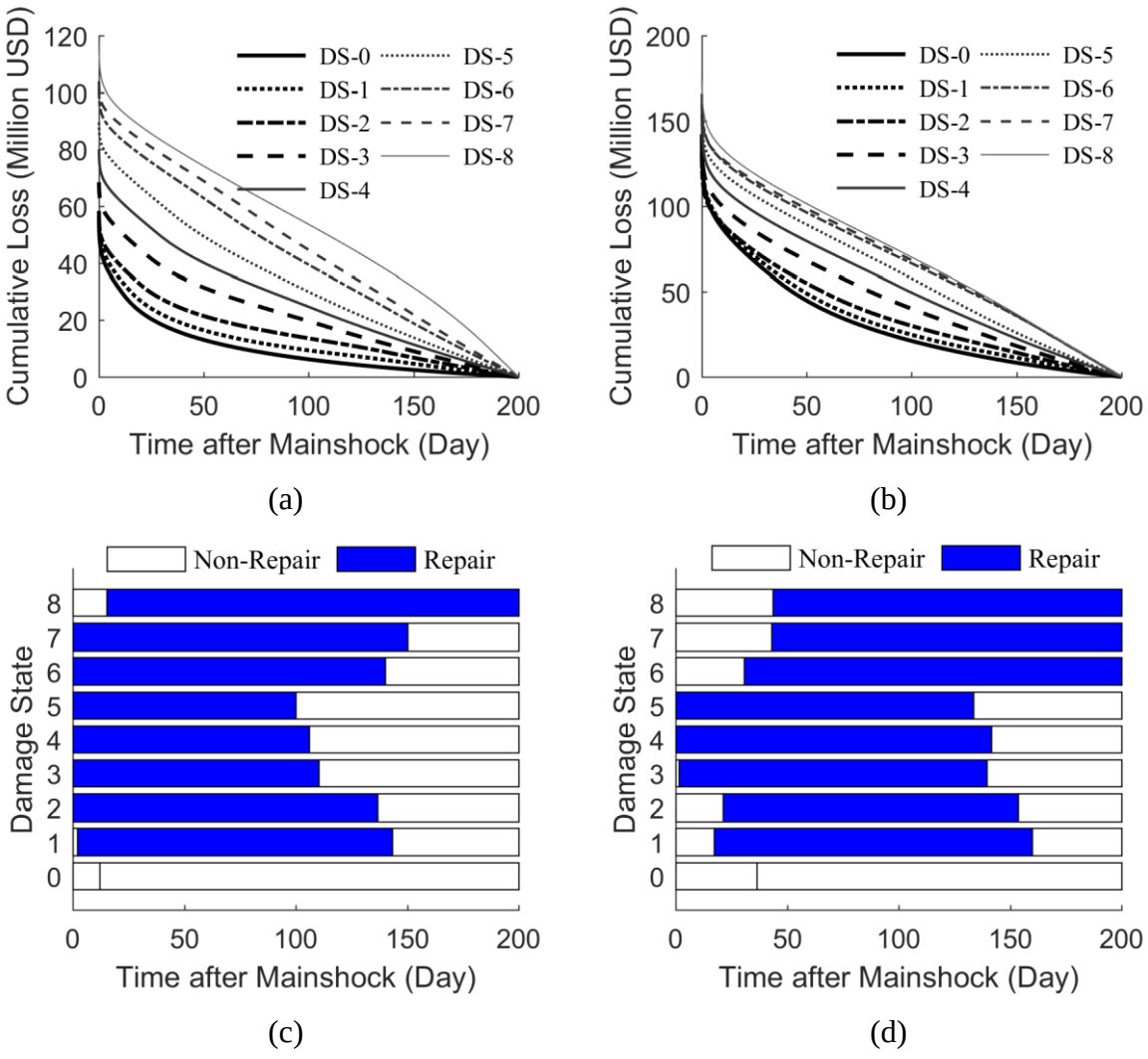

Fig. 6-12. (a-b) Minimal financial losses considering financial loss and repair and (c-d) corresponding optimal repair periods for the low- and high-seismicity scenarios within 200 days after mainshock, respectively

6.5.4 Financial Loss, Safety Threshold and Repair

Case 4 is the final case which incorporates the financial loss, safety threshold, and repair and employs the complete version of the dynamic programming. The key difference with Case 3 is that both the reoccupancy and repairs are allowed only when the safety threshold is satisfied

to guarantee the life safety of the residents as well as workers. Similarly, the evacuation times are controlled by the optimal financial loss controls over the safety threshold for all damage states and are identical to those from Case 2 and 3.

As a result of the trade-off between safety and financial losses, some increases in the optimal financial losses are found for different damage states in both the low- and high-seismicity scenarios in Fig. 6-13 (a) and (b) due to the enforced delay of repairs. The ranges of 57-144 million dollars and 135-183 million dollars are observed with consistent ascending order in damage states for both scenarios, respectively.

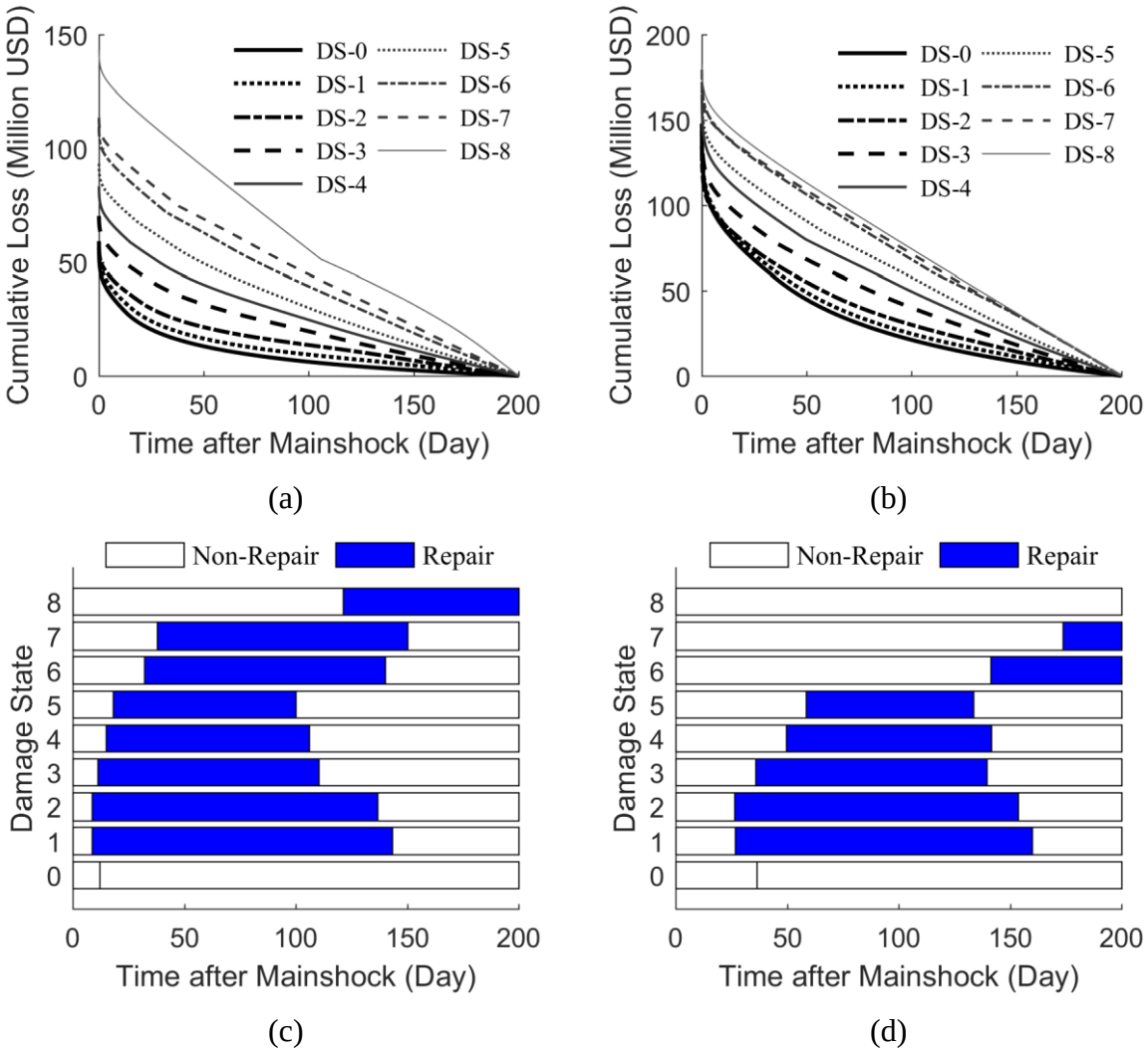

Fig. 6-13. (a-b) Minimal financial losses considering financial loss, safety threshold, and repair and (c-d) corresponding optimal repair periods for the low- and high-seismicity scenarios within 200 days after mainshock, respectively

Fig. 6-13 (c) and (d) present the optimal repair periods for Case 4. Again, no repairs are needed for the intact state. For most of the damage states, the repairs start as soon as the safety

threshold is satisfied, such as DS-1 to DS-7 for the low-seismicity scenario and DS-1 to DS-5 for the high-seismicity one. However, the repairs are postponed for a few days even after the safety threshold is satisfied for DS-8 and DS-6 to DS-7 in the low- and high-seismicity scenarios, indicating the minimal financial losses govern these times. No repairs are ever performed for DS-8 in Fig. 6-13 (d) as the building remains evacuated and controlled by the safety threshold for the entire time window. It is found that although start at different times, the repairs for the same damage state in the two cases end at a similar time. This might because it is not economically optimal to pay constant repair cost when the aftershock seismic risk drops significantly in a certain period after the mainshock, which is true in both cases.

6.6 Sensitivity Analysis

It is important to understand and quantify the impact of key parameters on the optimal policy and the minimal financial losses obtained from the previous analyses. Independent sensitivity analyses are conducted in this section for five parameters: time window, safety threshold, fatality loss, disruption loss, and repair cost. Only the low-seismicity scenario is considered in this chapter. Instead, two damage states, DS-2 (PSDR=1.0%) and DS-6 (PSDR=3.0%), are used for comparison.

6.6.1 Time Window

As shown in Fig. 6-14 (a), the financial losses for all damage states increase monotonically as the time window rises from 20 days to 300 days. As expected, the curves of the DS-0 and DS-8 serve as the lower and higher bounds. The curves cluster when the time window is small and spread out when it gets large. This is because more potential damage state transition of the damaged building is considered, leading to more customized optimal policies used for different damage states in a longer period. While the ascending order in terms of the damage state is nicely held, a cross of DS-6 and DS-7 is found near the time window of 125 days. This might because the evacuation time required by the safety threshold exceeds that by the minimizing financial losses for DS-7 within a certain time window. Fig. 6-14 (b) depicts the optimal waiting time for reoccupancy of different damage states as time window changes. For any damage state, this time is certainly bounded by the time window, and then decided from the safety threshold and minimal financial loss. The latter takes control for the damage state below DS-3 (inclusively) and DS-7 (inclusively) when the time window is taken as 20 days and 80 days respectively. For DS-8, the time window controls up to 260 days.

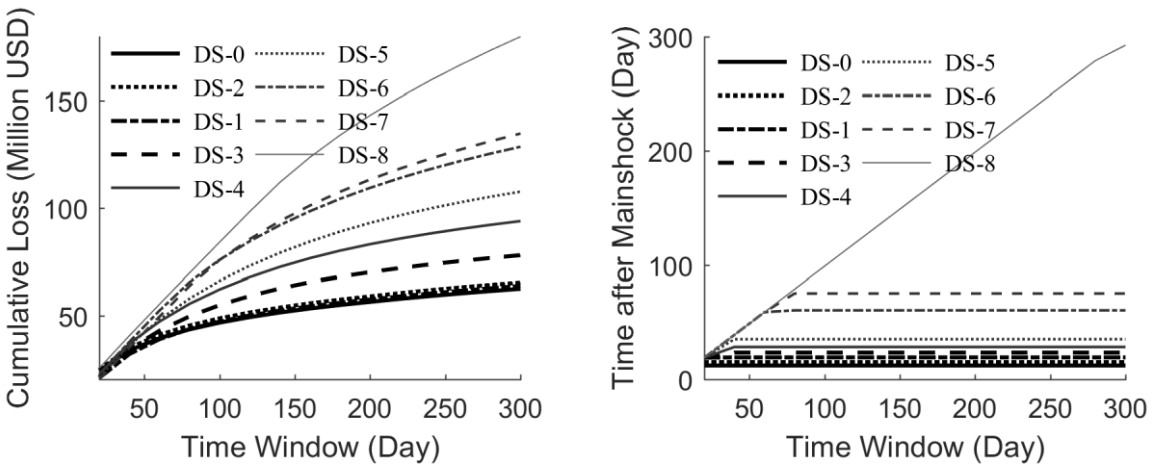

(a) (b)

Fig. 6-14. (a) Minimal financial losses and (b) optimal waiting times for reoccupancy in different time windows

The variation of the start and end of the repair process during aftershock environment is shown for post-mainshock DS-2 and DS-6 in Fig. 6-14 (c) and (d), respectively. As we can see, the safety threshold and minimal financial loss always control rather than the time window. For DS-2, no repairs are performed when the time window is less than 40 days, and the optimal repairs start consistently at 10 days after the mainshock but with longer durations as the time window increase beyond 60 days. The fact that the repairs do not continue to the end of the time window might because the aftershock seismic risk drops significantly in a certain period after the mainshock and it is not economically optimal to pay constant repair cost after that. Similar results are found for DS-6 but with longer waiting time before repairs and shorter duration at each time step. The longer waiting time is because the higher aftershock seismic risk is higher for DS-6 and take more time to get below the safety threshold needed to start the repairs. Recall from Table 6-9, for a given target lower damage state, the higher an initial damage state, the lower the transition probability. Moreover, for a given initial damage state, the constant transition probability into a lower damage state drops fast as the target damage state goes lower. For example, the transition probability is 6.15×10^{-4} from DS-6 to DS-5 while is only 1.29×10^{-5} from DS-6 to DS-0. These indicate that performing the repairs with the same constant cost, a lower damage state is more economically beneficial compared with a higher damage state in terms of the expected financial gain defined in Equation 6.6. The benefit of the repair for higher damage state is more to reduce the probability of the collapse of the damaged building such that the fatality loss is limited rather than to recover the building to lower damage states. As a result, even though start later, the repairs for a higher damage state

(DS-6 in this case) could end earlier as the collapse risk drops significantly after a certain period.

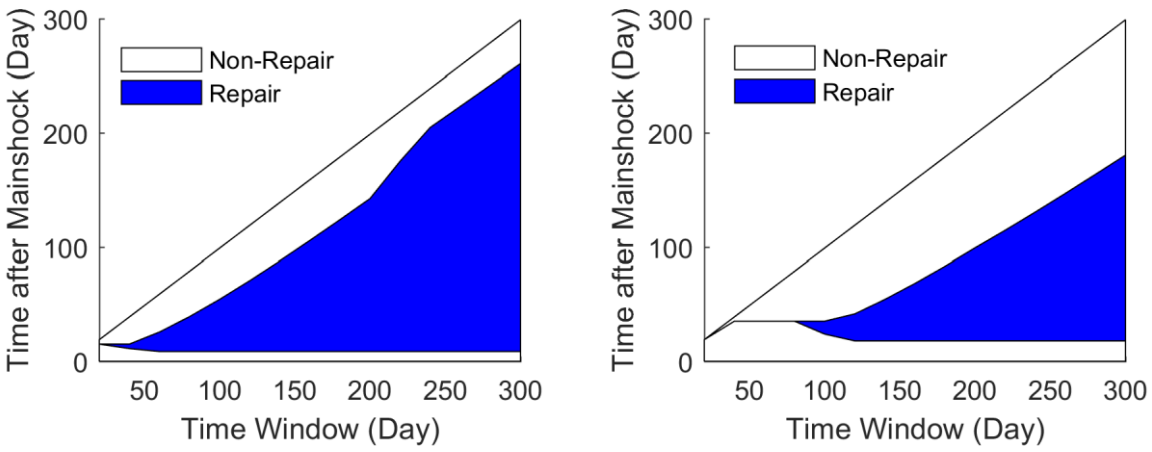

Fig. 6-15. Optimal repair periods for (a) DS-2 and (c-d) DS-6 in different time windows

6.6.2 Safety Threshold

The safety threshold range defined as the daily transition rate into the unsafe damage states is increased from 5.5×10^{-7} to 5.5×10^{-4} for the sensitivity analyses, which correspond to 0.5 and 500 times the daily exceedance rate of the MCE level.

Three phases of the safety threshold could be divided from Fig. 6-16 (a). In Phase 1, the safety threshold governs the financial losses for all damage states when it is small enough such that the building remains evacuated throughout the entire time window. This is marked by either a linearly sharp descending line (DS-0 to DS-7) or a horizontal line (DS-8). In Phase 2, as the safety threshold increases, it gradually releases the control of evacuation to the minimal financial loss from the lower damage state to the higher ones. The switching point is around 8.2×10^{-5}. However, the safety threshold in this phase still governs the start of the repairs after the mainshock, as depicted by the gradually descending lines in Fig. 6-16 (a). In Phase 3, the safety threshold is so large such that it never governs any decision at any time, thus the minimal financial loss each damage state simply remains the same. It is noted that curves of DS-6 to DS-8 are approaching but have not yet reached phase 3 at 5.5×10^{-4}. Similar phases are observed in Fig. 6-16 (b) for the waiting times for reoccupancy of different damage states, but Phase 2 and Phase 3 are actually merged into a single phase as the optimal evacuation and repair times are independent with each other.

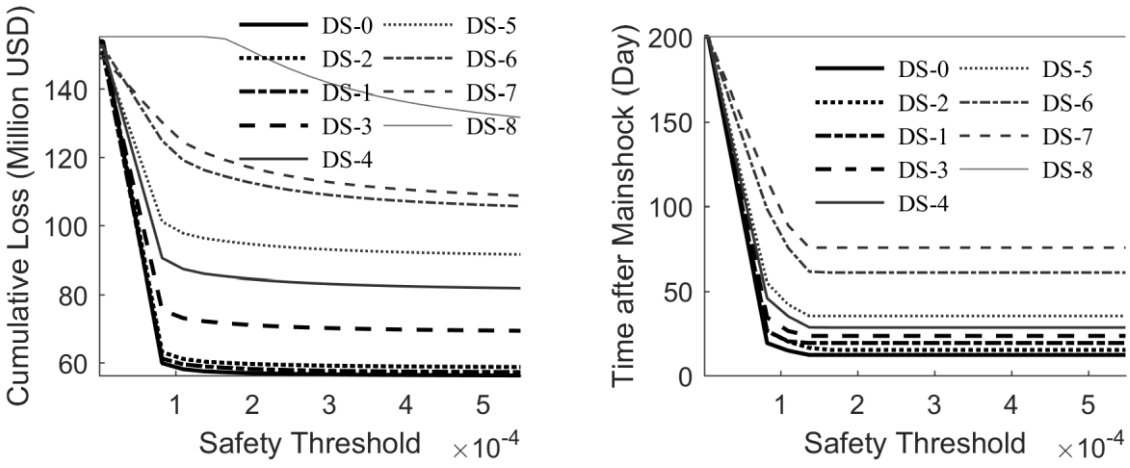

(a) (b)

Fig. 6-16. (a) Minimal financial losses and (b) optimal waiting times for reoccupancy with different safety threshold

Fig. 6-17 (a) and (b) give examples of the optimal repair periods as the safety threshold varies for the building in DS-2 and DS-6 after the mainshock, respectively. No repairs are performed when the safety threshold is below 8.2×10^{-5}, which corresponds to the end of Phase 1 defined earlier. As the safety threshold increases beyond this point within the considered range, the repairs start from 55 to 10 days and from 26 to 5 days for DS-2 and DS-6, but consistent end times of 100 days and 143 days are found for them, respectively.

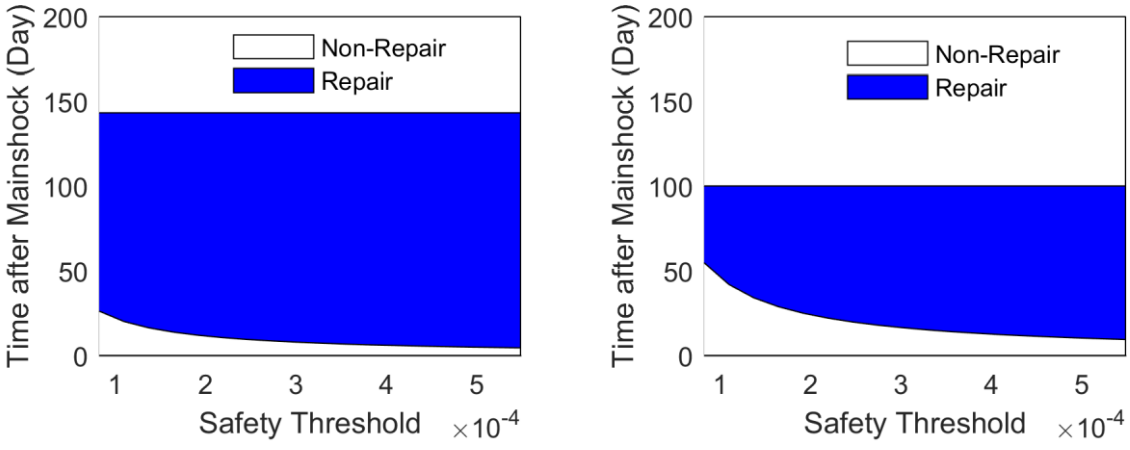

(a) (b)

Fig. 6-17. Optimal repair periods for (a) DS-2 and (c-d) DS-6 with different safety threshold

6.6.3 Fatality Loss

The actions and corresponding financial losses are reoptimized for the fatality loss ranging from 1 to 20 million dollars per person. Fig. 6-18 (a) shows the curves of the DS-0 and DS-8

serve as the lower and higher bounds, and each curve increases monotonically with decreasing slope. Larger changes of minimal financial losses are observed for the lower damage states. For example, the minimal financial loss for DS-0 increases from 37 to 98 million dollars while it only rises from 133 to 154 million dollars for DS-8. This is because the severely damaged building is evacuated for the most part of the time window if not entire, so the fatality loss caused by collapse would not be significantly impacted. On the other hand, the trade-off between continuing disruption loss and the fatality loss are kept evaluation at each time step for slightly damaged building. Fig. 6-18 (b) depicts that the waiting time for reoccupancy of each damage state remains constant when the fatality loss per person is below 2 million dollars per person, meaning only the safety threshold is controlling. After that, it increases almost linearly until reaching the cap of 200 days when the building is simply closed for the entire time window due to excessive fatality loss caused by a potential collapse. The higher a damage state, the sooner it reaches the cap due to its higher probability of collapse given the same aftershock hazard.

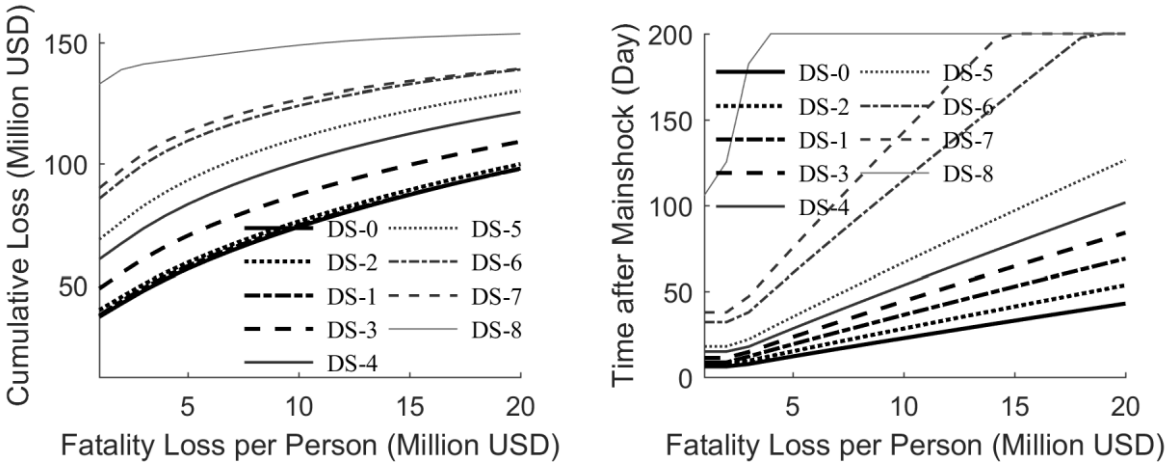

(a) (b)

Fig. 6-18. (a) Minimal financial losses and (b) optimal waiting times for reoccupancy with different fatality costs

In Fig. 6-19 (a) and (b) show the optimal repair periods as the fatality loss varies for the building in DS-2 and DS-6 after the mainshock, respectively. The constant start times are controlled by the safety threshold, but long durations from 125 to 153 days and from 53 to 123 days are assigned as the fatality loss increases for the two damage states respectively.

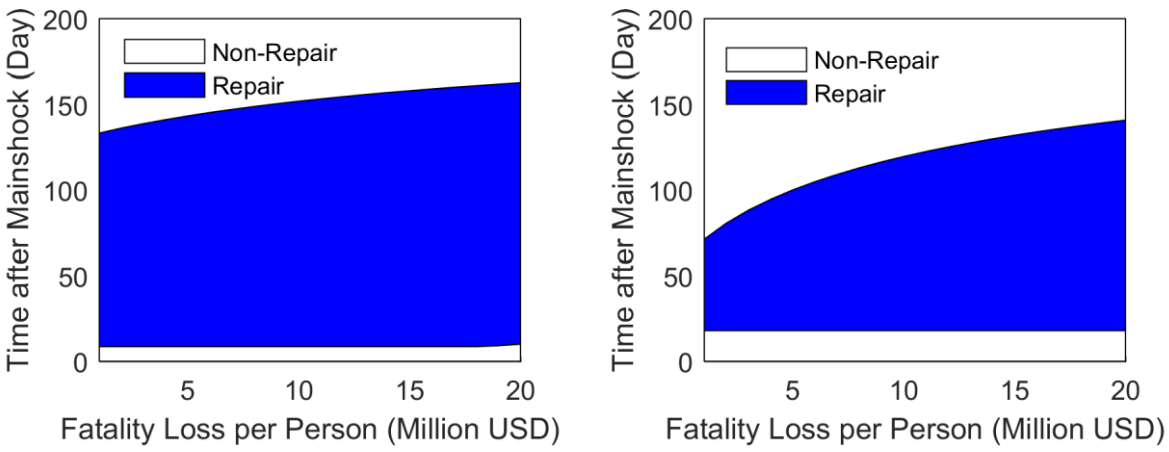

(a) (b)

Fig. 6-19. Optimal repair periods for (a) DS-2 and (c-d) DS-6 with different fatality costs

6.6.4 Disruption Loss

The influence of changing the cap of disruption loss from 0.1 to 2 million dollars per day on the optimal financial loss is explored in Fig. 6-20 (a). It is noted that the cap corresponds to the highest damage state where the damaged building collapses. The state-dependent disruption loss for any other damage state is computed according to the proportional relationships defined in Section 6.3.3. DS-0 and DS-8 serve as the lower and higher bounds. Each curve increases monotonically with slightly decreasing slope when the disruption loss is below 0.5 million dollars per day. After that, almost linear increases are observed. Significantly more losses are added to the higher damage states as longer evacuation times are expected.

Fig. 6-20 (b) shows how the increase of the cap of disruption loss shortens the waiting time for reoccupancy in order to get minimal financial loss. As mentioned in the previous section, this is also the result of the trade-off optimization between the disruption loss caused by building evacuation and the fatality loss due to collapse. Sharps drops in the waiting times for reoccupancy are found for DS-0 to DS-7 when the cap of disruption loss is less than 1 million dollars per day, especially below 0.5 million dollars per day. No obvious changes happen after 1.5 million dollars per day as the evacuation is controlled by the safety threshold, which is independent of the disruption loss. A different curve is observed for DS-8, which is initially evacuated for the entire 200 days but starts to be reoccupied for some time in the late stage of the time window when the state-dependent disruption loss goes over 0.48 million dollars per day.

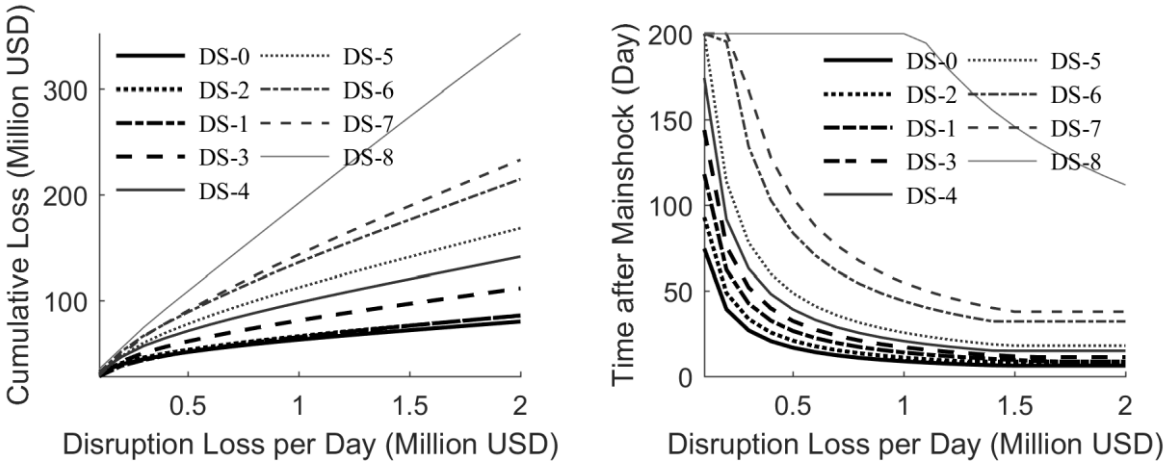

(a) (b)

Fig. 6-20. (a) Minimal financial losses and (b) optimal waiting times for reoccupancy with different disruption losses

Fig. 6-21 (a) and (b) show that the repair durations increase from 61 to 169 and from 48 to 137 for DS-2 and DS-6 respectively as the state-dependent disruption loss rises from 0.01 to 0.2 and from 0.03 to 0.6 million dollars per day. The repairs start immediately at Day 18 when the safety threshold is satisfied for DS-6 but slightly delay for the DS-2 when the disruption loss is below 0.02 million dollars per day.

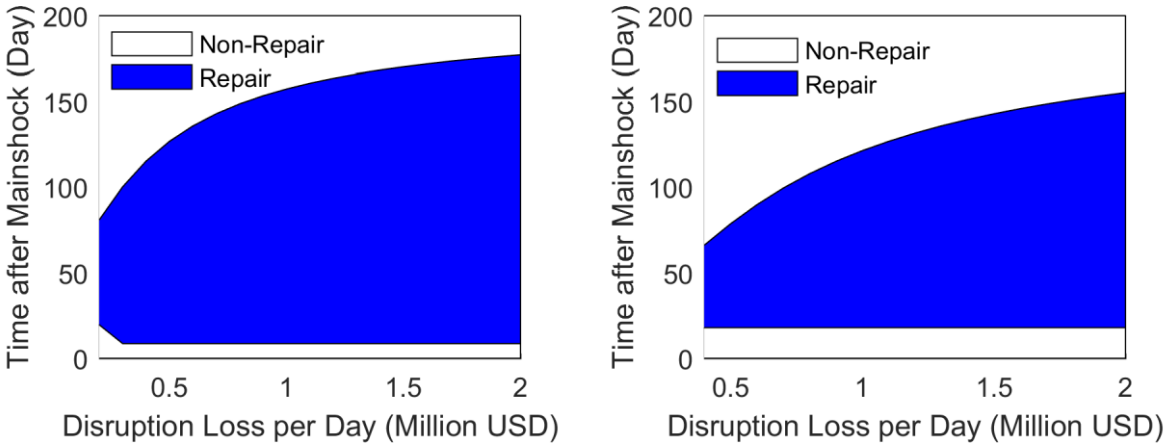

(a) (b)

Fig. 6-21. Optimal repair periods for (a) DS-2 and (c-d) DS-6 with different disruption losses

6.6.5 Repair Cost

The repair cost varying from 0.02 and 0.6 million dollars per day is used for the sensitivity analysis. As shown in Fig. 6-22 (a), the minimal financial loss of each damage state increases until reaching a plateau when the repair cost is so high such that it is never performed for the

damaged building. For example, the repairs could save up to 26 and 23 million dollars for the building with DS-2 and DS-6 right after the mainshock; however, no gains are observed when the repair cost exceeds 0.45 and 0.55 million dollars per day for the two damage states. Fig. 6-22 (b) confirms the fact that the change of repair cost would not influence the optimal waiting times for reoccupancy in all cases, as is discussed earlier.

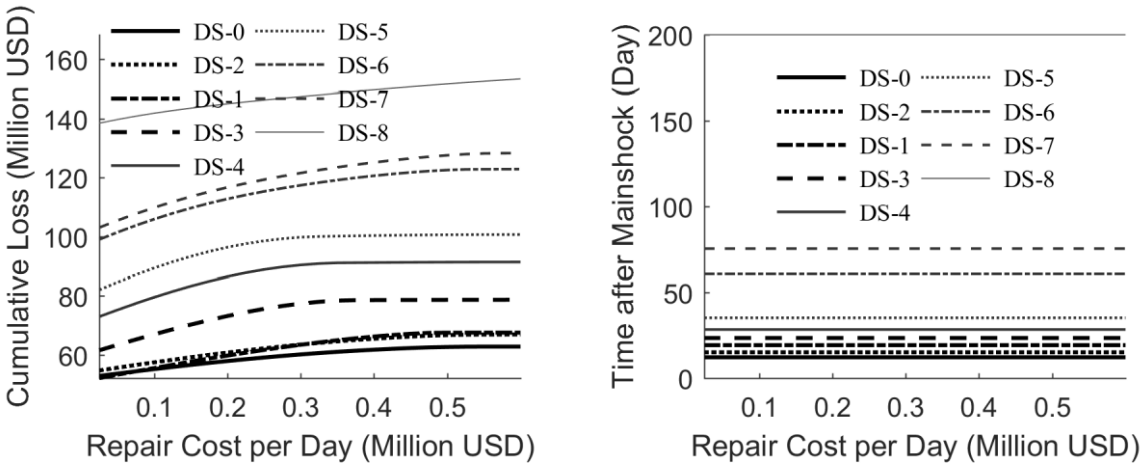

(a) (b)

Fig. 6-22. (a) Minimal financial losses and (b) optimal waiting times for reoccupancy with different repair costs

Very similar behaviors are observed for the repair periods of DS-2 and DS-6 in Fig. 6-23 (a) and (b). The duration reaches the maximum when the repair cost is the lowest, and keep decreasing as the repair cost goes up, until a point that no repairs are performed. The upper bound for possible repairs is 0.53 and 0.32 million dollars per day for DS-2 and DS-6, respectively.

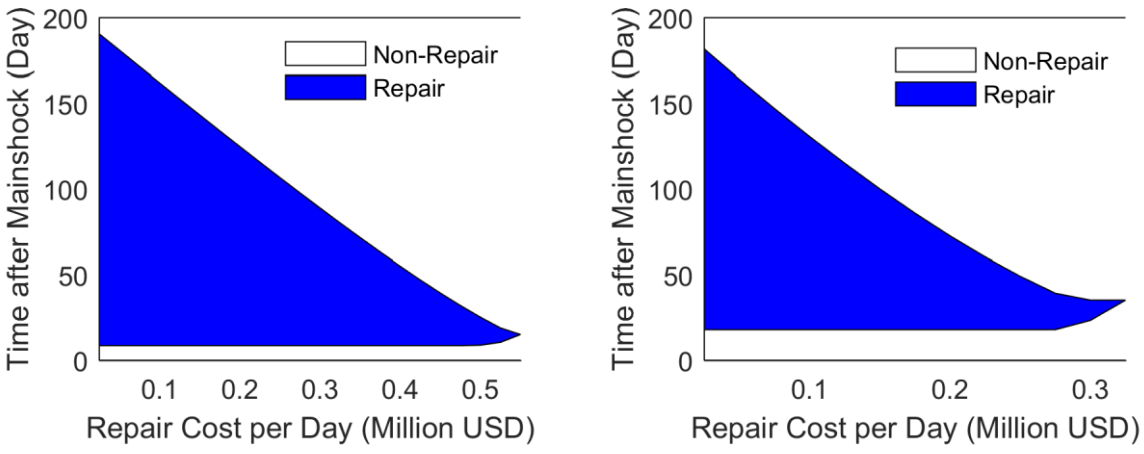

(a) (b)

Fig. 6-23. Optimal repair periods for (a) DS-2 and (c-d) DS-6 with different repair costs

6.7 Conclusions

This chapter focuses on the optimal decision-making in the aftershock environment by integrating the aftershock hazard, the residual structural capacity of damaged tall buildings, and the expected total financial loss into a time-dependent probabilistic framework based on a discrete nonstationary Markov Process. The expected total financial loss includes various sources from structural and nonstructural component damages, fatality due to collapse, disruption of residence and business as well as potential repair cost. It is defined as the expected cumulative loss within a certain time window of interest and obtained by summing up the discounted values of all the potential losses in the future. The objective is to minimize the expected financial loss and ensure life safety at the same time by the additional constraint defined as the transition probability into unsafety damage states. The transition from a higher damage state to a lower one, which is previously excluded in Chapter 5, is also considered in this chapter to account for the repairs. Two sets of actions after the mainshock are considered at any time point: whether to evacuate the building and when to reoccupy the building if it is previously evacuated; whether to repair the building and when to stop if the building had been retrofitted to a satisfactory state. Dynamic programming is then performed to find the optimal actions throughout the entire time period of interest. Sensitivity analyses are finally carried out to quantify the impact of the key parameters on the decision-making, including time window, safety threshold, fatality loss, disruption loss, and repair cost.

It is assumed that the damaged tall building is forced to be evacuated and no repairs are allowed when the seismic risk is higher than the safety threshold, and all the actions are available to minimize the financial loss otherwise. The decision of evacuation/reoccupancy and repair/non-repair are always treated independently. Two scenarios are employed for comparison using the time-dependent aftershock hazards from a low- and high-seismicity fault, respectively. Four difference cases are explored for the dynamic programming by considering: 1) the safety threshold only, 2) the financial loss and safety threshold, 3) the financial loss and repair and 4) the financial loss, safety threshold, and repair.

Case 1 serves as the baseline where the building is occupied as soon as the safety threshold is satisfied. The evacuation time and financial loss increases as the damage states get higher. For some severe damage states and high-seismicity scenarios, the damaged building could remain closed for the entire time window of interest. Some sharp drops on the financial loss curves are observed at the times corresponding to the reoccupancy as a result of the difference

between the significant reduction in disruption losses and a moderate increase in the fatality loss due to collapse.

Case 2 shows that given the key parameters used, the control criterion for the evacuation time is always the minimal financial loss rather than the safety threshold, meaning additional waiting time is needed to reoccupy the damaged building to further reduce the fatality loss for the rare event of a collapse. Relatively smoother curves are found in this case, which might because most of the switches of the actions from evacuation to reoccupancy happen where the trade-off between the reduction in disruption losses and increase in the fatality loss due to collapse are very small.

Case 3 obtained the minimal financial losses for all damage states across all cases as the safety threshold is removed such that the repairs could be performed as early as needed. The fact that the repairs do not start immediately nor continue to the end of the time window for some damage states is the nature of the optimization. The repairs are performed by paying a constant daily cost in exchange for the potential benefits to reduce the financial losses: 1) one-time gain when building recoveries to a lower damage state, 2) continuing lower expected disruption loss, 3) lower expected financial losses of the building with lower damage state in the future and 4) less expected fatality loss as the probability of staying or transforming into higher damage states are reduced. The repair strategy could vary a lot for different damage states in the aftershock environment as a result of the time-dependent interactive relationship among these factors.

Case 4 adds the safety threshold to Case3 and is the full application of dynamic programming considering all aspects. Most of the start times of repairs are postponed compared to Case to ensure the life safety of the worker; however, the repairs for the same damage state in the two cases end at the similar time. The is because it is not economically optimal to pay constant repair cost when the aftershock seismic risk drops significantly in a certain period after the mainshock, which is true in both cases.

Sensitivity analyses show that all the five key parameters have considerable impacts on the optimal actions as well as the minimal financial losses of the decision-making in the aftershock environment. A positive correlation is found between the minimal financial loss and all key parameters except the safety threshold, the increase of which releases the constraint for the optimization. The safety threshold, fatality loss, and disruption loss have significant impacts on the evacuation times or the waiting times for reoccupancy, while the time window only

serves as a valid higher bound and the repair cost has no influence on it. The duration of the repair increases when all the parameters rise except for the repair cost. However, this is generally achieved by starting the repairs earlier as the safety threshold increases and ending the repairs later when the time window, fatality loss, and disruption loss gets larger.

The proposed optimal decision-making framework could be used at any time in the aftershock environment to provide solid support to the for the stakeholders such as residents, earthquake engineers, insurance companies as well as policymakers. However, it is important to note that the results in this study are only valid for the time window considered, and the seismic hazard includes only the aftershock hazard following the already occurred mainshock without considering the mainshock hazard in the future. For example, the optimal policy in this study might end with stopping the repairs when aftershock seismic risk drops significantly and leaving the building with considerable damages; however, it could be more beneficial to keep repairing the building to the full recovery state when considering any future mainshock hazard.

CHAPTER 7: Conclusion, Limitations, and Future Work

7.1 Overview

The primary objective of this study is to present a series of frameworks for the post-earthquake performance assessment and optimal decision-making of tall buildings. More specifically, a machine learning framework to assess the structural safety is first proposed and applied to a low-rise frame building. The methodology is then extended to tall buildings with substantial modifications including the adoption of specialized techniques to handle the high-dimension feature space. Seismic risk assessment is then carried out for the tall building by comparing the time-dependent probability of exceeding various response demand limits over a pre-defined period using mainshock-only and mainshock-aftershock hazards. The risk-based consistency of the EDP-based limit state acceptance criteria is also examined. Finally, a framework to support optimal decision-making following the mainshock is formulated to minimize the expected financial losses and, at the same time, ensure life safety. The proposed prediction model, risk assessment methodology and optimal decision-making strategy provide critical insights into the seismic performance of mainshock-damaged tall buildings and useful guidance to occupants, structural engineers, insurance companies as well as policymakers.

7.2 Findings

The key findings from chapters 2, 4, 5 and 6 are presented in this section. Recall that Chapter 3 presented the structural modeling, probabilistic seismic hazard analysis and ground motion selection for tall buildings with core walls and special moment frames, which laid the foundation for the analyses in Chapters 4-6.

7.2.1 Chapter 2: Machine Learning Framework for Assessing Post-Earthquake Structural Safety

Previously developed post-earthquake structural evaluation methods have based the safety state criteria on the exceedance of pre-defined response demand levels or damage state ratios within individual structural component groups. In contrast to these prior approaches, the outcome of the proposed framework consists of classification trees, each comprising of a high-dimension space of response and damage patterns partitioned into multiple subspaces. Given an arbitrarily observed pattern for a damaged structure, each tree is intelligently searched to find the matching subspace, which will serve as the basis for classifying the safety state of the

structure. The result is a discrete probability distribution of the structural safety state, which serves as an indicator of the confidence of the prediction.

The application of the proposed methodology to a 4-story reinforced concrete special moment frame building showed that the predictive models trained using machine learning algorithms can provide predictions with high performance in terms of accuracy, sensitivity, and specificity. Relatively high sensitivity is also observed in the prediction models developed for the case study, which is critical for reducing the rate of high-risk erroneous predictions i.e. model predicts safe when the building is unsafe. The proposed framework could be used to conduct rapid probabilistic assessments of whether a damaged building is safe to reoccupy following an earthquake. Additionally, the trees generated by the machine learning algorithms could be used to prioritize field inspections following an earthquake. Moreover, the probabilistic safety state predictions could be used in community resilience evaluations and individual building life-cycle performance assessment and optimization.

7.2.2 Chapter 4: Pattern Recognition Approach to Assess the Residual Structural Capacity of Damaged Tall Buildings

Pattern recognition models are constructed for the different EDP groups built on a significantly smaller (compared to the raw data) feature space. The global EDPs are observed to be strong indicators of the reduction in structural capacity possibly because they are directly associated with the CP performance metric. However, only the FBR, CBR and RTS give informative predictions and a weak relationship was found between the FCR and CCS and κ_{CP}. For FCR, this is likely due to the strong-column-weak-beam principle used to design the reinforced concrete frames, which seeks to limit plastic rotation demands in the frame columns. As for CCS, it is possible that most of the compressive strains in the shear wall concrete come from gravity loads with only small changes resulting from the lateral forces induced by mainshocks. While it is useful for feature selection, the predictive performance of LASSO is limited because of the highly nonlinear relationship between κ_{CP} and features. SVM with a radial basis function kernel can significantly reduce the root mean square errors using the selected features. Moreover, the reserved features can be used when the selected ones are unavailable, within minimal loss in the predictive accuracy.

The proposed methodology provides a rapid link between the structural responses measured during an earthquake to the building performance in subsequent events. This information can be used to optimize the placement of sensors used to measure such responses

and guide engineers performing post-earthquake inspections and assessments of residual structural capacity, which can be updated in real-time as structural response data becomes available.

7.2.3 Chapter 5: Seismic Risk Assessment of Tall Buildings Considering Mainshock and Aftershock Hazard

In this study, an aftershock seismic risk assessment is first conducted, which considers the case where the mainshock has occurred and the immediate post-mainshock building-level damage state is known. Except for CBR, a sharp increase and plateauing of the exceedance probability for the EDP limits was observed in the first 3 days when conditioned on an immediate post-mainshock PSDR = 0.5%. For the same immediate post-mainshock PSDR, the probability of exceeding the CBR limit is consistently high over the 30-day period. This type of assessment could inform the timing, cost and duration of repairs after a mainshock has occurred. For example, the results from this study showed that delaying repairs for approximately the first week after the mainshock could avoid having to perform redundant repair work caused by subsequent aftershock damage.

The mainshock-aftershock risk, which accounts for the uncertainty in the intensity and damage caused by both the mainshock and aftershock, is performed and compared with the case where only mainshock hazard is considered. The probability of exceeding each EDP limit over the 50-year life of the building is computed. When a 2% probability of exceedance in 50 years is used as the risk threshold for life safety, most of the associated response demands (except for CBR) are within the collapse prevention performance criteria when only mainshock hazard is considered. However, when the mainshock-aftershock hazard is considered, the demand levels for RSDR, FBR and CBR are much higher than the those corresponding to collapse prevention performance. Even though the limits set by TBI and LATBSDC are targeted towards collapse prevention performance, the implied 50-year exceedance probabilities were found to be non-uniform across the various EDPs for the mainshock only and mainshock-aftershock case, differing by a factor of 30 in the extreme case. This finding highlights the need to develop risk-consistent response demand limits when the acceptance criteria are targeted towards a single performance level.

7.2.4 Chapter 6: Optimal Decision-Making for Tall Buildings in the Aftershock Environment

In this study, a framework is developed to support optimal decision-making related to tall buildings in the post-earthquake environment. Dynamic programming is utilized under the following four conditions: 1) only a pre-defined safety threshold is considered, 2) financial losses and a pre-defined safety threshold are considered, 3) financial losses and repairs are considered and 4) financial losses, a pre-defined safety threshold, and repairs are considered.

The evacuation time and financial loss increases as the damage states get higher. For some severe damage states and high-seismicity scenarios, the damaged building could remain closed for the entire time window of interest. Sharp decreases in financial losses are observed at the times corresponding to reoccupancy. This is because of the difference between the significant reduction in disruption losses and a moderate increase in the fatality loss due to collapse. For the adopted parameters, the controlling criterion for the evacuation time is always minimizing the financial losses rather than the safety threshold. In other words, additional waiting time is needed to reoccupy the damaged building to further reduce the fatality loss for the rare event of a collapse. The fact that the repair does not start immediately nor continue to the end of the time window for some damage states is an artifact in the optimization. When repairs are performed, there is a constant daily cost that is offset by the following: 1) a one-time gain when building recovers to a lower damage state, 2) a continuous reduction in the expected disruption losses, 3) lower expected financial losses when, in the future, the building is in a lower damage state and 4) less expected fatality loss as the probability of staying in the current state or transitioning to a higher damage states is reduced. Because of the time-dependent interactive relationships among these factors, the repair strategy could vary significantly.

All five key parameters have considerable impacts on the optimal actions as well as the decision-based minimal financial losses in the aftershock environment. A positive correlation is found between the minimum financial loss and all key parameters except the safety threshold, which, when increased, relieves some of the optimization constraints. The safety threshold, fatality loss, and disruption loss have significant impacts on the evacuation times or the waiting times for reoccupancy. The time window only serves as a valid higher bound and the repair cost has no influence on it. There is a positive correlation between the duration of the repairs and all parameters except for the repair cost. However, an increase in repair duration is generally achieved by starting the repair earlier as the safety threshold increases and ending the

repair later when the time window, fatality loss, and disruption loss gets larger. It is important to note that the results in this study are only valid for the considered time window. Moreover, only aftershock hazard is considered because the assumption is that the mainshock has occurred and the additional future hazard from additional mainshocks is not considered. For example, the optimal policy in this study might end with stopping the repair when aftershock seismic risk drops significantly and leaving the building with considerable damage. However, it could be more beneficial to continue the repairs so that the building is restored to full functionality when considering any future mainshock hazard.

7.3 Limitations and future work

The classification of the safe and unsafe damage states in Chapter 2 and the residual capacity evaluation in Chapter 4 is entirely dependent on the statistics from the simulations of the available seismic hazard, ground motion data, and structural design, etc. There could be some bias that undermines the performance. It could be useful to incorporate expert opinions from earthquake engineering researchers and engineers into the predictions of the machine learning models, for example, following a Bayesian approach.

Although building-level damage states are used, the calibration simply using PSDR may not provide accurate estimation for system-level performance. A potentially better option would be using the residual structural capacity proposed in the current study. For example, constructing the Markov process in Chapter 5 and optimizing decisions in Chapter 6 based on building-level damage states grouped by certain intervals of residual structural capacity rather than PSDR.

The current work can map the damage or response patterns to safe/unsafe state or residual structural capacity, but no result is provided on how the relationship would change if one or more key structural components are repaired. With this piece of information, we can obtain an optimal repair sequence for the damaged building such that it can recover as soon as possible. Moreover, this can be then combined with the decision-making framework in Chapter 6 to get the optimal actions and repair sequences as time elapses after the mainshock.

The variation of building structures is not addressed in the current study. To generalize the feasibility of the proposed frameworks and methodologies, additional evaluations are needed using a set of buildings with different structural configurations and lateral force resisting systems.

Finally, the analyses used in the current study only incorporated record-to-record uncertainty. Prior studies have shown that modeling uncertainty can affect both the dispersion and median values of limit-state-based performance metrics. Therefore, for implementation purposes, the effect of modeling uncertainty should be incorporated in future work.

References

[1] American Society of Civil Engineers. Minimum Design Loads for Buildings and Other Structures. Reston, VA: American Society of Civil Engineers; 2010.

[2] International Code Council, Inc. 2015 International Building Code. Birmingham, AL: International Code Council, Inc.; 2014.

[3] Luco N, Ellingwood BR, Hamburger RO, Hooper JD, Kimball JK, Kircher C a. Risk-Targeted versus Current Seismic Design Maps for the Conterminous United States. Struct Eng Assoc Calif 2007 Conv Proc 2007:1–13.

[4] SEAOC. Vision 2000, Performance based seismic engineering of buildings. Sacramento, CA: Structural Engineers Association of California; 1995.

[5] ATC. 40, Seismic evaluation and retrofit of concrete buildings. Redwood, CA: Applied Technology Council; 1996.

[6] FEMA. 273/274, NEHRP guidelines for the seismic rehabilitation of buildings. Washington, DC: Federal Emergency Management Agency; 1996.

[7] Ghobarah A. Performance-based design in earthquake engineering : state of development 2001;23:878–84.

[8] Moehle J, Deierlein GG. A framework methodology for performance-based earthquake engineering. Proc 13 Th World Conf Earthq Eng 2004:3812–4. doi:10.1061/9780784412121.173.

[9] Comerio, M, Elwood, K, Berkowitz R. The M 6.3 Christchurch, New Zealand, Earthquake of February 22, 2011. Oakland, California, USA: 2011.

[10] Parker M, Steenkamp D. The economic impact of the Canterbury earthquakes major earthquakes. Reserv Bank New Zeal Bull 2012;75:13–25.

[11] Burton H V., Deierlein G, Lallemant D, Lin T. Framework for Incorporating Probabilistic Building Performance in the Assessment of Community Seismic Resilience. J Struct Eng 2016;142:C4015007. doi:10.1061/(ASCE)ST.1943-541X.0001321.

[12] FEMA. Seismic Performance Assessment of Buildings Volume 1 – Methodology. Washington, DC: Federal Emergency Management Agency; 2012.

[13] FEMA. Seismic Performance Assessment of Buildings Volume 2 – Implementation Guide. Washington, DC: Federal Emergency Management Agency; 2012.

[14] Cornell CA, Krawinkler H. Progress and Challenges in Seismic Performance Assessment 2000;3:1–4.

[15] Deierlein GG, Krawinkler H, Cornell CA. A framework for performance-based earthquake engineering. Pacific Conf Earthq Eng 2003;273:140–8. doi:10.1061/9780784412121.173.

[16] Porter KA, Kiremidjian AS, LeGrue JS. Assembly-based vulnerability of buildings and its use in performance evaluation. Earthq Spectra 2001;17:291–312. doi:10.1193/1.1586176.

[17] Porter KA. An Overview of PEER's Performance-Based Earthquake Engineering Methodology. 9th Int Conf Appl Stat Probab Civ Eng 2003;273:973–80.

[18] Cimellaro GP, Reinhorn AM, Bruneau M. Framework for analytical quantification of disaster resilience. Eng Struct 2010;32:3639–49. doi:10.1016/j.engstruct.2010.08.008.

[19] Cimellaro GP, Reinhorn AM, Bruneau M. Performance-based metamodel for healthcare facilities. Earthq Eng Struct Dyn 2011;40:1197–217. doi:10.1002/eqe.1084.

[20] Iervolino I, Giorgio M. Stochastic Modeling of Recovery from Seismic Shocks 2015:1–9.

[21] Fereshtehnejad E, Shafieezadeh A. Multiple hazard incidents lifecycle cost assessment of structural systems considering state-dependent repair times and fragility curves. Earthq Eng Struct Dyn 2016. doi:10.1002/eqe.2764.

[22] Applied Technology Council. ATC-20: Procedures for post-earthquake building safety evaluation procedures. Redwood, CA: 1995.

[23] Applied Technology Council. ATC-20-2: Addendum to the ATC-20 post-earthquake building safety evaluation procedures. Redwood, CA: 1995.

[24] Robertson I, Kindred T, Lau E. Compilation of Observations of the October 15 , 2006

2006.

[25] Mitrani-Resier J, Wu S, Beck JL. Virtual Inspector and its application to immediate pre-event and post-event earthquake loss and safety assessment of buildings. Nat Hazards 2016;81:1861–78. doi:10.1007/s11069-016-2159-6.

[26] Vamvatsikos D, Allin Cornell C. Incremental dynamic analysis. Earthq Eng Struct Dyn 2002;31:491–514. doi:10.1002/eqe.141.

[27] Vamvatsikos D, Cornell CA. The Incremental Dynamic Analysis and Its Application To Performance-Based Earthquake Engineering. Eur Conf Earthq Eng 2002:10.

[28] Dolsek M. Incremental dynamic analysis with consideration of modeling uncertainties. Earthq Eng Struct Dyn 2009;38:805–25. doi:10.1002/eqe.869.

[29] Joe M, Karl T, Mohr D, William H. Test Applications of Advanced Seismic Assessment Guidelines. Pacific Earthq Eng Res Cent 2006.

[30] Maffei J, Telleen K, Nakayama Y. Probability-based seismic assessment of buildings, considering post-earthquake safety. Earthq Spectra 2008;24:667–99. doi:10.1193/1.2950066.

[31] Yeo GL, Cornell CA. Building tagging criteria based on aftershock PSHA. Proceeding 13WCEE, Vancouver, Canada Pap 2004;3283.

[32] Raghunandan M, Liel AB, Luco N. Aftershock collapse vulnerability assessment of reinforced concrete frame structures. Earthq Eng Struct Dyn 2015;44:419–39. doi:10.1002/eqe.2478.

[33] Burton HV, Deierlein GG. Integrating visual damage simulation, virtual inspection, and collapse capacity to evaluate post-earthquake structural safety of buildings. Earthq Eng Struct Dyn 2018;47:294–310. doi:10.1002/eqe.2951.

[34] Breiman, L., Friedman, J., Stone, C. J., & Olshen RA. Classification and regression trees. CRC press; 1984.

[35] Efron B, Tibshirani R. Bootstrap methods for standard errors, confidence intervals, and other measures of statistical accuracy. Stat Sci 1986:54–75.

[36] Kohavi R, others. A study of cross-validation and bootstrap for accuracy estimation and

model selection. Proc. Fourteenth Int. Jt. Conf. Artif. Intell., vol. 14, San Mateo, CA: 1995, p. 1137–45.

[37] Breiman L. Bagging predictors. Mach Learn 1996;24:123–40.

[38] Kuhn M, Johnson K. Applied predictive modeling. Springer; 2013.

[39] Breiman L. Random forests. Mach Learn 2001;45:5–32.

[40] Hanley JA, McNeil BJ. The meaning and use of the area under a receiver operating characteristic (ROC) curve. Radiology 1982;143:29–36. doi:10.1148/radiology.143.1.7063747.

[41] Bradley AP. The use of the area under the ROC curve in the evaluation of machine learning algorithms. Pattern Recognit 1997;30:1145–59. doi:10.1016/S0031-3203(96)00142-2.

[42] Haselton CB, Deierlein GG. Assessing seismic collapse safety of modern reinforced concrete moment-frame buildings. PEER Report 2007/08, Pacific Earthquake Engineering Research Center, Berkeley, CA: 2008. doi:10.1061/(ASCE)ST.1943-541X.0000318.

[43] ACI Committee 318. Building Code Requirements for Structural Concrete (ACI 318-08). vol. 2007. 2008. doi:10.1016/0262-5075(85)90032-6.

[44] Mazzoni S, Mckenna F, Scott MH, Fenves GL. Open System for Earthquake Engineering Simulation (OpenSees) OpenSees Command Language Manual 2007.

[45] Ibarra LF, Medina R a., Krawinkler H. Hysteretic models that incorporate strength and stiffness deterioration. Earthq Eng Struct Dyn 2005;34:1489–511. doi:10.1002/eqe.495.

[46] Panagiotakos TB, Fardis MN. Deformation of reinforced concrete at yielding and untimate. ACI Struct J 2001;98:135–47. doi:10.14359/10181.

[47] Haselton CB, Liel AB, Lange ST. Beam-Column Element Model Calibrated for Predicting Flexural Response Leading to Global Collapse of RC Frame Buildings. PEER Report 2007/03, Pacific Earthquake Engineering Research Center, Berkeley, CA: 2008.

[48] Campbell KW, Bozorgnia Y. Campbell-Bozorgnia NGA Empirical Ground Motion Model for the Average Horizontal Component of PGA, PGV, PGD and SA at Selected

Spectral Periods Ranging from 0.01–10.0 Seconds (Version 1.1) 2006.

[49] Campbell KW, Bozorgnia Y. NGA-West2 Ground Motion Model for the Average Horizontal Components of PGA, PGV, and 5% Damped Linear Acceleration Response Spectra. Earthq Spectra 2014;30:1087–115. doi:10.1193/062913EQS175M.

[50] Baker JW, Cornell CA. Spectral shape, epsilon and record selection. Earthq Eng Struct Dyn 2006;35:1077–95. doi:10.1002/eqe.571.

[51] Baker JW. Conditional Mean Spectrum: Tool for Ground-Motion Selection. J Struct Eng 2010;137:322–31. doi:10.1061/(ASCE)ST.1943-541X.0000215.

[52] Moehle J, Bozorgnia Y, Jayaram N, Jones P, Rahnama M, Shome N, et al. Case studies of the seismic performance of tall buildings designed by alternative means: task 12 report for the tall buildings initiative: final report to California seismic safety commission and California emergency management agency. PEER Report 2011/05, Pacific Earthquake Engineering Research Center, Berkeley, CA: 2011.

[53] Los Angeles Tall Building Design Council. An alternative procedure for seismic analysis and design of tall buildings located in the Los Angeles region. Los Angeles,CA: 2008.

[54] Orakcal K, Wallace JW, Conte JP. Flexural Modeling of Reinforced Concrete Walls-Model Attributes. ACI Struct J 2004;101:688–98. doi:10.14359/13391.

[55] Orakcal K, Wallace JW. Flexural Modeling of Reinforced Concrete Walls - Experimental Verification. ACI Struct J 2006;103:196–206. doi:10.14359/15177.

[56] Mander JB, Priestley MJN, Park R. Theoretical Stress-Strain Model for Confined Concrete. J Struct Eng 1988;114:1804–26. doi:10.1061/(ASCE)0733-9445(1988)114:8(1804).

[57] ATC 72-1. Modeling and Acceptance Criteria for Seismic Design and Analysis of Tall Buildings. Redwood City, California: 2010.

[58] Kolozvari K, Piatos G, Beyer K. Practical nonlinear modeling of U-shaped reinforced concrete walls under bi-directional loading. Proc 16th World Conf Earthq Eng 2017.

[59] Naish D. Testing and Modeling of Reinforced Concrete Coupling Beams. Ph.D.

Dissertation, Department of Civil & Environmental Engineering, University of California, Los Angeles, CA, 2010.

[60] Omori T, One I. The Centenary a Decay of the Omori Formula Activity for Law of Aftershock Tokuji Utsu ,* Yosihiko Ogata , and Ritsuko S . Matsu ' ura 1995:1–33.

[61] Reasenberg P a, Jones LM. Earthquake hazard after a mainshock in california. Science 1989;243:1173–6. doi:10.1126/science.243.4895.1173.

[62] Yeo GL, Cornell CA. A probabilistic framework for quantification of aftershock ground-motion hazard in California: Methodology and parametric study. Earthq Eng Struct Dyn 2009;38:45–60. doi:10.1002/eqe.840.

[63] Boore DM, Atkinson GM. Ground-Motion Prediction Equations for the Average Horizontal Component of PGA, PGV, and 5%-Damped PSA at Spectral Periods between 0.01 *s* and 10.0 *s*. Earthq Spectra 2008;24:99–138. doi:10.1193/1.2830434.

[64] Ancheta TD, Darragh RB, Stewart JP, Seyhan E, Silva WJ, Chiou BS-J, et al. NGA-West2 Database. Earthq Spectra 2014;30:989–1005. doi:10.1193/070913EQS197M.

[65] Knopoff L, Gardner JK. Higher Seismic Activity During Local Night on the Raw Worldwide Earthquake Catalogue. Geophys J R Astron Soc 1972;28:311–3. doi:10.1111/j.1365-246X.1972.tb06133.x.

[66] Wooddell KE, Abrahamson NA. Classification of main shocks and aftershocks in the NGA-West2 database. Earthq Spectra 2014;30:1257–67. doi:10.1193/071913EQS208M.

[67] Jeon J-S, DesRoches R, Lowes LN, Brilakis I. Framework of aftershock fragility assessment-case studies: older California reinforced concrete building frames. Earthq Eng Struct Dyn 2015;44:2617–36. doi:10.1002/eqe.2599.

[68] Yeo GL, Cornell CA. Building life-cycle cost analysis due to mainshock and aftershock occurrences. Struct Saf 2009;31:396–408. doi:10.1016/j.strusafe.2009.01.002.

[69] Nazari N, van de Lindt JW, Li Y. Effect of Mainshock-Aftershock Sequences on Woodframe Building Damage Fragilities. J Perform Constr Facil 2013;29:130906020356006. doi:10.1061/(ASCE)CF.1943-5509.0000512.

[70] Shokrabadi M, Burton HV. Risk-based assessment of aftershock and mainshock-aftershock seismic performance of reinforced concrete frames. Struct Saf 2018;73:64–74. doi:10.1016/j.strusafe.2018.03.003.

[71] Burton HV, Sreekumar S, Sharma M, Sun H. Estimating aftershock collapse vulnerability using mainshock intensity, structural response and physical damage indicators. Struct Saf 2017;68:85–96. doi:10.1016/j.strusafe.2017.05.009.

[72] Zhang Y, Burton HV, Sun H, Shokrabadi M. A machine learning framework for assessing post-earthquake structural safety. Struct Saf 2018;72:1–16. doi:10.1016/j.strusafe.2017.12.001.

[73] Lignos D. Sidesway Collapse of Deteriorating Structural Systems Under Seismic Excitations. Stanford University; 2008.

[74] Goulet CA, Haselton CB, Mitrani-Reiser J, Beck JL, Deierlein GG, Porter KA, et al. Evaluation of the seismic performance of a code-conforming reinforced-concrete frame building-from seismic hazard to collapse safety and economic losses. Earthq Eng Struct Dyn 2007;36:1973–97. doi:10.1002/eqe.694.

[75] Haselton CB, Liel AB, Deierlein GG, Dean BS, Chou JH. Seismic Collapse Safety of Reinforced Concrete Buildings. I: Assessment of Ductile Moment Frames. J Struct Eng 2011;137:481–91. doi:10.1061/(ASCE)ST.1943-541X.0000318.

[76] TBI Guidelines Working Group. Guidelines for Performance-Based Seismic Design of Tall Buildings. Berkeley, CA: 2010.

[77] Tibshirani R. Regression Shrinkage and Selection via the Lasso. J R Stat Soc Ser B 1996;58:267–88. doi:10.2307/2346178.

[78] Vapnik VN. The nature of statistical learning theory. Springer; 1995.

[79] Vapnik V, Golowich SE. Support Vector Method for Function Approximation, Regression Estimation, and Signal Processing· n.d.

[80] Schölkopf B, Smola AJ. Learning with kernels : support vector machines, regularization, optimization, and beyond. MIT Press; 2002.

[81] Moehle J, Bozorgnia Y, Yang TY. The Tall Buildings Initiative. Seaoc 2007 2007:1–

10. doi:10.1002/tal.435.

[82] Dutta A, Hamburger RO. Case study of a 40-storey buckling-restrained braced frame building located in Los Angeles. Struct Des Tall Spec Build 2009;19:77–93. doi:10.1002/tal.543.

[83] Yang TY, Moehle JP, Bozorgnia Y, Zareian F, Wallace JW. Performance assessment of tall concrete core-wall building designed using two alternative approaches. Earthq Eng Struct Dyn 2012;41:1515–31. doi:10.1002/eqe.2219.

[84] Moehle J. Performance-Based Earthquake Engineering in the U.S.: A Case Study for Tall Buildings Tall buildings Tall buildings Tall buildings Tall buildings, Springer, Dordrecht; 2014, p. 385–99. doi:10.1007/978-94-017-8875-5_26.

[85] Jayaram N, Shome N, Rahnama M. Development of earthquake vulnerability functions for tall buildings. Earthq Eng Struct Dyn 2012;41:1495–514. doi:10.1002/eqe.2231.

[86] Jones P, Zareian F. Seismic response of a 40-storey buckling-restrained braced frame designed for the Los Angeles region. Struct Des Tall Spec Build 2013;22:291–9. doi:10.1002/tal.687.

[87] Tipler JF, Deierlein GG, Almufti I. Seismic Resilience of Tall Buildings - Benchmarking Performance and Quantifying Improvements. 10th US Natl Conf Earthq Eng 2014. doi:10.4231/D3QJ77Z84.

[88] Kazama M, Noda T. Damage statistics (Summary of the 2011 off the Pacific Coast of Tohoku Earthquake damage). Soils Found 2012;52:780–92. doi:10.1016/j.sandf.2012.11.003.

[89] Burton HV, Sharma M. Quantifying the Reduction in Collapse Safety of Main Shock–Damaged Reinforced Concrete Frames with Infills. Earthq Spectra 2017;33:25–44. doi:10.1193/121015EQS179M.

[90] Ruiz-García J, Negrete-Manriquez JC. Evaluation of drift demands in existing steel frames under as-recorded far-field and near-fault mainshock-aftershock seismic sequences. Eng Struct 2011;33:621–34. doi:10.1016/j.engstruct.2010.11.021.

[91] Li Q, Ellingwood BR. Performance evaluation and damage assessment of steel frame buildings under main shock–aftershock earthquake sequences. Earthq Eng Struct Dyn

2007;36:405–27. doi:10.1002/eqe.667.

[92] Zhang Y, Burton H V. Pattern recognition approach to assess the residual structural capacity of damaged tall buildings. Struct Saf 2019;78:12–22. doi:10.1016/J.STRUSAFE.2018.12.004.

[93] Brandow G, Carpenter L, Cochran BL, Hart GC, Huang SC, Lew M, et al. An Alternative Procedure for Seismic Analysis and Design of Tall Buildings Located in the Los Angeles Region 2005.

[94] ASCE. Seismic Evaluation and Retrofit of Existing Buildings: ASCE Standard ASCE/SEI 41-13. American Society of Civil Engineers; 2014.

[95] Naish D, Fry A, Klemencic R, Wallace J. Reinforced concrete coupling beams-part I: Testing. ACI Struct J 2013;110:1057–66.

[96] Deniz D, Song J, Hajjar JF. Energy-based seismic collapse criterion for ductile planar structural frames. Eng Struct 2017;141:1–13. doi:10.1016/j.engstruct.2017.02.051.

[97] Baker JW. Efficient Analytical Fragility Function Fitting Using Dynamic Structural Analysis. Earthq Spectra 2015;31:579–99. doi:10.1193/021113EQS025M.

[98] Shinozuka M, Feng MQ, Lee J, Naganuma T. Statistical Analysis of Fragility Curves. J Eng Mech 2000;126:1224–31. doi:10.1061/(ASCE)0733-9399(2000)126:12(1224).

[99] Straub D, Der Kiureghian A. Improved seismic fragility modeling from empirical data. Struct Saf 2008;30:320–36. doi:10.1016/j.strusafe.2007.05.004.

[100] Luco N, Bachman RE, Crouse CB, Harris JR, Hooper JD, Kircher CA, et al. Updates to building-code maps for the 2015 NEHRP Recommended Seismic Provisions. Earthq Spectra 2015;31:S245–71. doi:10.1193/042015EQS058M.

[101] Liel AB, Haselton CB, Deierlein GG. Seismic Collapse Safety of Reinforced Concrete Buildings. II: Comparative Assessment of Nonductile and Ductile Moment Frames. J Struct Eng 2011;137:492–502. doi:10.1061/(ASCE)ST.1943-541X.0000275.

[102] Haselton CB, Baker JW, Liel AB, Deierlein GG. Accounting for Ground-Motion Spectral Shape Characteristics in Structural Collapse Assessment through an Adjustment for Epsilon. J Struct Eng 2011;137:332–44. doi:10.1061/(ASCE)ST.1943-

541X.0000103.

[103] Naish D, Fry A, Klemencic R, Wallace J. Reinforced Concrete Coupling Beams-Part II: Modeling. ACI Struct J 2013;110:1067–75.

[104] Survey USG. Implications for earthquake risk reduction in the United States from the Kocaeli, Turkey, earthquake of August 17, 1999. 2000. doi:10.3133/CIR1193.

[105] Stewart JP, Zimmaro P, Lanzo G, Mazzoni S, Ausilio E, Aversa S, et al. Reconnaissance of 2016 Central Italy Earthquake Sequence. Earthq Spectra 2018;34:1547–55. doi:10.1193/080317EQS151M.

[106] Ruiz-García J, Negrete-Manriquez JC. Evaluation of drift demands in existing steel frames under as-recorded far-field and near-fault mainshock–aftershock seismic sequences. Eng Struct 2011;33:621–34. doi:10.1016/J.ENGSTRUCT.2010.11.021.

[107] Ruiz-García J, Aguilar JD. Aftershock seismic assessment taking into account postmainshock residual drifts. Earthq Eng Struct Dyn 2015;44:1391–407. doi:10.1002/eqe.2523.

[108] Tesfamariam S, Goda K, Mondal G. Seismic vulnerability of reinforced concrete frame with unreinforced masonry infill due to main shock-aftershock earthquake sequences. Earthq Spectra 2015;31:1427–49. doi:10.1193/042313EQS111M.

[109] Luco N, Bazzurro P, Allin Cornell C. Dynamic Versus Static Computation of the Residual Capacity of a Mainshock-Damaged Building To Withstand an Aftershock. 13th World Conf Earthq Eng 2004.

[110] Bazzurro P, Cornell CA, Menun C, Motahari M. Guidelines for seismic assessment of damaged buildings. Proc. 13th World Conf. Earthq. Eng. Vancouver, Canada, 2004.

[111] Hatzigeorgiou GD, Liolios AA. Nonlinear behaviour of RC frames under repeated strong ground motions. Soil Dyn Earthq Eng 2010;30:1010–25. doi:10.1016/j.soildyn.2010.04.013.

[112] Han R, Li Y, van de Lindt J. Assessment of Seismic Performance of Buildings with Incorporation of Aftershocks. J Perform Constr Facil 2015;29:04014088. doi:10.1061/(ASCE)CF.1943-5509.0000596.

[113] Shokrabadi M, Burton H V. Building service life economic loss assessment under sequential seismic events. Earthq Eng Struct Dyn 2018;47:1864–81. doi:10.1002/eqe.3045.

[114] Jalayer F, Asprone D, Prota A, Manfredi G. Multi-hazard upgrade decision making for critical infrastructure based on life-cycle cost criteria. Earthq Eng Struct Dyn 2011;40:1163–79. doi:10.1002/eqe.1081.

[115] Alessandri S, Giannini R, Paolacci F. Aftershock risk assessment and the decision to open traffic on bridges. Earthq Eng Struct Dyn 2013;42:2255–75. doi:10.1002/eqe.2324.

[116] Iervolino I, Giorgio M, Chioccarelli E. Markovian modeling of seismic damage accumulation. Earthq Eng Struct Dyn 2016;45:441–61. doi:10.1002/eqe.2668.

[117] Yeo GL, Cornell CA. Post-quake decision analysis using dynamic programming. Earthq Eng Struct Dyn 2009;38:79–93. doi:10.1002/eqe.842.

[118] Yeo GL, Cornell CA. Building tagging criteria based on aftershock PSHA. Proceeding 13WCEE, Vancouver, Canada Pap 2004.

[119] Yeo GL, Cornell CA. Stochastic characterization and decision bases under time-dependent aftershock risk in performance-based earthquake engineering. Pacific Earthquake Engineering Research Center Berkeley, CA; 2005.

[120] Yeo GL, Cornell CA. Equivalent constant rates for post-quake seismic decision making. Struct Saf 2009;31:443–7. doi:10.1016/j.strusafe.2008.11.002.

[121] Comerio MC. Estimating downtime in loss modeling. Earthq Spectra 2006;22:349–65. doi:10.1193/1.2191017.

[122] Hutt CM, Asce M, Almufti I, Willford M, Deierlein G, Asce F. Seismic Loss and Downtime Assessment of Existing Tall Steel-Framed Buildings and Strategies for Increased Resilience. J Struct Eng 2016;142. doi:10.1061/(ASCE)ST.1943-541X.0001314.

[123] Cimellaro GP. Downtime and Recovery Models, Springer, Cham; 2016, p. 93–108. doi:10.1007/978-3-319-30656-8_5.

[124] De Iuliis M, Kammouh O, Cimellaro GP, Tesfamariam S. Downtime estimation of

building structures using fuzzy logic. Int J Disaster Risk Reduct 2019;34:196–208. doi:10.1016/J.IJDRR.2018.11.017.

[125] De Iuliis M, Kammouh O, Cimellaro GP, Tesfamariam S. Resilience of the Built Environment: A Methodology to Estimate the Downtime of Building Structures Using Fuzzy Logic. Resilient Struct. Infrastruct., Singapore: Springer Singapore; 2019, p. 47–76. doi:10.1007/978-981-13-7446-3_2.